POLITECNICO DI MILANO

Facoltà di Ingegneria dei Sistemi

Corso di Laurea Specialistica in Ingegneria Biomedica

PATIENT-SPECIFIC MODELING OF A STENTING PROCEDURE IN CORONARY BIFURCATIONS: A FINITE ELEMENT STUDY

Relatore: *Prof*. Francesco MIGLIAVACCA

Correlatore: *Ing*. Stefano MORLACCHI

Tesi di Laurea Specialistica di:

Sebastian George COLLEONI

Anno Accademico 2010-2011

Index

5. RESULTS AND DISCUSSION

6. CONCLUSIONS, LIMITATIONS AND FURTHER DEVELOPMENT

Summary

1. Introduction

Stenting in coronary bifurcation has always been an important issue in cardiology, considering the higher procedural difficulties and the post-interventional risks, mainly due to the injury provoked on the arterial wall and to hemodynamic disturbances [35, 36]. In the past decade, several finite element analyses carried out have provided new information on stenting procedures in coronary bifurcation and on their main clinical issues [27]. Most of these models lack patient-specificity, simulating stenting interventions in idealized arterial geometries. Therefore, these works can only provide general guidelines and not specific indications for the planning of each patient treatment.

Lately, a few numerical studies have been performed using patient-specific reconstructions of atherosclerotic coronary segments, based on vascular imaging tools [38, 40]. Nevertheless, many limitations to an optimal realistic technique can be found. As far as image-based arterial modeling is concerned, many works base their geometry reconstruction on one imaging technique, although the information offered by one method can never fully describe the coronary morphology [20]. Furthermore, in order to decrease computational cost, the majority of these works carry significant simplifications. Indeed, to the author's knowledge, no image-based model involving coronary stenting considers the

effect of plaque, even though its plastic mechanical properties strongly influence stent deployment. Also, many numerical works do not take into account the presence of the balloon, whose incidence cannot be neglected in order to achieve a realistic stent expansion, as proved by Gervaso et al. [42].

Hence, the aim of this work is to implement a patient-specific virtual model, overcoming the limitations of the current state-of-the-art in finite element stenting procedures simulations. The atherosclerotic image-based geometry of the vessel's internal surface was reconstructed by Cárdenes et al. [23]. An actual intervention case that took place in Hospital Doctor Peset (Valencia, Spain) involving a provisional T-stenting without final kissing balloon inflation was investigated. Medical devices used in the stenting procedure case were accurately modeled, and particular attention was paid to the insertion of the stents on the catheters and their correct positioning in the complex bifurcated geometry. The computational results were investigated in order to assess stent deployment in a specific case and the final configuration achieved was subsequently compared with the image-based reconstruction of the post-stenting lumen geometry.

2. Materials and methods

2.1 Coronary bifurcation model

The pre-interventional geometry of a patient-specific atherosclerotic left anterior descending coronary artery (LAD) was generated using a modeling technique that takes information from conventional coronary angiography (CCA) and computed tomography angiography (CTA) images, routinely used in clinical practice. Based on such vascular geometry data, the 3D reconstruction of the stenotic lumen was created [23]. In order to achieve a full arterial model, the coronary wall was recreated. First, the bifurcation centerline was identified and the various branches were split, using the open-source vascular modeling toolkit VMTK [51]. Subsequently, the external wall surfaces were generated, using the CAD software RHINOCEROS 4.0 Evaluation (McNeel & Associates, Indianapolis, IN, USA). Such operation was performed creating circumferences perpendicular to the centerline, basing the geometrical values on physiological data of

Figure 1 – 3D final reconstruction of the diseased bifurcated coronary artery. The distributed stenosis in the main branch is remarkable.

internal diameters and wall thicknesses of LAD and its diagonal branches [51, 52]. The final patient specific reconstruction is shown in Figure 1.

The geometry was then discretized using ANSYS ICEM CFD (Ansys Inc., Canonsburg, PA, USA). The hexahedral meshing procedure utilized the blocking strategy, a technique in which an adequate block topology was built to fit the vascular geometry. Mesh density was increased in the regions of interest, i.e. in the bifurcated tracts and along the wall thickness towards to the lumen. The final mesh consisted of 187326 hexahedral elements. Figure 2A shows part of the final discretization.

Finally, the atherosclerotic plaque was identified using the commercially available software package MATLAB (MathWorks Inc., Natick, MA, USA). The developed function computed the distance between each node of the mesh and the centerline of the external wall surface, identifying where plaque elements could reasonably be present. Results are shown in Figure 2B.

The material properties used for the coronary artery wall replicated the mechanical behavior of the media layer in the circumferential direction and were modeled by means of a hyperelastic isotropic constitutive law. The law describing the material model was based on a sixth-order reduced polynomial strain energy density function (SEDF). The experimental data used to characterize the vascular wall was obtained by the work carried out by Holzapfel et al. (2005) [49]. The atherosclerotic plaque behavior, on the other hand, was described through an isotropic hyperelasto-plastic model. The hyperelastic part was implemented based on the stress-strain curves obtained by Loree et al. (1994) for cellular plaques [54], while the plastic behavior was modeled by means of a perfect plasticity law.

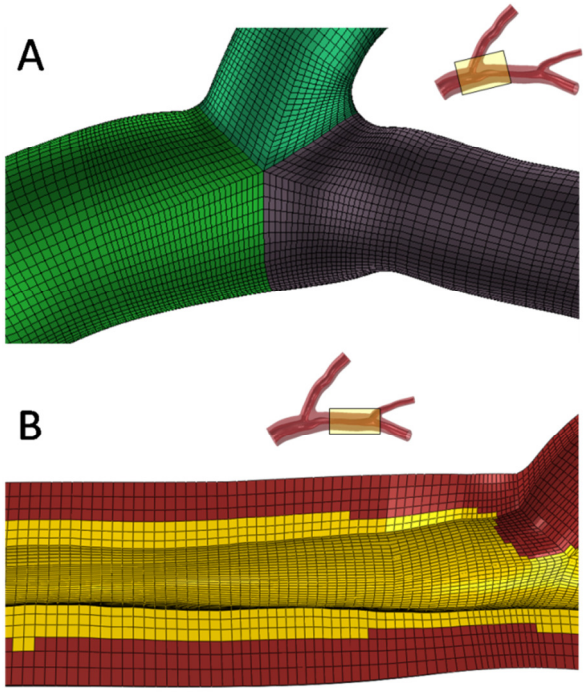

Figure 2 – Hexahedral discretization of a bifurcated segment of the arterial model (A) and plaque (yellow) identification in the atherosclerotic main branch (B).

2.2 Stent and balloon models

The actual intervention performed involved two Endeavor Resolute (Medtronic, Minneapolis, MN, USA) coronary stents. The geometries of the intravascular devices were generated using the previously mentioned CAD software. The crown-shaped rings were built based on the geometrical data provided by the manufacturer, and then fused together using Boolean difference. The final 15 mm Endeavor stent model used is shown in Figure 3. The meshing procedure of the stent model was performed using hexahedral discretization. Bidimensional meshes were created in the circular cross sections and dragged along the surfaces, increasing mesh density in the curved regions, characterized by a higher stress gradient. Final discretization generated 272384 hexahedral elements, and part of it is shown in Figure 4. Endeavor stents are made of a cobalt-chromium alloy, and the material behavior considered in the numerical work was described through a Von Mises-Hill plasticity model with isotropic hardening. The material constants were chosen according to typical biocompatible Co-Cr alloys: density was assumed equal to 8.5 g/cm^3, Young's modulus was set to 233 GPa and Poisson's ratio to 0.35.

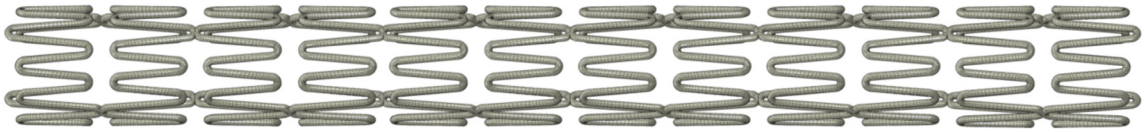

Figure 3 – CAD model of the 15 mm Endeavor Resolute coronary stent used.

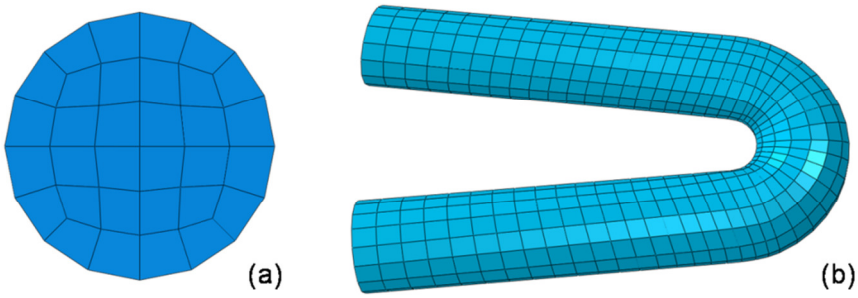

Figure 4 – Final mesh generated for the stent model. Cross-sectional elements (a) and discretization along the curved regions (b).

The balloon models, on the other hand, were first created in their expanded configuration, and then deflated in order to obtain a multi-folded configuration. Such configuration was compared to a more realistic five-folded balloon, and results in terms of stent deployment did not demonstrate a remarkable difference between the two. Therefore, the multi-folded balloon model was chosen in order to decrease computational effort. The numerical work performed to deflate the balloon is shown in Figure 5.

The balloon surface was discretized using 10368 membrane elements, through a quad-dominated sweep technique. The mechanical behavior was modeled by means of an isotropic linear elastic law, based on stress-strain curves of PET.

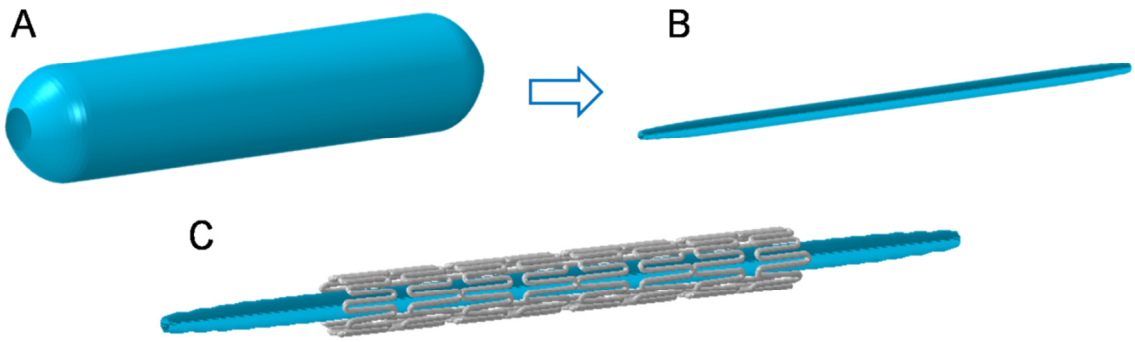

Figure 5 – Deflation of the multi-folded balloon, from the expanded configuration (A) to the deflated one (B), able to be inserted inside the crimped stent model (C).

2.3 Preliminary simulations: crimping and bending

In order to replicate the *in-vivo* procedure, the intravascular devices used in the intervention had to be accurately positioned in the patient-specific arterial model. This issue required preliminary simulations of stent crimping, stent bending and balloon bending. The preliminary computational work on the stent model was performed using the commercial code ABAQUS/Standard (Dassault Systèmes Simulia Corp., Providence, RI, USA). First the stent was crimped to a smaller diameter, in order to fit inside the obstructed arterial regions. Crimping was obtained by means of a rigid cylinder under radial displacement control, decreasing the stent external diameter from an initial value of 1.6 mm to 1.1 mm. Subsequently the bending simulations were carried out, in which the stents were set to advance on cylindrical guides following the post-angioplasty vessel centerline. Stent advancement was achieved imposing longitudinal boundary conditions at the links of the device. The stent-guide contact was modeled by means of a soft contact interaction property, with linear pressure-overclosure relationship and friction coefficient equal to 0.3.
Balloon bending was necessary to position the multi-folded balloon models inside the bent stents. This operation was performed using the finite element code ABAQUS/Explicit. Adequate CAD geometries of bent catheter and outer guide were created, and balloon advancement was accomplished by means of concentrated loads acting on the end nodes of the balloon. The multi-folded configuration was maintained constraining several balloon elements as rigid bodies.

2.4 Final simulations

The clinical case was simulated following the procedural indications provided by the clinicians involved in the actual intervention. Two Endeavor stents were implanted in the main branch of the arterial geometry, between the first and the second diagonal branches. First a pre-dilation was performed, using a 15 mm long angioplasty balloon with a diameter of 2.5 mm. Subsequently the distal stent was inserted and balloon expanded at 12 atm by means of a 2.75 mm x 19 mm balloon. Finally, the proximal device was implanted at 14 atm using a 3 mm x 19 mm balloon, resulting in a small overlap between the two coronary stents.
The described procedure was replicated using the finite element method, with ABAQUS/Explicit. The quasi-staticity of the analysis was verified monitoring the energy

trend of the two devices, ensuring the kinetic energy did not exceed a small fraction of the internal energy. A realistic balloon expansion was achieved imposing a gradually increasing pressure on its inner surface, while applying a rigid body constraint to the ending elements. Contact was set between such rigid elements and the catheter model, which was fully constrained. The arterial bifurcation had its end nodes constrained in the longitudinal direction by means of four cylindrical local coordinate systems.

3. Results and discussion

3.1 Preliminary procedures

Figure 6 shows the crimping simulation outcome, in which the stent external diameter decreased from 1.6 mm to about 1.1 mm. High local stresses and plastic deformations characterized the curved parts of the stents, resulting in a permanent modification of the curvature radii. The proximal stent bending simulation is shown in Figure 7, highlighting the stress trend during bending. Interestingly, no plastic deformation was added, making the history of bending of the device during catheter insertion negligible. Moreover, the stent course prior to the implantation region is characterized by larger vessels, with greater curvature radii. These simulations were necessary for accurate positioning of the two stents inside the patient-specific bifurcated geometry.

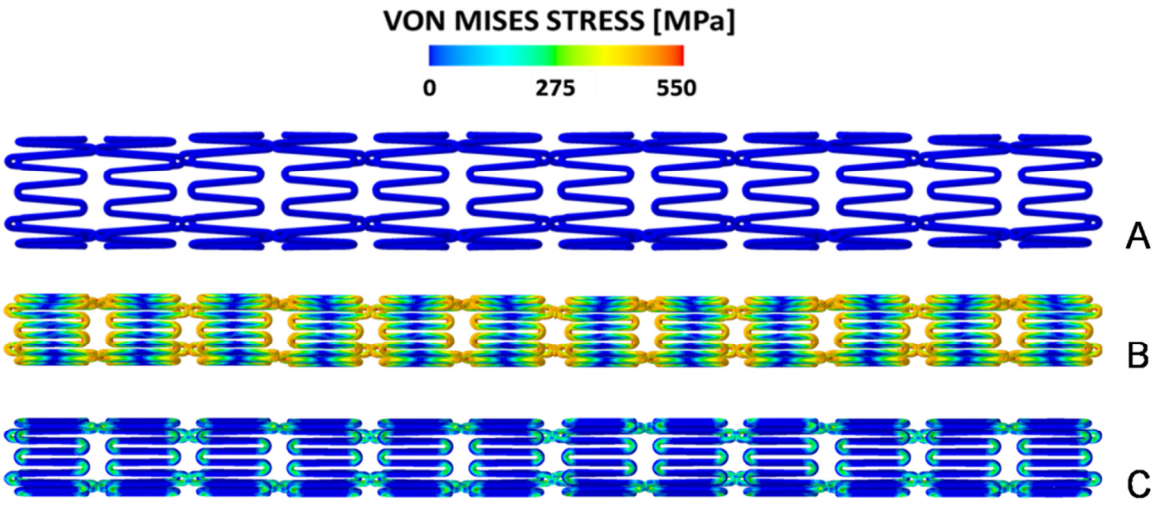

Figure 6 – Von Mises stress distributions in Endeavor stent models during crimping. Longitudinal views at initial configuration (a), at full crimping (b) and after elastic recoil (c).

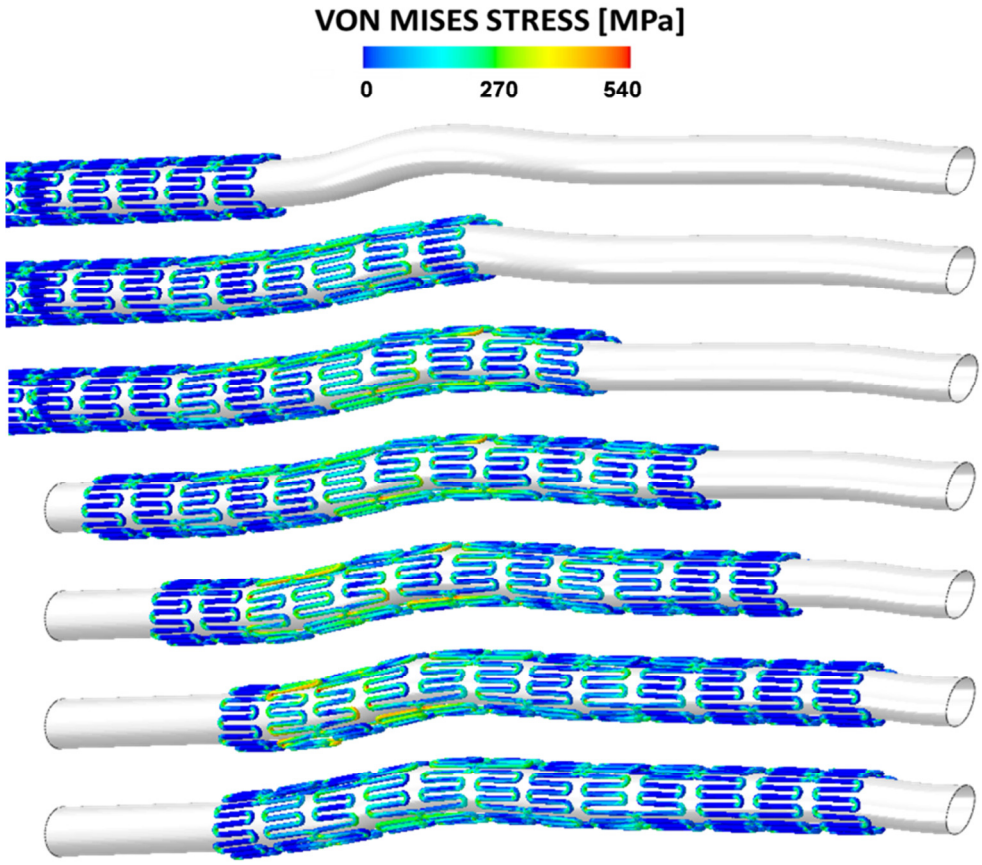

Figure 7 – Proximal stent advancement on the created guide based on the post-angioplasty lumen centerline.

3.2 Virtual clinical case

The computational simulation of the stenting procedure performed is shown in its various steps in Figure 8. The Von Mises stress distribution is shown in Figure 9, highlighting the high local stresses obtained in the curved regions of the struts and the slight increase where the stents overlap. The arterial response (see Fig. 10) was investigated in terms of maximum principal stresses achieved, identifying the arterial regions more susceptible to an aggressive pathobiological response. The most critical vascular areas, more prone to neointimal thickening, appear to be the region of overlap between the two stents and the part close to the second diagonal branch.

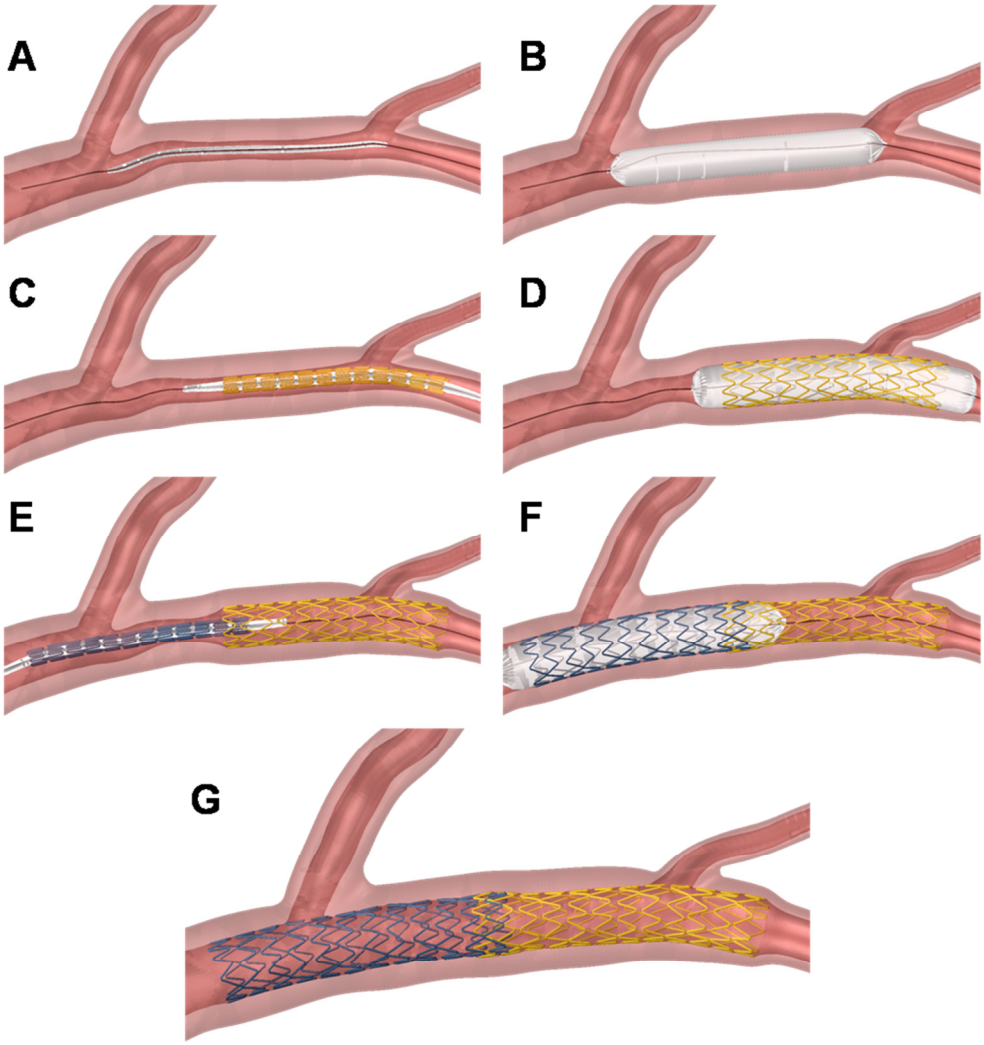

Figure 8 – Simulation of the clinical procedure performed. Angioplasty balloon insertion (A), angioplasty procedure (B), distal stent and balloon insertion (C), distal stent expansion (D), proximal stent and balloon insertion (E), proximal stent expansion (F) and final configuration after elastic recoil (G).

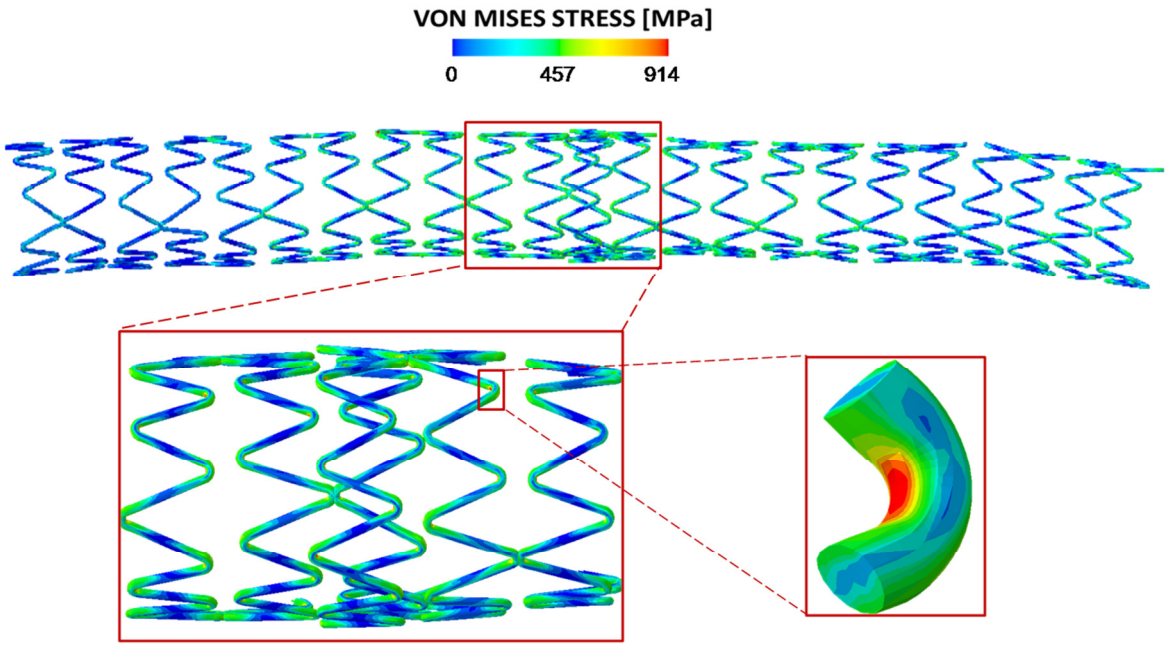

Figure 9 – Von Mises stress contour map of the two coronary stents implanted. Close-ups of the overlap region and of the maximum stress achieved on a curved strut.

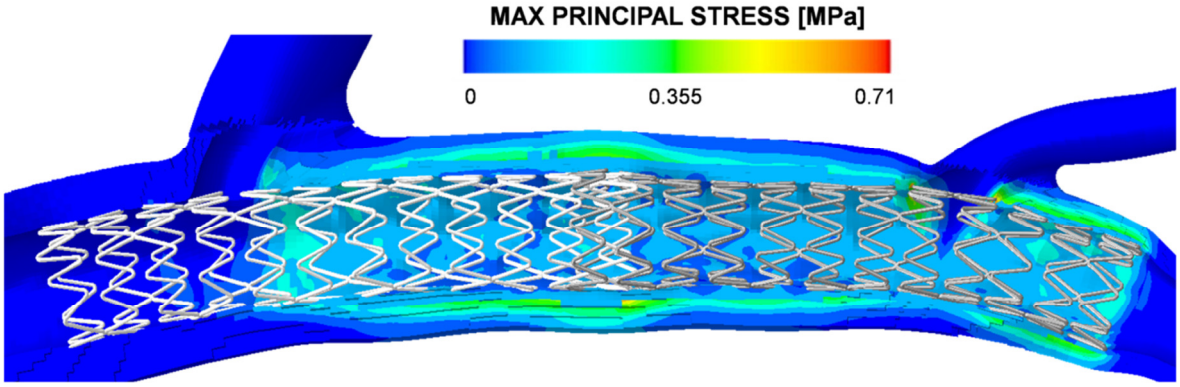

Figure 10 – Maximal principal stress distribution on the arterial wall following the double stenting procedure.

Also, the virtual simulation was compared to the actual intervention performed, investigating the two different post-stenting lumen geometries (see Figure 11). The two geometries show a generally good concordance. However, some differences can be found: the greater straightening of the diseased vessel in the numerical work, which could be explained by the absence in the model of surrounding tissues or with an only hypothesized mechanical characterization of the atherosclerotic plaques.

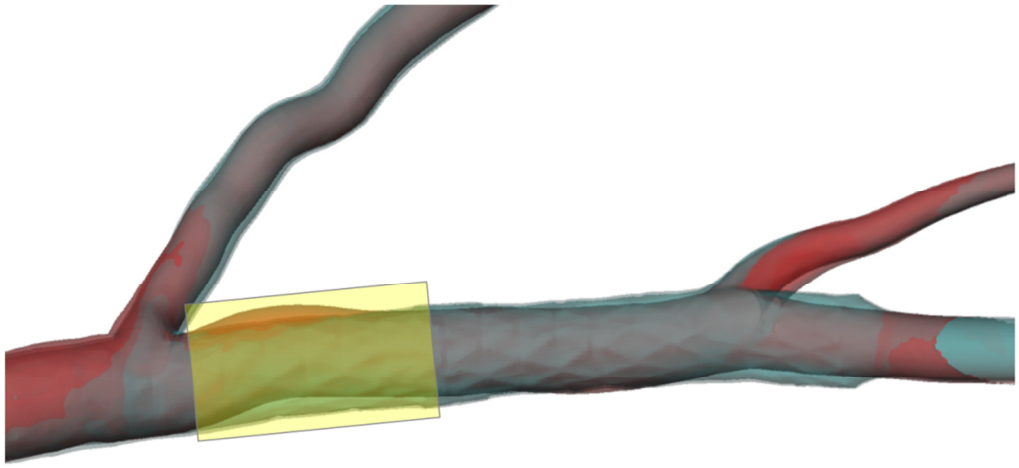

Figure 11 – Comparison of post-stenting lumen between the actual intervention (red) and the computational results (blue). The greater straightening achieved in the numerical work is highlighted in yellow.

4. Conclusions

The presented work proves the feasibility of implementing a patient-specific virtual model replicating actual clinical cases. A coronary stenting procedure that took place was simulated using the finite element method, by means of an accurate 3D reconstruction of the arterial bifurcated region and CAD geometries created reproducing the commercial devices used. The model was investigated in terms of stresses and strains obtained, and subsequently validated through a comparison with the actual post-intervention lumen. Such computational studies could be used prior to stenting implantation, comparing different clinical options and facilitating the intervention strategy planning. Also, further developments under investigation will be fluid dynamics analyses on the post-stenting lumen achieved, evaluating the efficacy of the procedure from this point of view, too. The biomechanical influence of the stenting procedure assessed in this patient-specific virtual bench testing will be compared to the clinical outcome at a 6-month follow-up.

Sommario

1. Introduzione

Le procedure di stenting in biforcazioni coronariche presentano ancora numerose problematiche cliniche dovute principalmente alle maggiori difficoltà tecniche e i rischi post-intervento. Negli ultimi anni, sono state proposte numerose analisi basate su modelli a elementi finiti in grado di fornire nuove indicazioni sulle procedure di stenting in biforcazioni coronariche e sulle loro principali problematiche [35, 36]. Tuttavia, la maggior parte di questi modelli manca di specificità, simulando interventi di stenting in geometrie arteriose idealizzate. Pertanto, questi studi possono fornire soltanto linee guida generali e non indicazioni specifiche per la pianificazione di un trattamento adatto ad ogni paziente.
Recentemente, sono stati proposti alcuni lavori numerici usando ricostruzioni *patient-specific* di segmenti coronarici aterosclerotici, basati su strumenti di *imaging* vascolare [27]. Tuttavia, molte limitazioni sono ancora presenti. Per quanto riguarda la modellazione di arterie *image-based*, molti lavori basano le loro ricostruzioni geometriche su una sola tecnica di imaging, sebbene le informazioni offerte da un metodo non siano in grado di descrivere pienamente la morfologia coronarica [20]. Inoltre, al fine di diminuire il costo computazionale, la maggioranza dei suddetti lavori contiene semplificazioni rilevanti come, per esempio, l'effetto della presenza di placche aterosclerotiche. Inoltre, molti lavori

numerici non simulano l'espansione tramite pallone per angioplastica, il cui effetto non può essere trascurato per ottenere un'espansione realistica dello stent come dimostrato in Gervaso et al. [42]. Pertanto, l'obiettivo del presente lavoro è l'implementazione di un modello virtuale *patient-specific*, cercando di superare le maggiori limitazioni dello stato dell'arte attuale. In particolare, la geometria aterosclerotica *image-based* della superficie interna del vaso è stata ricostruita da Cárdenes et al. [23]. E' stato analizzato un caso clinico trattato presso l'ospedale Hospital Doctor Peset (Valencia, Spagna) di *provisional T-stenting* senza *final kissing balloon*. I dispositivi medici usati nella procedura di stenting sono stati modellizzati facendo particolare attenzione all'inserimento degli stent sui cateteri e al loro corretto posizionamento all'interno della tortuosa geometria biforcata. I risultati numerici sono stati esaminati al fine di valutare il comportamento dello stent in un caso specifico e la configurazione finale ottenuta è stata in seguito confrontata con la ricostruzione *image-based* della geometria del lume arterioso in seguito alla procedura.

2. Materiali e metodi

2.1 Modello computazionale della biforcazione coronarica

La geometria pre-stenting del lume di un'arteria coronarica discendente anteriore sinistra (*left anterior descending artery*, LAD) aterosclerotica è stata generata usando una tecnica di modellizzazione che parte dalle informazioni geometriche tratte da immagini angiografiche convenzionali (CCA) e da tomografie computerizzate (CT), correntemente usate in routine clinica. La ricostruzione 3D del tratto stenotico è stata creata basandosi su tali dati di geometria vascolare [23] e valori fisiologici di spessore arterioso. Il primo passo è stato l'identificazione della linea media della biforcazione e lo *splitting* dei rami secondari, utilizzando il software *open-source* di modellazione vascolare VMTK [51]. In seguito, sono state create le superfici della parete esterna, usando il software CAD RHINOCEROS 4.0 Evaluation (McNeel & Associates, Indianapolis, IN, USA). Tale operazione è stata realizzata creando circonferenze perpendicolari alla centerline il cui raggio è basato sui valori fisiologici dei diametri interni e spessori di pareti dei tratti

Figura 1 – Ricostruzione finale 3D della biforcazione coronarica patologica. La stenosi all'interno del ramo principale è notevole.

coronarici analizzati [51, 52]. La ricostruzione finale *patient-specific* del caso in esame è mostrata in Figura 1.

La geometria è stata poi discretizzata usando ANSYS ICEM CFD (Ansys Inc., Canonsburg, PA, USA). La procedura di *meshing* esaedrico si è basata sulla strategia di *blocking* suddividendo la geometria vascolare in una topologia riconducibile a soli esaedri. La densità della mesh è stata aumentata nelle regioni di interesse come, per esempio, nei tratti biforcati e lungo lo spessore della parete verso il lume interno. Parte della discretizzazione finale è rappresentata in Figura 2A.

Infine, la placca aterosclerotica è stata identificata utilizzando il software commerciale MATLAB (MathWorks Inc., Natick, MA, USA).La funzione sviluppata calcola la distanza tra ogni nodo e la linea media della superficie della parete esterna, identificando dove elementi della placca potrebbero essere ragionevolmente presenti. I risultati sono mostrati in Figura 2B.

Il modello del materiale usato per la parete dell'arteria coronarica riflette il comportamento meccanico della tonaca media in direzione circonferenziale ed è stato modellizzato per mezzo di una legge costitutiva iperelastica isotropa. La legge che descrive il modello del materiale è basata su una *strain energy density function* (SEDF) polinomiale di sesto ordine. I dati sperimentali usati per caratterizzare la parete vascolare è stata ottenuta dal lavoro di Holzapfel et al. (2005) [49]. Il comportamento della placca aterosclerotica, infatti, è stato descritto con un modello isotropo iperelasto-plastico. La parte iperlelastica è stata implementata basandosi sulle curve sforzo-deformazione ottenute da Loree et al.

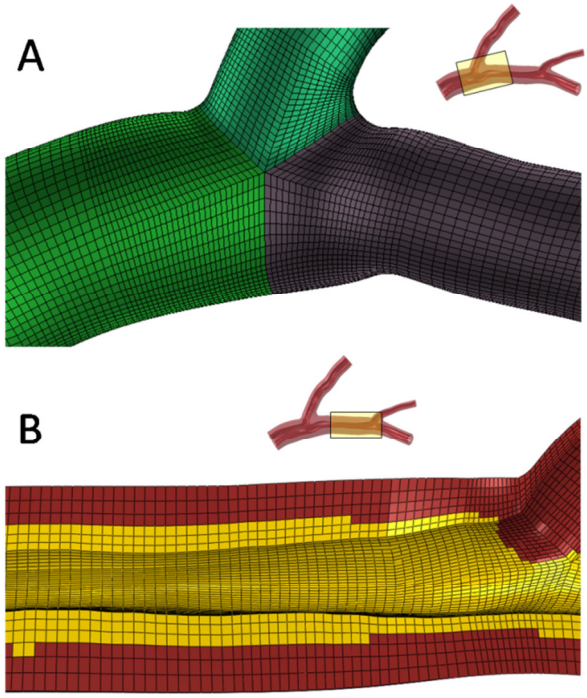

Figura 2 –Discretizzazione esaedrica del segmento biforcato del modello arterioso (A) e identificazione della placca nel main branch aterosclerotico (B).

(1994) nella caratterizzazione di placche cellulari [54], mentre il comportamento plastico è stato modellizzato per mezzo di una legge di plasticità perfetta.

2.2 Modelli computazionali di stent e palloni

L'intervento realmente avvenuto ha coinvolto l'utilizzo di due stent coronarici Endeavor Resolute (Medtronic, Minneapolis, MN, USA). Le geometrie dei dispositivi intravascolari sono state generate usando il sopra citato software CAD. Le maglie modulari dello stent sono state create basandosi sui dati geometrici forniti dall'azienda produttrice, e poi fuse una con l'altra tramite differenza booleana. Il modello dello stent Endeavor finale è rappresentato in Figura 3. La procedura di meshing dello stent è stata eseguita utilizzando esaedri. Una mesh bidimensionale è stata creata in una sezione circolare e successivamente trascinata lungo le superfici del modello. Una mesh più fitta è stata creata nelle regioni curve, caratterizzate da un maggiore gradiente di sforzo. La discretizzazione finale è illustrata in Figura 4. Gli stent Endeavor sono composti di una lega cobalto-cromo, e il comportamento del materiale considerato nel lavoro numerico è stato descritto tramite un modello di plasticità Von Mises-Hill con hardening isotropo. Le costanti del materiale

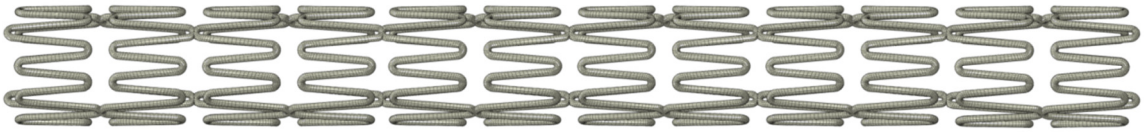

Figura 3 – Modello CAD dello stent coronarico Endeavor Resolute usato.

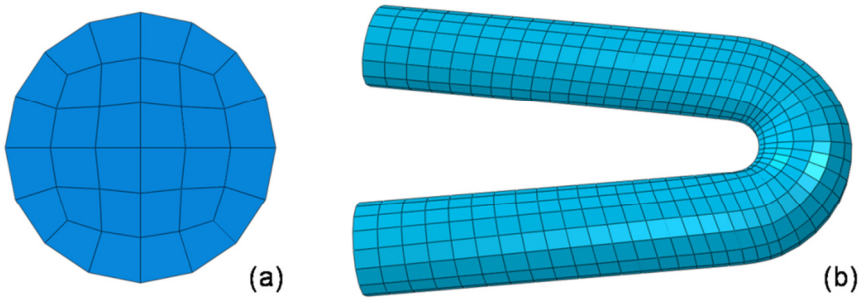

Figura 4 – Mesh finale generata per il modello di stent. Elementi nelle sezioni circolari (a) e discretizzazione lungo le regioni curve (b).

sono state scelte basandosi su tipici valori di leghe Co-Cr utilizzate per dispositivi medici: densità di 8.5 g/cm^3, modulo di Young pari a 233 GPa and coefficiente di Poisson di 0.35.

I modelli di palloni per angioplastica, invece, sono stati creati inizialmente in configurazione espansa e, in seguito, sgonfiati al fine di ottenere una conformazione *multi-folded*. Tale configurazione è stata confrontata con un modello di pallone più realistico a 5 ali. I risultati di tale confronto non dimostrano forti differenze in termini di espansione dello stent. Pertanto, a causa del minore costo computazionale, nelle successive analisi è stato utilizzato il modello *multi-folded*. L'analisi numerica effettuata per sgonfiare il pallone è mostrata in Figura 5. La superficie del pallone è stata poi discretizzata usando elementi a membrana. Il comportamento meccanico è stato modellizzato tramite una legge elastica lineare isotropa, basata su tipiche curve sforzo-deformazione del PET.

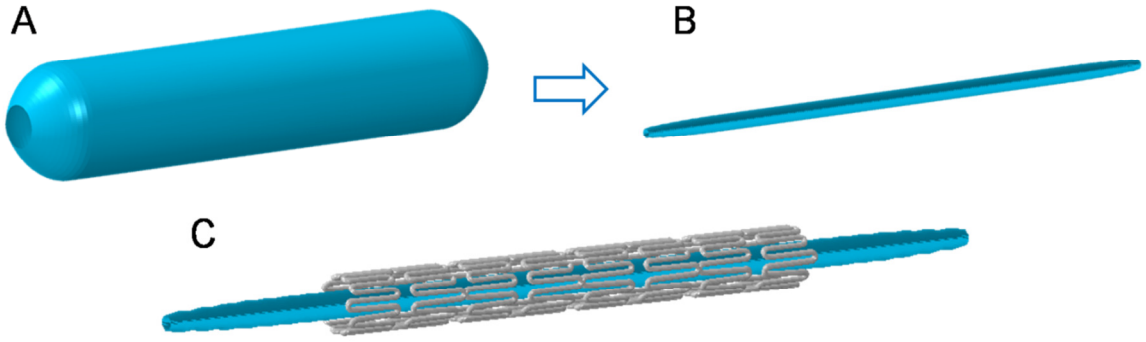

Figura 5 –Simulazione dello sgonfiaggio del pallone in maniera multi-folded, dalla configurazione espansa (A) a quella sgonfiata (B), in modo da essere inserito all'interno dello stent crimpato.

2.3 Simulazioni preliminari: crimping e inserimento

Al fine di poter replicare la reale procedura effettuata *in-vivo*, è stato necessario accuratamente posizionare nel modello dell'arteria *patient-specific* i dispositivi intravascolari usati nell'intervento. Ciò ha richiesto delle simulazioni preliminari in cui gli stent vengono crimpati e piegati e i palloni piegati per l'inserimento. Il lavoro computazionale preliminare sui modelli di stent è stato effettuato usando il codice commerciale ABAQUS/Standard (Dassault Systèmes Simulia Corp., Providence, RI, USA). Lo stent è stato inizialmente crimpato raggiungendo un diametro minore, tale da essere inserito nei tratti di arteria ostruiti. Questo è stato ottenuto per mezzo di un cilindro rigido controllato in spostamento radiale, diminuendo il diametro esterno dello stent da un valore iniziale di 1.6 mm a 1.1 mm. A partire da questa configurazione, sono state eseguite le simulazioni di inserimento degli stent all'interno dell'arteria. I dispositivi sono stati fatti avanzare su guide cilindriche modellate in base alla linea media del *main branch*. L'avanzamento degli stent è stato realizzato imponendo uno spostamento longitudinale ai link che connettono le maglie dei dispositivi. Il contatto stent-guida è stato modellizzato per mezzo di un contatto soft, con rapporto pressione-penetrazione lineare, e coefficiente di attrito pari a 0.3.

Simulazioni di inserimento dei palloni sono state necessarie per posizionare i modelli di pallone *multi-folded* all'interno degli stent piegati. Tale operazione è stata eseguita utilizzando il codice agli elementi finiti ABAQUS/Explicit. La configurazione *multi-folded* è stata mantenuta imponendo il vincolo *rigid body* a numerosi elementi del pallone.

2.4 Simulazioni finali

La procedura clinica avvenuta è stata simulata seguendo le indicazioni fornite dai cardiologi che hanno eseguito l'intervento. Due stent Endeavor sono stati impiantati nel main branch della LAD, tra il primo e il secondo ramo diagonale. Inizialmente è stata compiuta una pre-dilatazione, usando un pallone da angioplastica lungo 15 mm e avente diametro di 2.5 mm. In seguito è stato inserito lo stent distale ed espanso a 12 atm, per mezzo di un pallone di 2.75 mm x 19 mm. Infine, è avvenuto l'impianto del dispositivo prossimale, a 14 atm utilizzando un pallone di 3 mm x 19 mm, ottenendo una piccola sovrapposizione tra i due stent coronarici.

La procedura descritta è stata replicata usando il metodo degli elementi finiti, con ABAQUS/Explicit. La quasi-staticità dell'analisi è stata verificata monitorando gli andamenti delle energie cinetica e interna dei due dispositivi, assicurandosi che il rapporto tra l'energia cinetica e l'energia interna fosse rimasto minore del 5%. L'espansione realistica del pallone è stata ottenuta applicando una pressione gradualmente crescente sulla superficie interna. Il contatto è stato imposto tra gli elementi finali del pallone e il modello di catetere, totalmente incastrato. I nodi delle estremità della biforcazione sono stati vincolati in direzione longitudinale, per mezzo di quattro sistemi di riferimento cilindrici locali.

3. Risultati e discussione

3.1 Procedure preliminari

In Figura 6 è illustrato il risultato della simulazione di crimping, in cui il diametro esterno dello stent è stato fatto diminuire da 1.6 mm a 1.1 mm. Le parti curve delle maglie dello stent sono caratterizzate da alti sforzi locali e da deformazioni plastiche, risultando in una modifica permanente dei raggi di curvatura. La simulazione dell'avanzamento dello stent prossimale lungo la guida è mostrata in Figura 7, evidenziando l'andamento degli sforzi. Appare interessante notare che nessuna deformazione plastica è aggiunta, rendendo trascurabile la storia delle piegature subite dallo stent nel percorso precedente caratterizzato da vasi con diametri e raggi di curvatura maggiori. Le simulazioni descritte sono state necessarie per un posizionamento accurato dei due modelli di stent all'interno della geometria *patient-specific* della biforcazione.

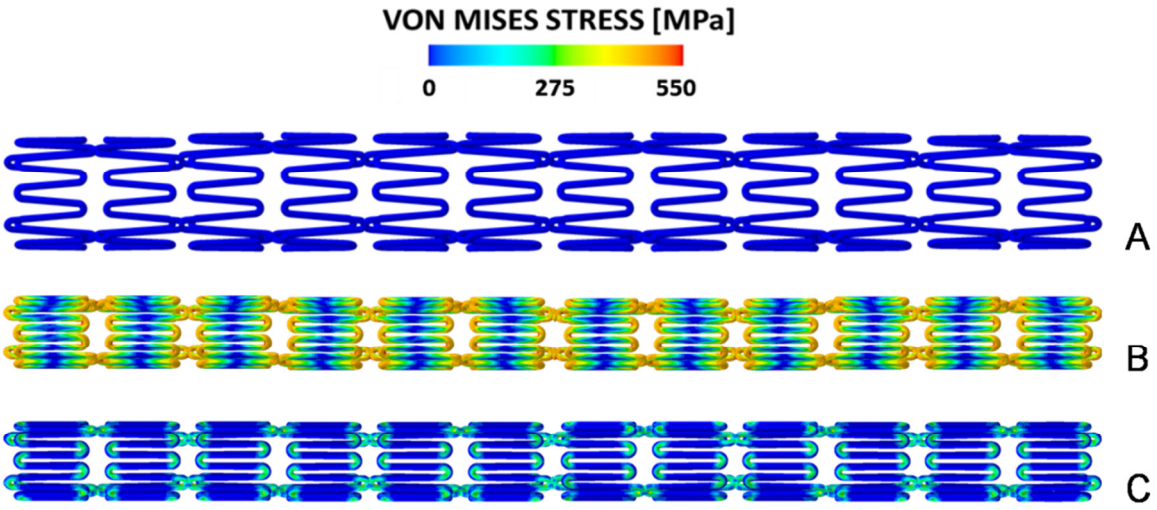

Figura 6 – Mappe degli sforzi di Von Mises nel modello di stent durante crimping. Viste longitudinali in configurazione iniziale (A), a crimping massimo (B) e dopo ritorno elastico (C).

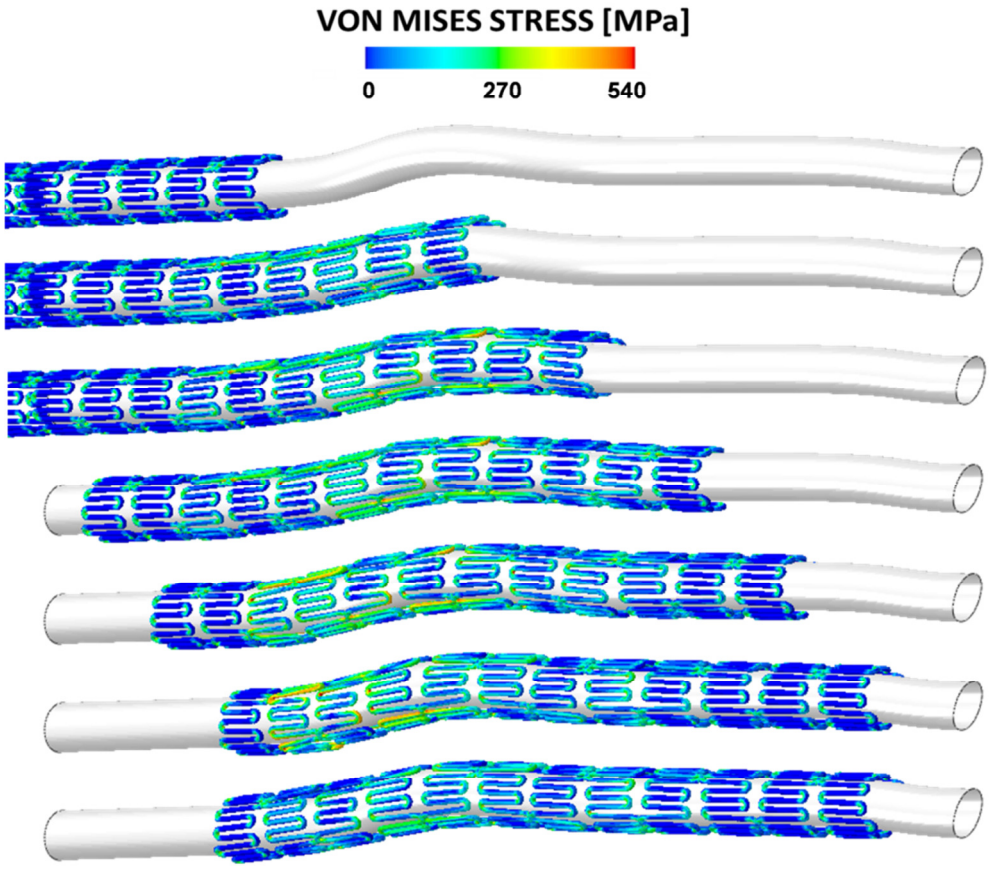

Figura 7 – Avanzamento dello stent prossimale lungo la guida basata sulla centerline del lume post-angioplastica.

3.2 Procedura clinica simulata

L'analisi computazionale della procedura di stenting è mostrata nelle varie fasi in Figura 8. La distribuzione degli sforzi di Von Mises è rappresentata in Figura 9, evidenziando i picchi di sforzo locali ottenuti nei tratti curvi delle maglie e il leggero aumento nella regione di sovrapposizione dei due stent. La risposta dell'arteria (vedi Fig. 10) è stata analizzata in termini di sforzi principali massimi, identificando le regioni della parete coronarica potenzialmente più inclini a restenosi. Le zone vascolari più critiche, maggiormente portate a un successivo ispessimento della neointima, sembrano essere la regione di sovrapposizione degli stent e la zona prossima al secondo ramo diagonale.

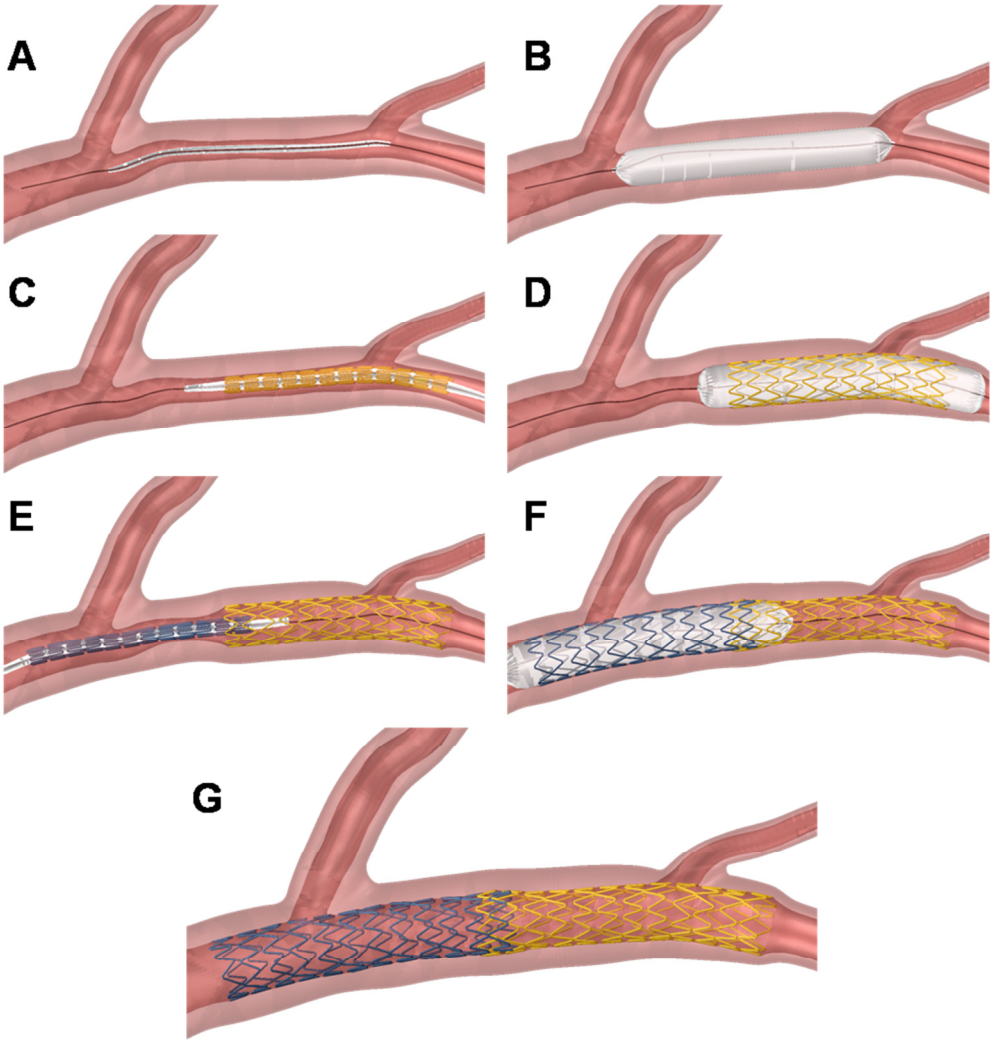

Figura 8 –Simulazione della procedura clinica effettuata. Inserimento del pallone per angioplastica (A), intervento di angioplastica (B), inserimento dello stent distale con pallone (C), espansione dello stent distale (D), inserimento dello stent prossimale con pallone (E), espansione dello stent prossimale (F) e configurazione finale dopo ritorno elastico (G).

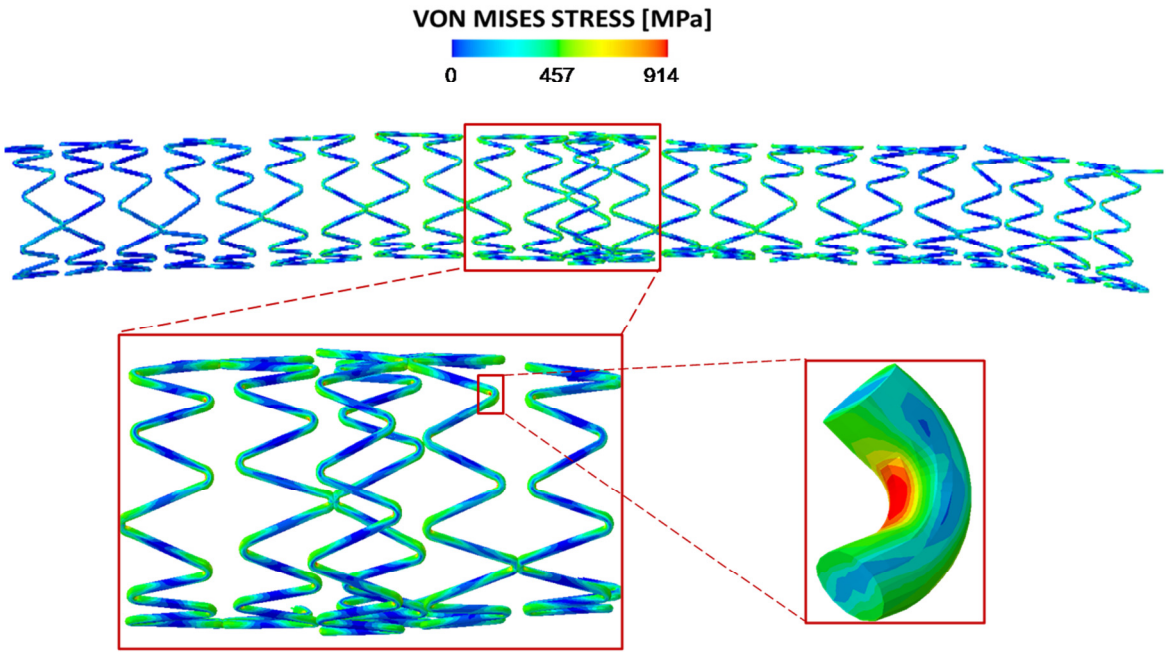

Figura 9 – Mappa degli sforzi di Von Mises sui due stent coronarici impiantati. Zoom sulla regione di sovrapposizione e sul massimo sforzo ottenuto lungo una maglia curva.

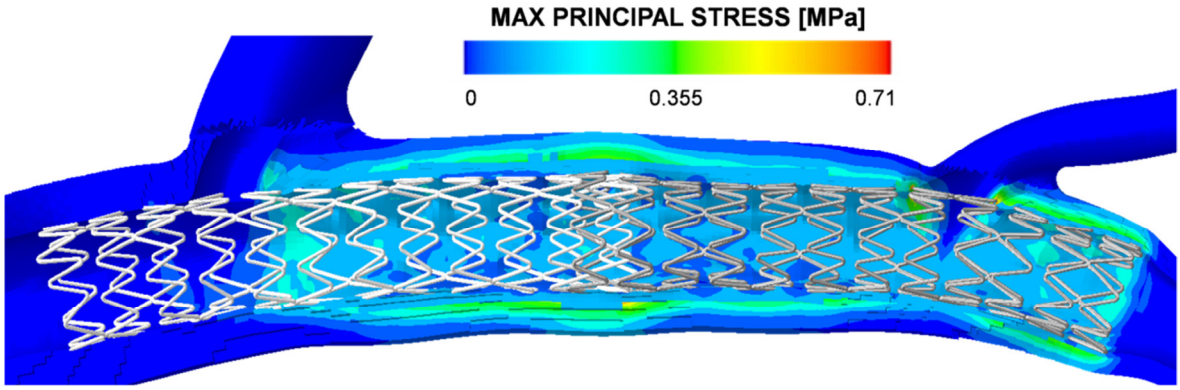

Figura 10 – Distribuzione degli sforzi massimi principali lungo la parete arteriosa rimanenti in seguito alla procedura di stenting.

Inoltre, i risultati della simulazione numerica sono stati confrontati con il reale intervento avvenuto, analizzando le due geometrie del lume post-stenting (vedi Fig. 11). Le due geometrie mostrano una buona corrispondenza. Tuttavia, si possono trovare alcune differenze, tra cui il maggiore raddrizzamento del vaso nel lavoro computazionale. Tale risultato potrebbe essere spiegato con l'assenza nel modello di tessuti circostanti o a causa di una caratterizzazione meccanica delle placche aterosclerotiche solo ipotizzata.

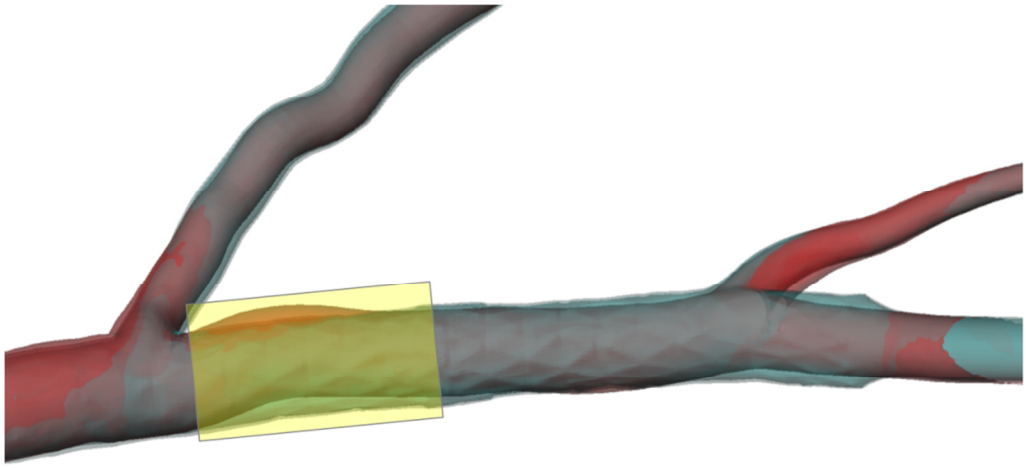

Figura 11 – Confronto del lume arterioso post-stenting tra il reale intervento avvenuto (rosso) e i risultati computazionali (blu). Il maggiore raddrizzamento ottenuto nel lavoro numerico è evidenziato in giallo.

4. Conclusioni

Il presente lavoro dimostra la fattibilità dell'implementazione di un modello virtuale *patient-specific* replicando casi clinici reali. Una procedura di stenting avvenuta è stata simulata usando il metodo degli elementi finiti, per mezzo di un'accurata ricostruzione 3D della regione di biforcazione coronarica e di geometrie CAD create a somiglianza dei dispositivi commerciali utilizzati. Il modello è stato analizzato in termini di sforzi e deformazioni ottenute e, in seguito, confrontato con il reale lume ottenuto al termine dell'intervento. Tali analisi computazionali potrebbero essere utilizzate per confrontare diverse opzioni cliniche, facilitando in tal modo il planning dell'intervento. Inoltre, sviluppi futuri attualmente in corso riguarderanno delle analisi fluidodinamiche, valutando l'effetto del trattamento da quest'altro punto di vista. L'influenza biomeccanica della procedura di stenting valutata in questo modello *patient-specific* sarà poi confrontata con il follow-up clinico a 6 e 12 mesi.

Introduction

The present work, carried out at the Laboratory of Biological Structure Mechanics (LaBS), aimed to achieve a finite element model to simulate patient-specific stenting interventions in coronary bifurcations. In particular, an actual stenting procedure performed at Hospital Doctor Peset (Valencia, Spain) was replicated computationally. The arterial geometry was generated based on vascular imaging techniques, while the intravascular devices used were recreated based on the procedural indications provided by the clinicians. The current state-of-the-art in finite element works simulating stenting procedures lacks patient-specificity, mostly utilizing idealized geometries. The use of image-based arteries could greatly improve stenting procedures, predicting the results of various clinical options and thus facilitating intervention planning.

A brief description of the thesis structure is here presented.

In the first chapter, the vascular imaging techniques are shortly overviewed. Subsequently, the state-of-the-art of image-based geometric modeling of coronary artery is discussed, concentrating on a novel reconstruction technique. Furthermore, the image-based modeling of medical devices is briefly examined.

In the second chapter, the most recent finite element models simulating angioplasty procedures and stenting intervention in simple and in tortuous vessels based on patient-

specific reconstructions are presented. Moreover, the main limitations of the current state-of-the-art are briefly highlighted.

The third chapter clarifies the choice of the balloon model used for the finite element work. A comparison is carried out between two balloon configurations, investigating the effects of the use of a more realistic model.

In the fourth chapter, the structural model of the real clinical intervention is described. The steps carried out to achieve a realistic 3D reconstruction of the coronary bifurcated region are explained, as well as the methods used to create CAD geometries of the intravascular devices used in the stenting procedure. Also, the final simulation details are described, as well as the preliminary analyses (crimping and bending) performed in order to make the final analysis possible.

The fifth chapter shows the results obtained and discusses the outcomes in terms of geometrical considerations and of mechanical stresses and strains obtained on the stent models and on the arterial wall. Furthermore, a comparison between the finite element results and the actual intervention is made.

In the sixth chapter, the main conclusions are reported, followed by the limitations of the presented model and its possible further developments.

.

Chapter 1

Coronary imaging techniques and reconstruction of 3D vessel models

---

In the first chapter, the vascular imaging techniques are shortly overviewed. Subsequently, the state-of-the-art of image-based geometric modeling of coronary artery is discussed, concentrating on a novel reconstruction technique. Furthermore, the image-based modeling of medical devices is briefly examined.

1.1 Coronary artery imaging techniques

Coronary imaging is still an open challenge for any medical imaging operators. The main reason is that coronary arteries are small (2-4 mm in diameter), have a tortuous, complex, three dimensional paths and are continuously in motion [1]. Beside ordinary requisites, such as complete diagnosis capability, accuracy and limited invasiveness, coronary imaging has two important technical requirements: high temporal resolution, to overcome the constant motion during both the respiratory and the cardiac cycle, and high spatial resolution to provide accurate imaging of very small vessels [2].

Angiography is the standard clinical test for advanced coronary artery disease, but recently computed tomography angiography (CTA), magnetic resonance imaging (MRI), intravascular ultrasonography (IVUS) and optical coherence tomography (OCT) have been proved able to accurately provide further anatomical and functional information.

The main coronary imaging techniques are briefly described below, followed by Table 1.1 summarizing some of their main features.

1.1.1 Conventional coronary angiography

Conventional coronary angiography (CCA) is the gold standard for coronary assessment. It identifies luminal dimension detecting stenotic lesions, with 2D images of the vasculature. CCA has better temporal and spatial resolution compared to CTA and MRI techniques. Figure 1.1 is an example of a CCA image highlighting a stenosis. The main drawback of this imaging method is its high invasiveness, since it requires catheterization, with associated risks of arterial puncture, the injection of an iodinated contrast medium and patient radiation exposure to X-rays [2]. CCA is only able to identify the arterial lumen without detecting wall thickness and plaque extension. Thus, CCA is unable to predict the development of atherosclerotic vessels [3]. It also provides no information on plaque composition and microvasculature [4].

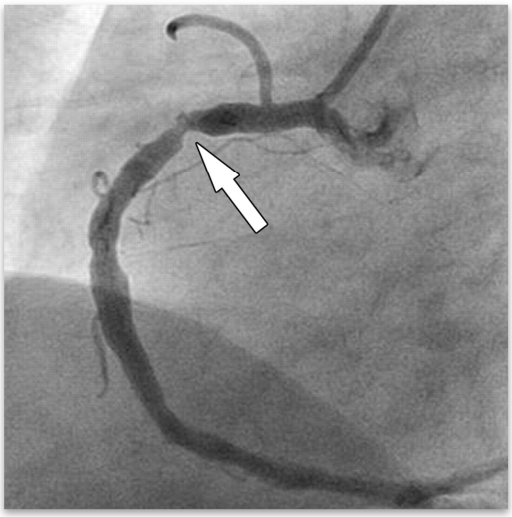

Figure 1.1- Angiographic 2D image of a coronary artery. The white arrow indicates a stenotic region [5].

1.1.2 Computed tomography angiography (CTA)

The rise of CTA has opened the possibility for non-invasive imaging of the coronary arteries [2]. Moreover, CTA can provide more information regarding coronary disease. Indeed, tomographic coronary imaging tests allow early and direct assessment of atherosclerotic plaques: recent trials have proved CTA able to identify plaque area, degree of stenosis and vessel wall morphology. Furthermore, when associated with an intravenous contrast medium, CTA is capable of identifying calcified and non-calcified lesions, distinguishing soft, intermediate and hard plaque [3]. This technique is not time-consuming and is continuously improving its spatial resolution, reaching 0.5 mm in most recent scanners. Its major drawback is low temporal resolution, important to freeze cardiac motion and achieve an optimal CTA, making image quality susceptible to high heart rate and arrhythmia [2]. Correspondingly, this technique requires a heavy radiation exposure and is unable to image lesions with heavy calcium burden [6]. The acquired images are 3D images, useful for a better investigation of coronary morphology and geometric 3D reconstructions. An example is shown in Figure 1.2.

Figure 1.2–CTA image of coronary arteries [7].

1.1.3 Magnetic resonance imaging (MRI)

Magnetic resonance imaging (MRI) of coronary arteries is the safest and the only fully non-invasive diagnostic method, since there is no radiation exposure nor iodinated contrast [8]. Compared to CTA, MRI has higher temporal resolution and lower spatial resolution [2]. Recent developments make this technique capable of plaque characterization, including size, composition and inflammatory status, besides the ability of detecting microvascular obstruction (Figure 1.3). However, although MRI angiography has generated promising data in recent trials, its long image acquisition times, together with a limited contrast-to-noise ratio, hinder its consistent application in clinical use [4]. A method to acquire better quality images and improve the signal-to-noise ratio is to associate MRI with a contrast medium injection, but this would nullify the non-invasiveness of this technique. Also, patients with metallic devices, such as pacemakers and stents, cannot undergo MRI acquisition.

1.1.4 Intravascular ultrasonography (IVUS)

Intravascular ultrasound (IVUS) is an invasive modality which provides cross-sectional images of coronary arteries, as shown in Figure 1.4. Such images identify both the lumen and the outer vessel wall, providing accurate estimations of their dimensions and of the plaque burden [9]. IVUS also allows the differentiation of morphological characteristics between culprit and non-culprit plaques and identifies their calcification degree. Nevertheless, the invasiveness of this technique makes it not ideal for patients that did not undergo CCA. Its spatial resolution is limited if compared to other invasive methods.

Figure 1.3- MRI coronary angiography highlighting a heavy bifurcation stenosis (white arrow) and some of the main coronary vessels [4].

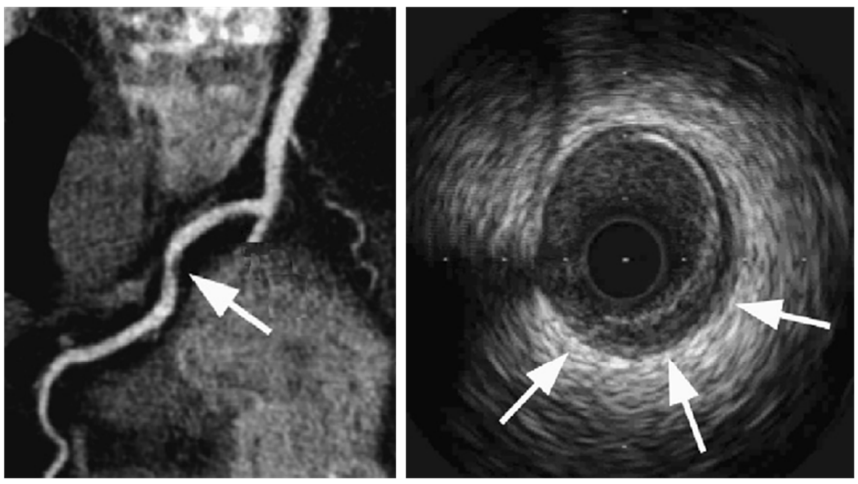

Figure 1.4 – On the left a CT image of a stenotic coronary artery, on the right the IVUS image of the cross section of the indicated area. The three white arrows show the plaque, accurately detected [10].

1.1.5 Optical coherence tomography (OCT)

Optical coherence tomography (OCT) is a recent invasive intravascular technology, characterized by the unique ability to detect atherosclerotic lesions in microscopic detail, particularly those lesions believed to be prone to sudden rupture [11]. As IVUS, it provides cross sectional images of vessels, as shown in Figure 1.5. Among the recent coronary imaging techniques, OCT has the high spatial resolution, about 10 times if compared to IVUS [6]. This technology is able to identify culprit plaques by clearly visualizing large lipid cores and can accurately assess inflammation. Also, optical coherence tomography detects metal materials, so OCT is the highest resolution vascular technique able to identify both stent and arterial wall. As a result of the excellent spatial resolution, stent struts are clearly defined, as shown in Figure 1.6. Besides invasiveness, main disadvantages of OCT are its limited depth penetration and that it is quite time consuming. Moreover, each coronary artery must be imaged separately making this technique unable to acquire an entire bifurcation in a single scan [6].

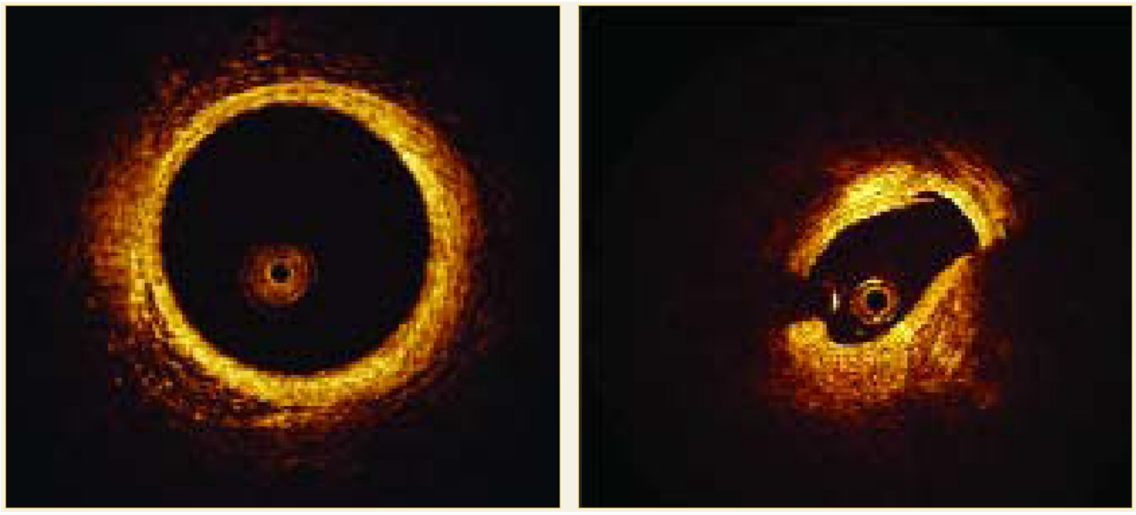

Figure 1.5 – Two OCT images of coronary artery cross sections. On the left a normal appearing artery, on the right a stenotic artery with remarkable lumen narrowing [11].

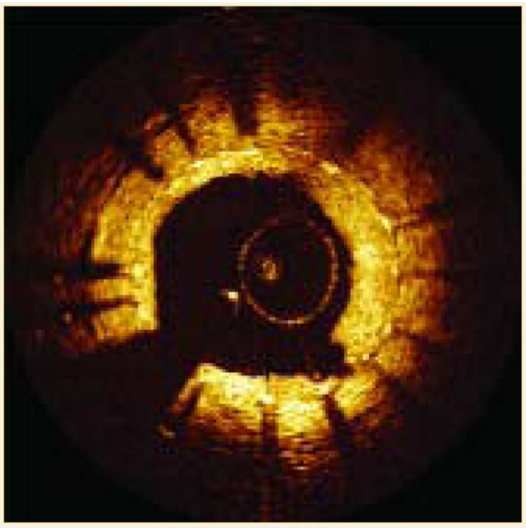

Figure 1.6 – OCT image of a cross sectional arterial view after stent implantation. Stent struts are clearly defined [11].

Table 1.1 – Advantages and disadvantages for CCA, CTA, MRI, IVUS and OCT. Grading goes from +++ (most) to – (least), X indicates ability [2, 11].

	CCA	**CTA**	**MRI**	**IVUS**	**OCT**
SPATIAL RESOLUTION [µm]	100 - 200	500 - 600	1000	80 - 120	10 – 20
TYPE OF RADIATION	X – rays	X – rays	Radio waves	Ultrasound	Near-IR light
HEAVY RADIATION EXPOSURE	++	+++	-	-	-
INVASIVENESS	+++	+	-	+++	+++
CORONARY ASSESSMENT	+++	++	+	+++	+++
PLAQUE DETECTION		X	X	X	X
PLAQUE COMPONENTS DETECTION				X	X

1.2 Image-based geometric modeling

Much effort has been made over the last decade to reconstruct three dimensional geometries of coronary arteries from medical images. The typical steps required for a mesh generation are shown in Figure 1.7. 3D imaging, such as CTA and MRI techniques, allow a 3D reconstruction of the vessel geometry, while cross-sectional imaging, such as IVUS and OCT, can be used to provide further information on vessel wall and lumen boundaries.

The first and arguably most important step in the image-based modeling process is the extraction of the vessel skeleton from images of the vascular anatomy [13]. Depending on the type of images available, the skeleton is reconstructed using the boundaries of the lumen and/or on the outer wall [12]. Much research over the past decade has focused on this process, with studies relying on manual or computer-assisted segmentation of individual image slices, coupled to 3D reconstruction techniques. The vessel boundary must be determined in order to identify the centerline and compute the radius as the distance between the centerline and the boundary [14]. In order to generate the vessel surface it is possible to loft the series of lumen and/or wall "rings" together (see Steps 4 and 5 in Figure 1.7), usually followed by surface smoothing [13].

For straight or curved vessels without branches, such as coronary artery segments, it is straightforward to connect corresponding points around the vessel circumference, using

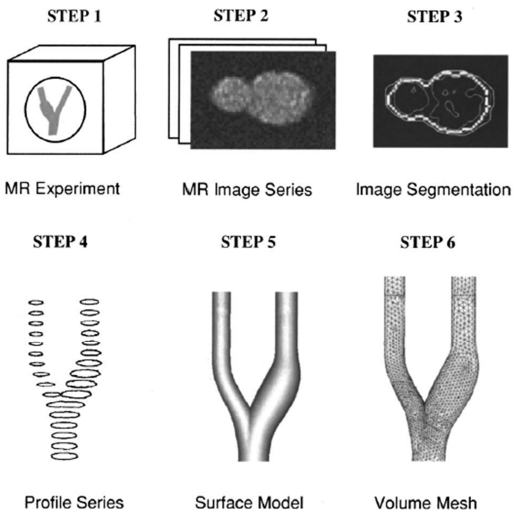

Figure 1.7 – Summary of the steps required for the construction of a finite-element mesh from MRI images of a coronary bifurcation [12].

splines or filtering techniques to achieve the desired level of smoothing. For bifurcating or branching vessels the surface generation is more ambitious; a common approach is to reconstruct each branch separately and then merge them using solid modeling operations [12].

As briefly described (see Paragraph 1.1), recent improvements in the spatial resolution and quality of medical images has made it much easier to perform 3D vessel extraction. Also, depending on the image type, segmentation methods vary: for volumetric images having well-defined lumen-wall boundaries, such as those obtained from CTA or contrast-enhanced MRI, 3D segmentations are preferred for their convenience, speed and robustness, while 2D segmentation remains the best option for biplane IVUS medical images [13].

The final but key step in the vessel reconstruction process is the discretization of the complex model into finite elements or volumes, whose size and distribution largely govern the accuracy of the 3D reconstruction. If the geometry has to undergo computational simulations, a nontrivial balance must be struck between solution accuracy and computational effort. For simple geometries, that are topologically equivalent to straight tubes, such as coronary artery segments, meshing is fairly uncomplicated and can be automated by dividing the tube-like structure into a fixed number of points around the circumference and along the vessel axis, generating structured meshes. Such meshes may also be computed for bifurcating geometries, though considerably more effort is required to ensure the element quality. More popular are unstructured meshes in which arbitrary distributions of tetrahedral, hexahedral or prismatic elements are generated using specific sophisticated algorithms [12].

1.2.1 State-of-the-art of coronary artery 3D reconstruction

Following the guidelines for the 3D reconstruction of coronary vessel geometry, several approaches have been attempted in the last decade, utilizing different medical images. The surfaces and the following meshes that are created strongly correlate with the image quality and resolution. Earlier methods proposed to reconstruct geometries from one type of medical image, while recently the trend is to combine different images to more accurately build the vessel surface.

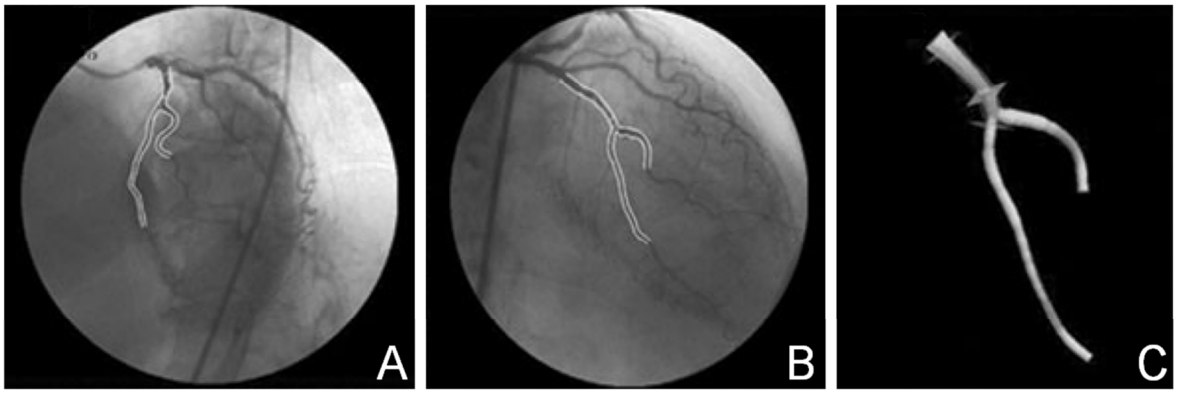

Figure 1.8 - On the left and in the middle, two conventional coronary angiography images taken from different angles. On the right, the 3D reconstruction generated by Galassi et al. [15].

Galassi et al. have proposed a three dimensional reconstruction of coronary bifurcation based on 2D CCA images, made in standard clinical tests. As shown in Figure 1.8, their novel 3D reconstruction system well reproduces a solid image starting from simple biplane angiographies [15]. Dvir et al. also successfully generated 3D models of coronary bifurcation using 2D angiographies taken from different angles of projection, and utilized the solid geometries to investigate morphological changes occurred after treatment [16].

Other trials have been carried out utilizing 3D clinical images that could follow vessel directions in space more precisely. Antiga et al. were able to reconstruct various arterial bifurcations using only CTA images, proposing a fast, accurate and reproducible technique. The study developed a methodology to build and analyze patient-specific 3D geometrical models and to generate high quality hexahedral meshes semi-automatically [17]. Attempts have also been made to model vessel geometries from contrast-enhanced MRI angiography. Bijari et al. reconstructed arterial bifurcations utilizing magnetic resonance images only, and achieved high quality surfaces in a reasonable time [18].

Other procedures to generate a realistic 3D lumen and vessel wall reconstruction rely on the combination of different imaging techniques, in particular to add the high resolution cross sectional views of IVUS or OCT, improving accuracy in the determination of lumen area and wall thickness. The combination of biplane angiography and IVUS was validated and used in many clinical investigations. This technique, named ANGUS, has the main advantage that the centerline and IVUS imaging are virtually simultaneous, and that it does not rely on the selection and matching of anatomical landmarks [19]. Many authors have combined CCA and IVUS to obtain three-dimensional reconstructions of coronary arteries

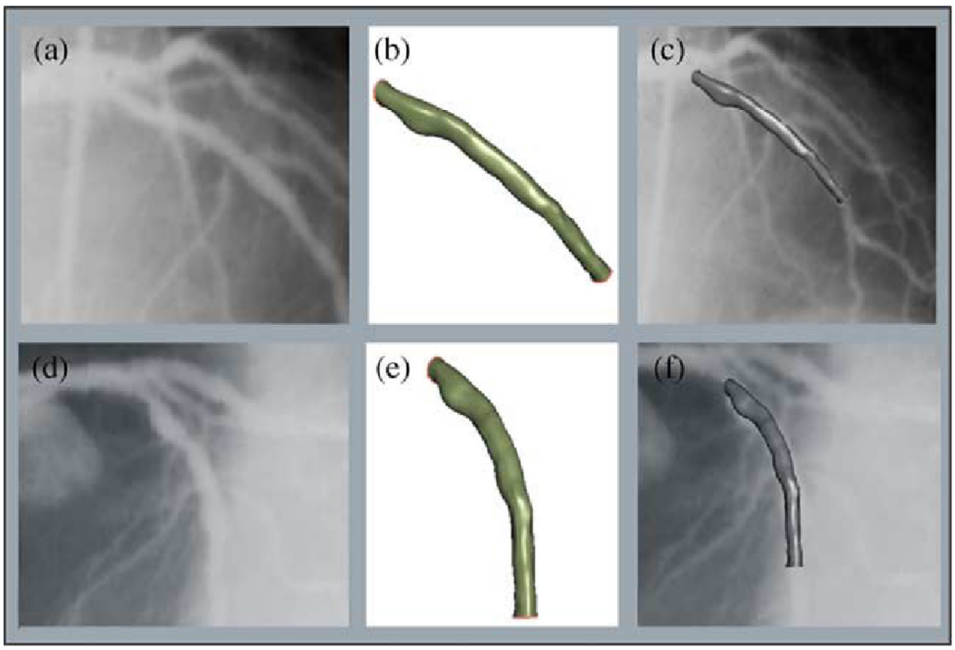

Figure 1.9 – Biplane projection of a coronary artery (a, d). The 3D reconstruction of a segment is depicted in figures b and e. As it is shown in figures c and f, the reconstructed coronary segments match well the lumen's silhouette [21].

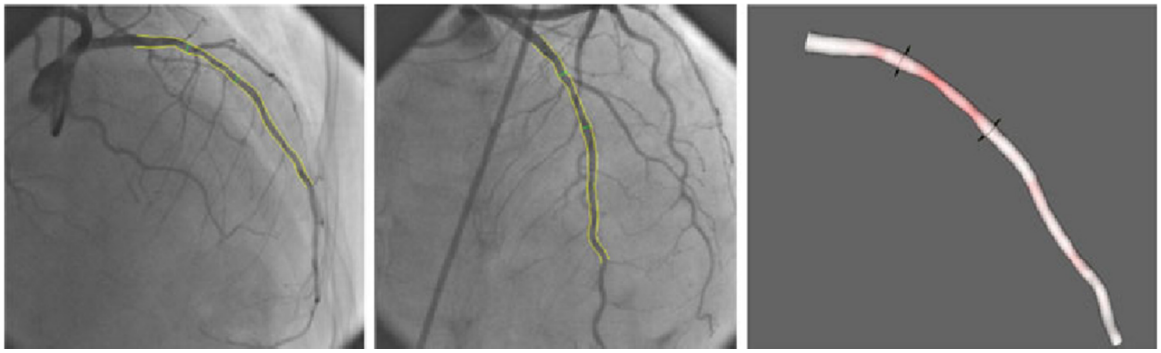

Figure 1.10 – Two biplane CCA images taken from different angles of projection (left and center) and the solid geometry reconstructed using IVUS cross sectional images (right) [22].

and their quantitative validation [20, 21]. The vessel path is identified from 2D angiographies, while IVUS images provide the sections to obtain accurate geometries. Examples of the results of these works carried out are shown in Figures 1.9 and 1.10.

OCT imaging can also be used combined with CCA to obtain reconstructions that provide detailed information about lumen area and plaque size at every position along the vessel of interest [22]. Recently, procedures combining CTA and IVUS images have been used to obtain the 3D reconstruction of coronary arteries. Van der Giessen et al. first acquired vessels 3D centerlines from CTA, and secondly positioned IVUS images containing lumen

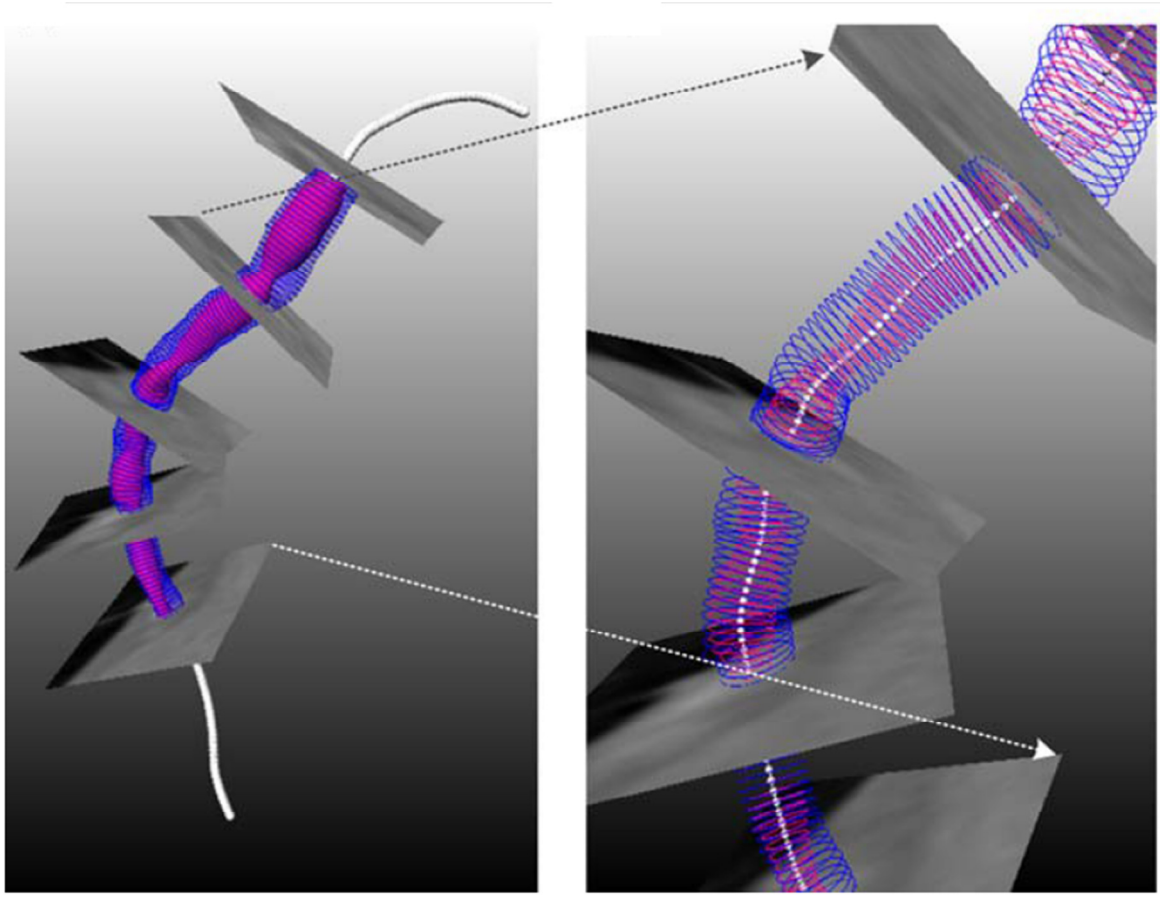

Figure 1.11 – The IVUS 2D images are placed on the CT derived centerline at correct locations, generating the coronary artery geometry. Pink curves represent the internal lumen, blue ones the exterior wall. On the right, a magnification of the 3D contours [19].

and wall contours perpendicularly to the centerline, thus neglecting the IVUS catheter orientation [19]. The procedure is shown in Figure 1.11.

1.2.2 A novel reconstruction technique: CCA and CTA

As described in the previous paragraph, several approaches have been proposed to obtain accurate segmentations of coronary arteries. However, most of the studies are based on information resulting from only one image modality; others utilize IVUS images that are quite unusual due to their highly invasivity and expense. Therefore, in 2011 Cárdenes et al. developed a method to combine CTA and CCA, taking advantage of each one to overcome the limitations of the other. It is the first work that combined these two modalities for reconstruction of coronary artery bifurcations [23]. Also, Cárdenes et al. analyzed vessels that underwent stenting surgery examining pre- and post-operative conditions.

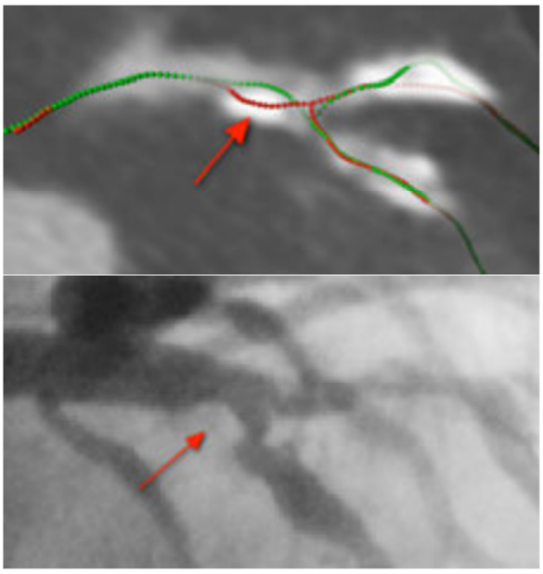

Figure 1.12 – Top: centerlines of the post (red) and pre (green) operative models, avoiding the calcified plaque pointed by a red arrow. Bottom: corresponding CCA image, which better highlights the stenosis [23].

The method proposed consists of three steps. First, the 3D structure of the bifurcation is obtained by CTA pre-operative data. The CTA image is used to extract the information of the vessel centerlines forming the bifurcation. To take into account the calcified tissues of the plaque, that if present are visible in CTA images, the calcifications are subtracted from the CTA image and the centerline is re-computed. Therefore, the final pre-operative centerlines deviate with respect to the previous ones at calcified lesions, as shown in Figure 1.12.

Secondly, CCA images obtained before and after endovascular treatment are processed to obtain the vessel radii along the vessel centerlines. Two images are selected from pre and post operative views, using an angle where the area of projection of the bifurcation is maximum. This projection corresponds approximately to the CCA image chosen by the clinician for an optimum visualization of the bifurcation. As only vessel radii and lengths are used from CCA, there is no need to have perfect matching between CCA and CTA images.

Finally, the models are constructed mapping the vessel radii from 2D to the 3D structure. Circular cross section is assumed for the arteries without losing too much accuracy in the majority of cases. Results have proved to be highly accurate and are considered satisfactory by visual inspection and in comparison with manual measurements.

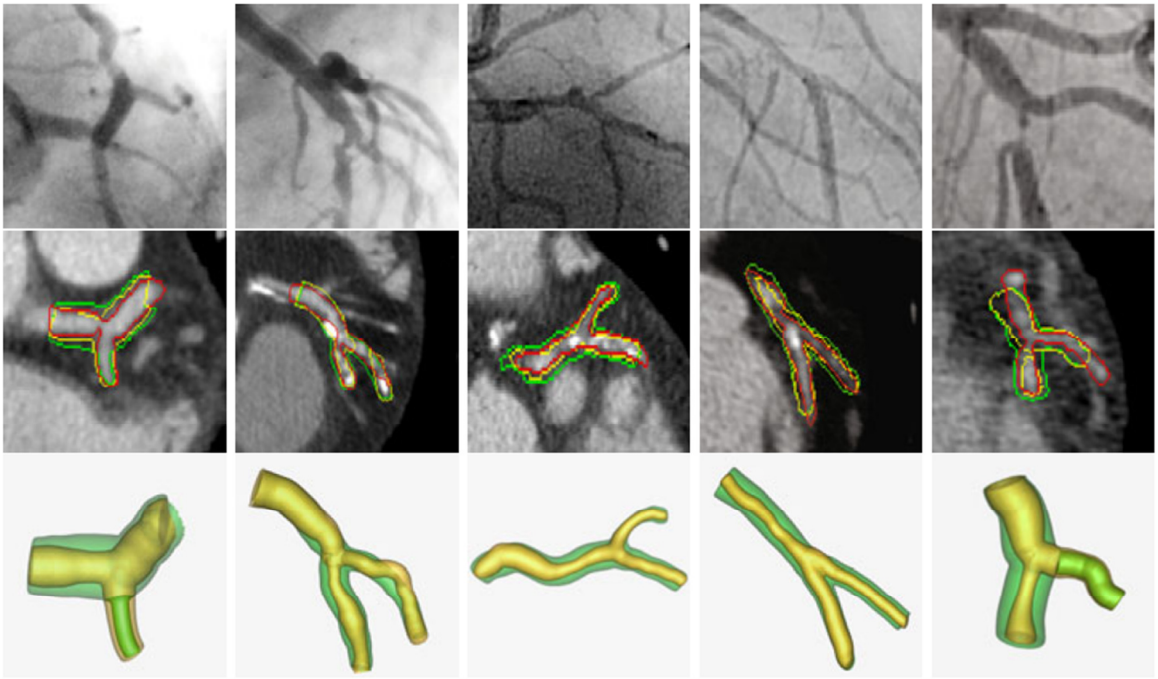

Figure 1.13 – Top row: CCA images of the coronary bifurcation investigated. Middle row: CTA images with manual segmentation (red), pre (yellow) and post (green) outlines detected. Bottom row: 3D geometrical models of the bifurcations, with inner lumen referred to the pre (yellow) and the post (green) operative models [23].

Correspondence between CCAs, CTA images and the realistic 3D bifurcation geometries is shown in Figure 1.13.

1.2.3 State-of-the-art of medical device 3D reconstruction

Medical images have been used not only for vasculature reconstruction, but also for medical device geometry creation. As far as coronary stenting intervention is concerned, studies have been carried out reconstructing balloon and stent models.

De Beule et al. (2008) were able to recreate the trifolded pattern of a commercially available balloon. The study was based on micro-CT images of the unexpanded balloon-catheter assembly, shown in Figure 1.14. By means of image examination, the balloon thickness and the inner shaft diameter were detected, making the following computational analysis more realistic [24].

Figure 1.14 – Micro-CT based reconstruction of the trifolded balloon, coupled with the cylindrical inner shaft [25].

Computed tomography images have also been used for the reconstruction of commercial stent geometries. Connolley et al. (2007) acquired X-ray micro-tomography images from *in-vitro* stent expansion performed in a mock silicone artery. In order to obtain correct geometrical information, the sample was rotated to acquire the different projections required for tomographic reconstruction, for a total of 900 projections per scan. The images were taken at different stages of stent deployment, to assess the progress of stent expansion. Figure 1.15 shows two 3D reconstruction of the stent during balloon expansion. The device was accurately reconstructed, as the geometrical parameters match the ones assessed from the tomography acquisitions [26]. The results of the work not only proved the use of CT images to reconstruct medical devices geometries, but also demonstrated the feasibility of numerical analyses utilizing such models, in order to obtain more accurate and realistic results.

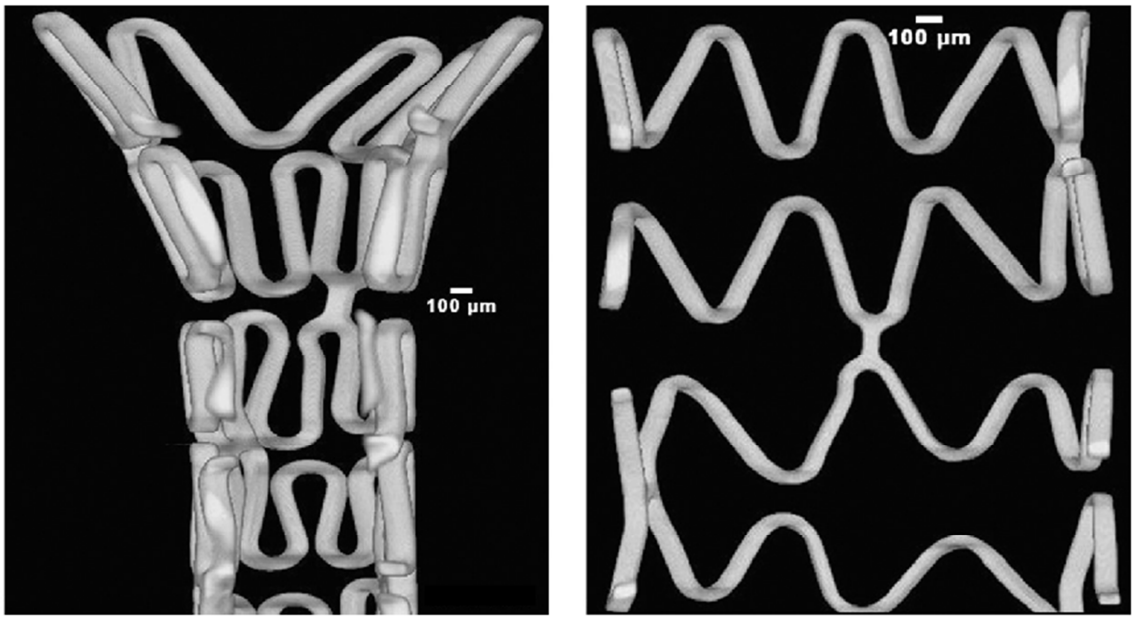

Figure 1.15 – 3D longitudinal sections of the reconstructed volume of the stent during (left) and after (right) in vitro balloon expansion [26].

Chapter 2

Image-based finite element models: state-of-the-art

In the second chapter, the most recent finite element models simulating angioplasty procedures and stenting intervention in simple and in tortuous vessels based on patient-specific reconstructions are presented. Moreover, the main limitations of the current state-of-the-art are briefly highlighted.

The finite element method (FEM) and, in general, numerical methods have emerged as an essential and widely adopted tool for the assessment and optimization of biomedical devices such as coronary stents. Over the past decade, increasing levels of computational power and physiology knowledge have led to a high level of complexity and sophistication involved in these studies. Nevertheless, there is a need to investigate the performance of these devices within realistic models of diseased arteries. This improvement can be achieved by means of the previously reported image-based models (see Paragraph 1.2). The coupling of patient-specific atherosclerotic artery models and advanced computational simulations has the potential to provide a scientific basis for the identification and optimization of suitable stent geometries and materials in the treatment of coronary artery diseases for specific cases [27].

The main structural works found in literature following this line of thought are listed below, focusing on the reconstruction technique and the ability to create complex realistic arterial geometries. The numerical simulations will be briefly reviewed and subsequently the main limitations will be examined.

2.1 State-of-the-art of image-based finite element artery models

Computational studies based on vessel reconstructions from medical imaging are strongly dependent on the image type. Cross sectional views of arterial segments, provided by acquisition methods like OCT and IVUS, allow the generation of two-dimensional geometrical models, while images showing the complete vessel morphology, such as MRI and CTA, allow 3D reconstructions of patient-specific arterial geometries. The combination of different medical imaging types is preferred, as each one can overcome the limitations of the other. Following this direction, cross sectional 2D images can be associated to a 3D vessel path in order to reconstruct a realistic arterial segment.

2.1.1 Angioplasty intervention simulations

Chau et al. (2004) proposed the first use of optical coherence tomography as a basis for finite element analysis. The study aim was to simulate the angioplasty procedure by assessing the mechanical response of coronary atherosclerotic plaques to inner pressure. The gold standard for determining plaque geometry and composition has always been histology, despite the processing technique is known to cause geometry artifacts [28]. OCT is able to overcome these limitations and allows an accurate characterization of vessel and plaque components, as shown in Figure 2.1. Moreover, OCT has the great advantage to be an *in vivo* procedure, making reconstruction possible on effective patients.

A structured finite element mesh was created using 2D plane elements, as shown in Figure 2.2. The structural mechanical analysis of inner pressure application was performed by the commercial finite element software package ADINA (Watertown, MA, USA). Chau et al. compared numerical tests based on OCT with traditional ones based on histology, highlighting the smoother lumen boundaries and the absence of processing artifacts in the OCT-based model, with similar stress and strain distributions [28]. Results demonstrated not only the feasibility of image-based models use, but also a higher accuracy achieved.

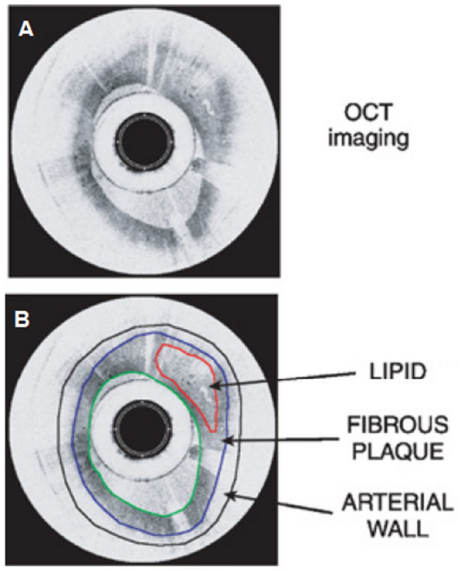

Figure 2.1 – OCT image of a lipid-rich coronary plaque cross section (A) and the following segmentation allowing tissue differentiation (B) [28].

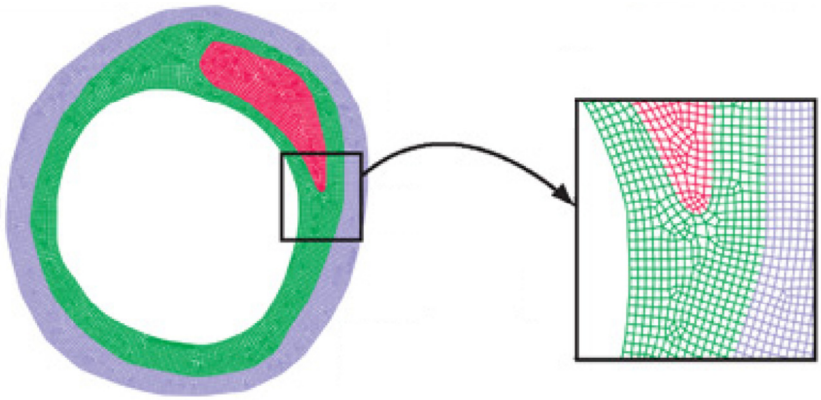

Figure 2.2 – Structured finite element mesh generated, with close-up [28].

The response of plaque, and more generally the overall response of vascular tissue components to balloon angioplasty was also investigated by Kiousis et al. in 2007, by means of a 3D numerical simulation based on magnetic resonance imaging. The work modeled a patient-specific geometry from high resolution MRI data of a stenotic iliac artery. As a result of a 3D semi-automatic segmentation, the most important tissue boundaries were traced, identifying seven different tissue components, as shown in Figure 2.3.

In order to reduce computational power, the 3D reconstruction was subsequently simplified, reducing the number of tissue components and considering just a slice of the atherosclerotic lesion [29]. Numerical analyses were implemented into the finite element software FEAP (Berkeley, CA, USA). The effect of balloon inflation was examined by placing a circular cylinder with continuously increasing diameter, and the obtained results are shown in Figure 2.4.

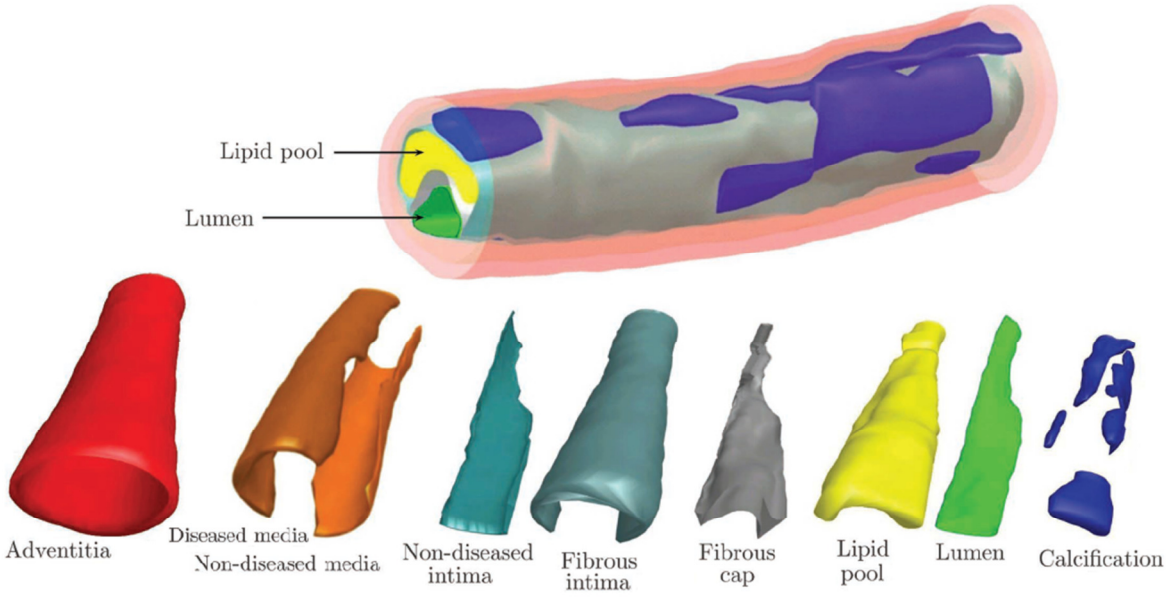

Figure 2.3 – Three-dimensional reconstruction of the diseased iliac artery, and representation of all the different tissue components detected [30].

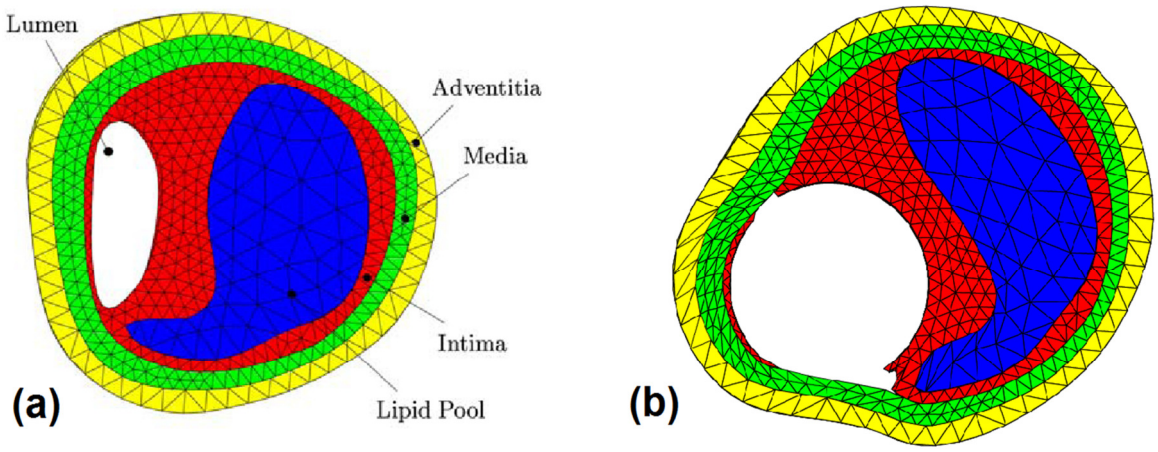

Figure 2.4–Model used for the numerical simulations of balloon angioplasty before (a) and maximum expansion (b) during the procedure [29].

2.1.2 Stenting procedure simulations in linear artery segments

Holzapfel et al. (2005) presented results from a study carried out to investigate the effect of geometrical parameters such as stent cell size and strut thickness on the biomechanical impact of the three different stents expanded within a realistic, patient-specific model of a linear stenotic artery. To the best of the author's knowledge, this is the first structural work of stent deployment using image-based geometrical models. The 3D reconstruction was

based on high resolution magnetic resonance images of a postmortem iliac artery segment presenting stenosis. The medical images, coupled with histological analysis, allowed the detection of eight different tissue types. For each scanned MRI cross sectional image, the borders of the arterial components were traced automatically by a set of points. These points were then fitted by non-uniform rational B-splines (NURBS) curves, which were combined along the arterial axis in order to obtain the boundary surfaces of the different tissue components. The geometry of the stenotic iliac artery is shown in Figure 2.5.

In order to model the material response, each component of the stenotic segment was assumed to behave as a composite reinforced by two families of collagen fibers. Finite element meshes were generated using a built-in software, able to parameterize and automatically generate differently dense meshes. Three commercially available stent models were expanded in the reconstructed geometry applying pressure directly on the inner surface of the struts, exhibiting different mechanical and geometrical results [31]. The results are shown in Figure 2.6, highlighting the circumferential stress distribution. The presented study gave a new perspective to structural computational analysis of stent deployment, highlighting the potential of FEM utilizing realistic, patient-specific diseased vessels.

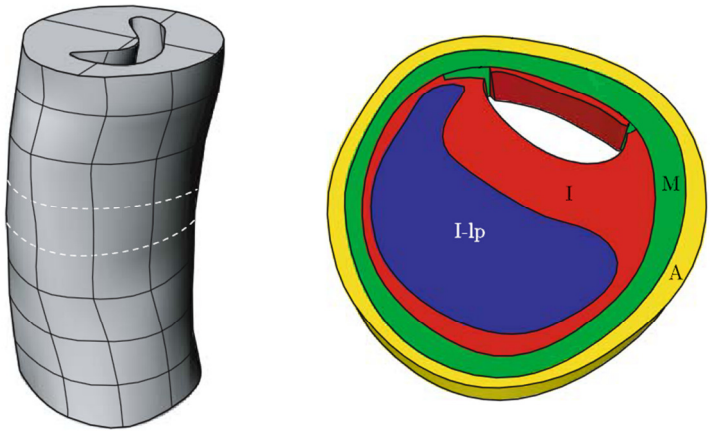

Figure 2.5–3D geometrical model of the iliac artery segment reconstructed by means of NURBS [32].

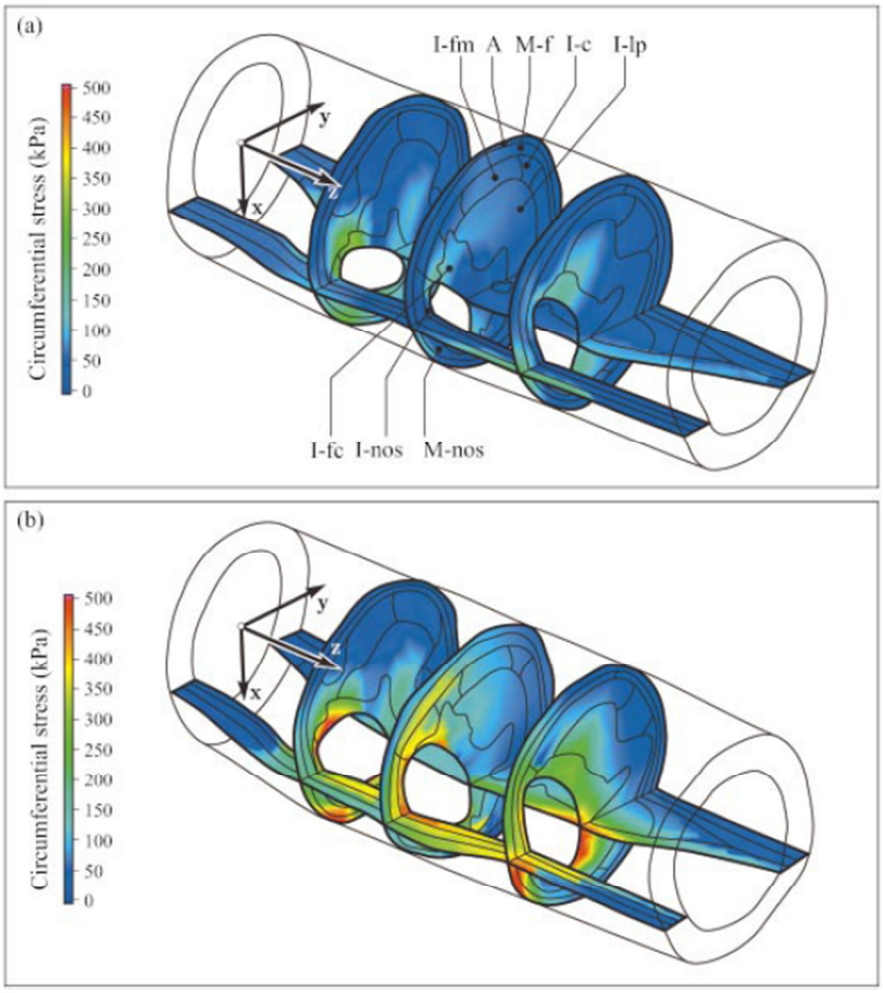

Figure 2.6 – Circumferential Cauchy stress distribution in the stenotic arterial wall before (a) and after (b) stenting procedure. The top figure highlights the eight tissue types detected [31].

Following the direction of image-based computational simulations of stent deployment, Gijsen et al. (2008) investigated the effect of a coronary stent expansion within a patient-specific model of a stenotic artery. The reconstruction was based on biplane angiography and intravascular ultrasonography of a right coronary artery achieved prior to the stenting intervention. First, the CCA images were selected at end-diastole, to eliminate respiratory and cardiac motion artifacts. Secondly, the IVUS frames were analyzed and segmented semi-automatically, to detect lumen contours and the media/adventitia interface. Subsequently, the IVUS cross sectional images were positioned perpendicularly onto the reconstructed 3D catheter path and finally the coronary artery segment was generated utilizing B-splines. The final reconstruction, together with the medical images that made it possible, is shown in Figure 2.7. The stent was positioned in the stenotic area and

expanded by means of a pressure directly applied on the inner surface, as shown in Figure 2.8. Although the stenosis is relevant, no plaque is considered in this work [33].

Results in terms of morphology changes and Von Mises stresses on the arterial wall are shown in Figure 2.9. The great innovation brought by Gijsen et al. is the use of one of the most advanced reconstruction techniques, utilizing CCA and IVUS, for structural purpose. Once the medical images are taken, the intervention results can be predicted computationally.

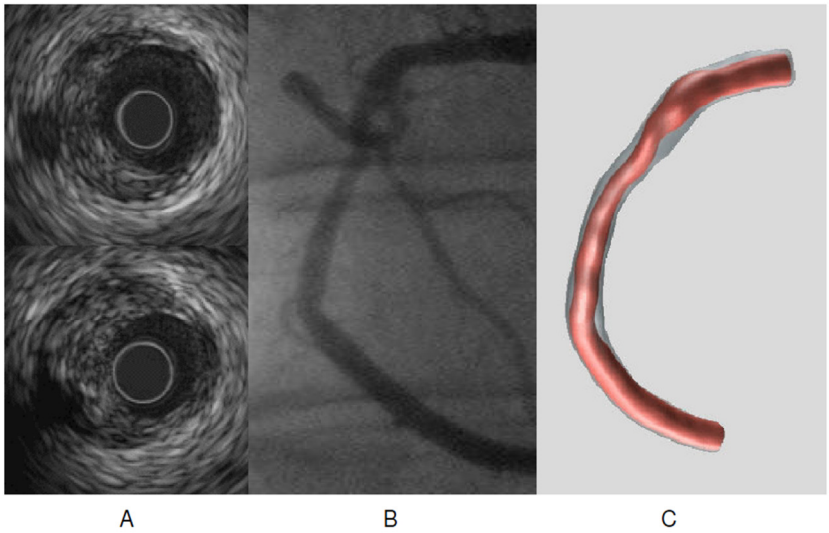

Figure 2.7 – Two IVUS images (A) and the corresponding coronary angiography (B) of the right coronary artery analyzed, with the 3D reconstruction (C) [33].

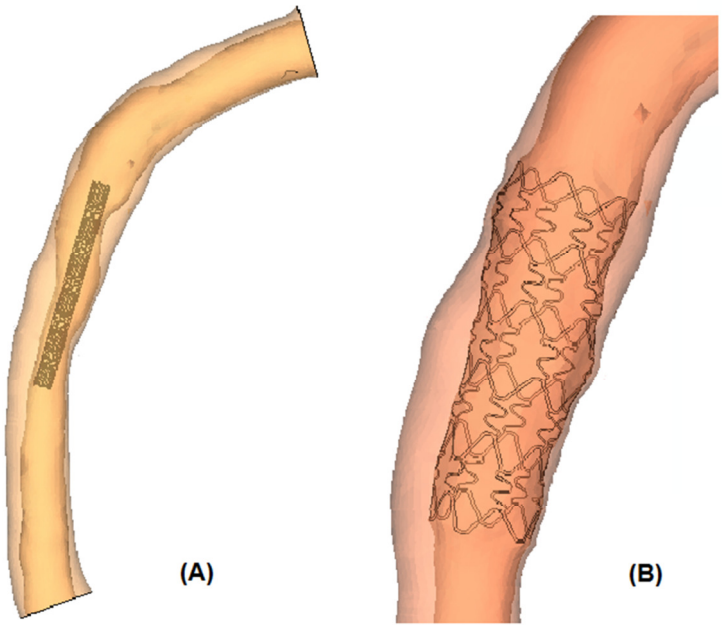

Figure 2.8 – Positioning of the coronary stent (A) and subsequent expansion in the patient-specific geometry (B) [33].

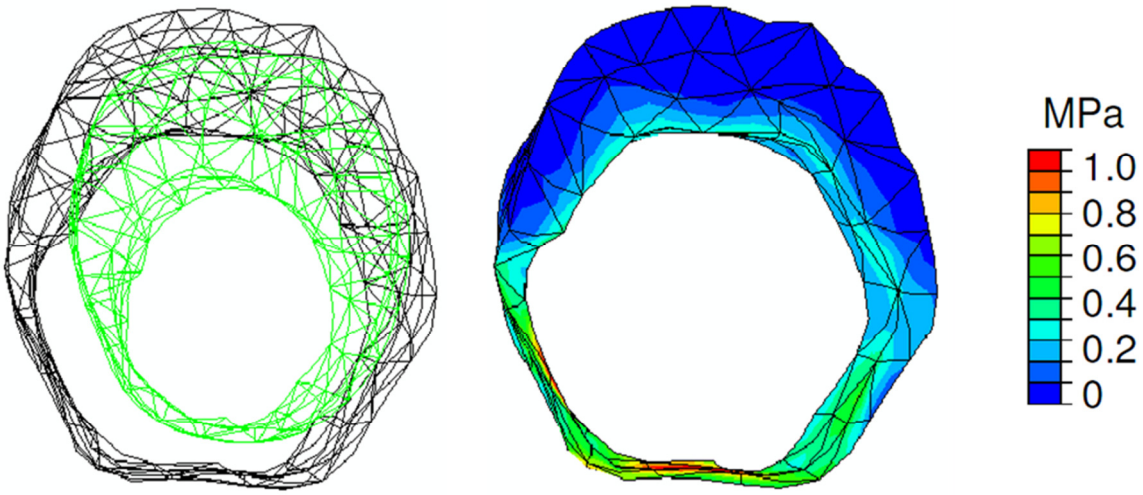

Figure 2.9 – Results of the computational work carried out by Gijsen et al. On the left, lumen shape in the most stenotic cross section before (green) and after (black) the stenting procedure. On the right, the corresponding Von Mises stresses on the arterial wall [33].

Recently, other finite element analyses concerning stent deployment in realistic arterial geometries can be found in literature. Zahedmanesh et al. (2010) simulated the expansion of a balloon expandable stent in a realistic coronary artery. The patient-derived model of an atherosclerotic linear artery segment was recreated based on digitized 3D angiographic images and reconstructing the arterial wall based on common arterial wall thicknesses. The

vessel wall was divided into three layers: *intima*, *media* and *adventitia*. The computational assembly is shown in Figure 2.10.

Mechanical analyses were performed by the commercial finite element software package ABAQUS (Dassault Systèmes Simulia Corp., Providence, RI, USA). The advanced methodology proposed a realistic trifolded balloon model coupled with the patient-derived atherosclerotic vascular segment [34]. Results in terms of Von Mises stress distribution following full expansion and after recoil are shown in Figure 2.11.

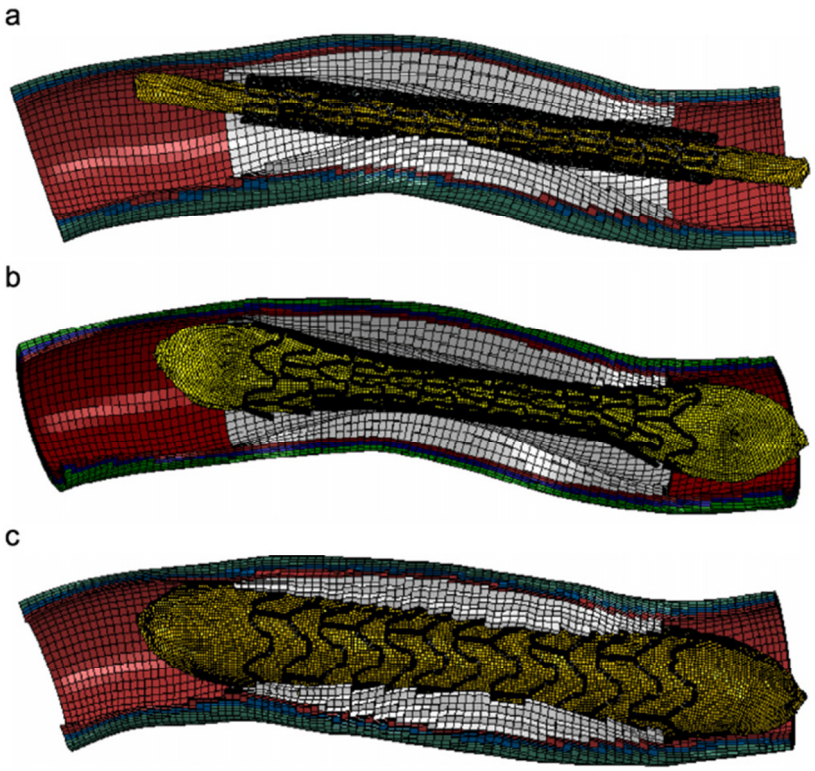

Figure 2.10–Assembly of patient-specific stenotic coronary artery, balloon and stent in crimped configuration (a), at beginning of pressurization (b) and following full expansion (c). In the vessel wall, the three layers and the plaque are colored differently [34].

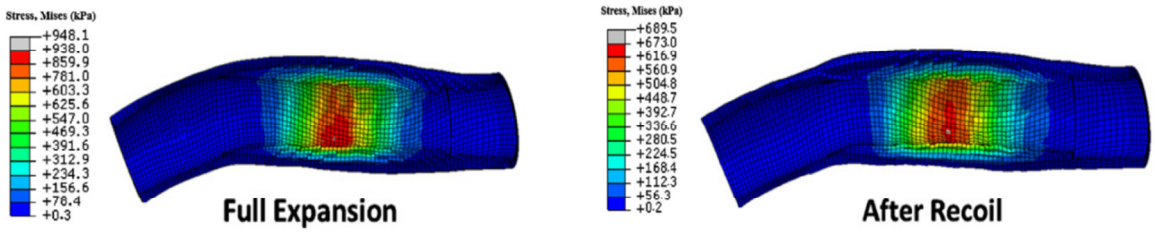

Figure 2.11 – Von Mises stress distributions following balloon full expansion (left) and after elastic recoil (right) [34].

2.1.3 Stenting procedure simulations in complex arterial geometries

The works analyzed in Paragraph 2.1.2 are image-based finite element numerical simulations involving rather simple arterial morphologies. Recently, stenting procedures in complex arterial geometries such as aneurysms and bifurcations are becoming more interesting due to higher procedural difficulties and post-interventional risks, mainly due to hemodynamic disturbances [35, 36]. As a result, realistic aneurysm morphologies or tortuous bifurcated arterial segments have been currently under investigation by means of image-based numerical models.

Molony et al. (2010) utilized CT scan data to create 3D models of patient-specific aneurysms replicating stent graft implantations. First the CT images were analyzed to identify the region of interest and to segment the different tissue boundaries and secondly the surfaces were reconstructed and smoothed. Figure 2.12 shows some of the patient geometries reconstructed.

The subsequent numerical work took into account the aneurysmatic wall, intraluminal thrombus and the stent-graft. Computational analyses were performed by the commercial software ABAQUS [37]. An example result of a commercially available stent graft finite element model following full expansion is shown in Figure 2.13. The investigation was able to assess the geometrical changes consequent to the graft stent model implantation, elaborating a sophisticated tool which could be used by physicians to predict patient-specific results of graft stenting procedures.

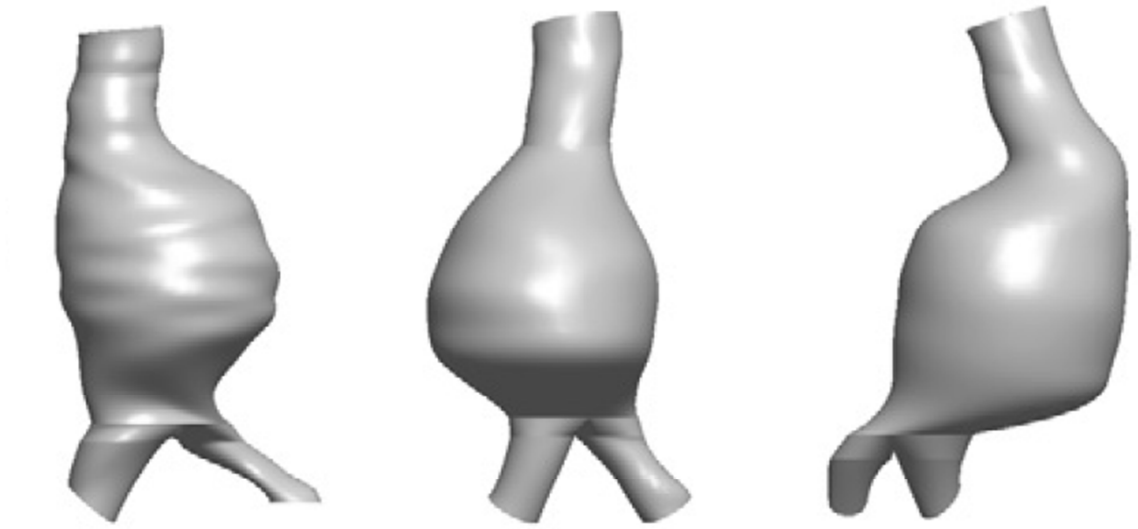

Figure 2.12- 3D reconstruction of CT image-based patient-specific aneurysm geometries [37].

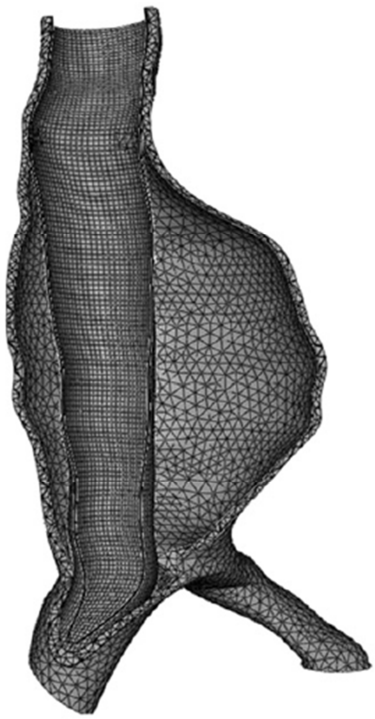

Figure 2.13 – Example result of a stent graft implantation simulated. Arterial finite element mesh is tetrahedral, stent graft discretization is hexahedral [37].

Stent graft implantation has also been simulated in pulmonary bifurcations, for the treatment of pulmonary valve dysfunction. Capelli et al. (2010) reconstructed the three-dimensional volumes of patients' implantation sites from pre-operative magnetic resonance images of the right ventricle, right ventricle outflow tract and pulmonary arteries. The valved stent graft models were created using CAD (Computer-Aided Design) software, and stent wires materials were characterized by the shape memory properties of Nitinol. The device first was crimped under displacement control, and secondly was positioned in the patient's outflow tract model, close to the bifurcation, according to the judgment of interventional cardiologists.

The numerical analyses, performed by the FE commercial code ABAQUS, proved the stent graft tendency to recover its original shape, as shown in Figure 2.14. The patient-specific simulations showed the feasibility of new devices in clinical cases, and most importantly demonstrated the ability of patient-specific data to guide device design [38].

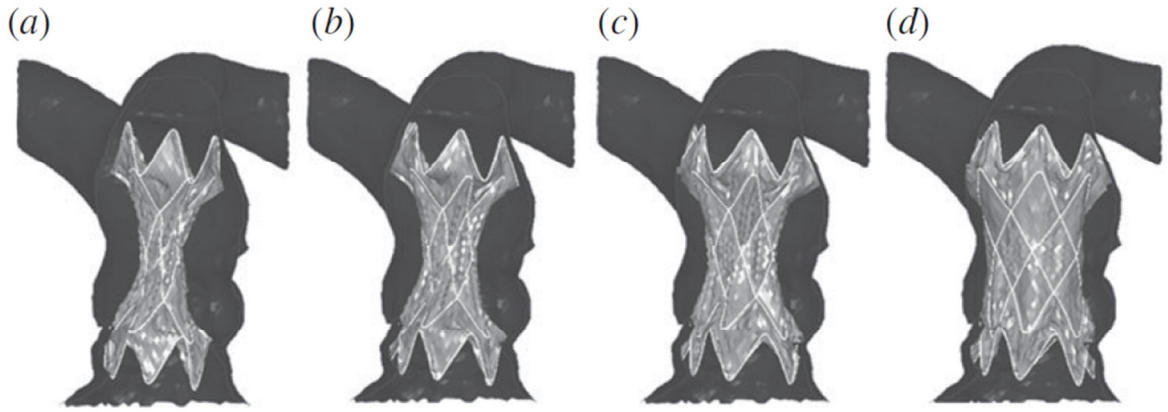

Figure 2.14 – Development of stent graft expansion: crimped configuration (a), beginning of shape recovery (b), contact with the arterial wall model (c) and final configuration (d) [38].

Auricchio et al. (2010) simulated a carotid artery stenting procedure on a bifurcated arterial model based on computed tomography angiography images. The CT images of a stenotic carotid bifurcation were processed in order to select the region of interest and remove secondary branches. Since the medical images did not contain information on the vessel wall thickness, the 3D model was reconstructed considering the thickness as a percentage (i.e. 30%) of the vessel radius. By means of B-splines, the whole geometry was generated and discretized in a high quality hexahedral mesh able to undergo numerical simulations. No plaque components were considered. The whole reconstruction procedure is shown in Figure 2.15.

To fit in such a complex geometry, the stent was first crimped and subsequently bent. The stent deployment was then simulated in an idealized way, by imposing radial displacement to an internal catheter, as shown in Figure 2.16 [39]. The structural analysis was executed using the commercial software package ABAQUS.

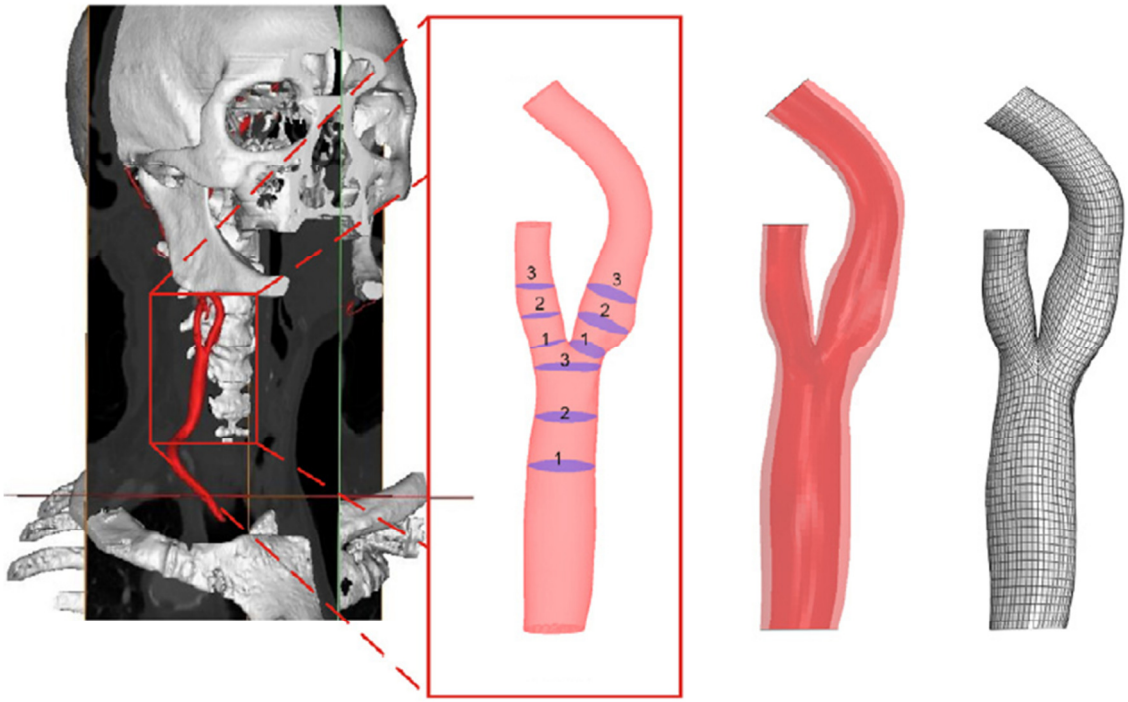

Figure 2.15–3D reconstruction of the carotid bifurcation from the CT images, to the lumen identification in the different branches, to the reconstructed vessel geometry and the hexahedral mesh generation [39].

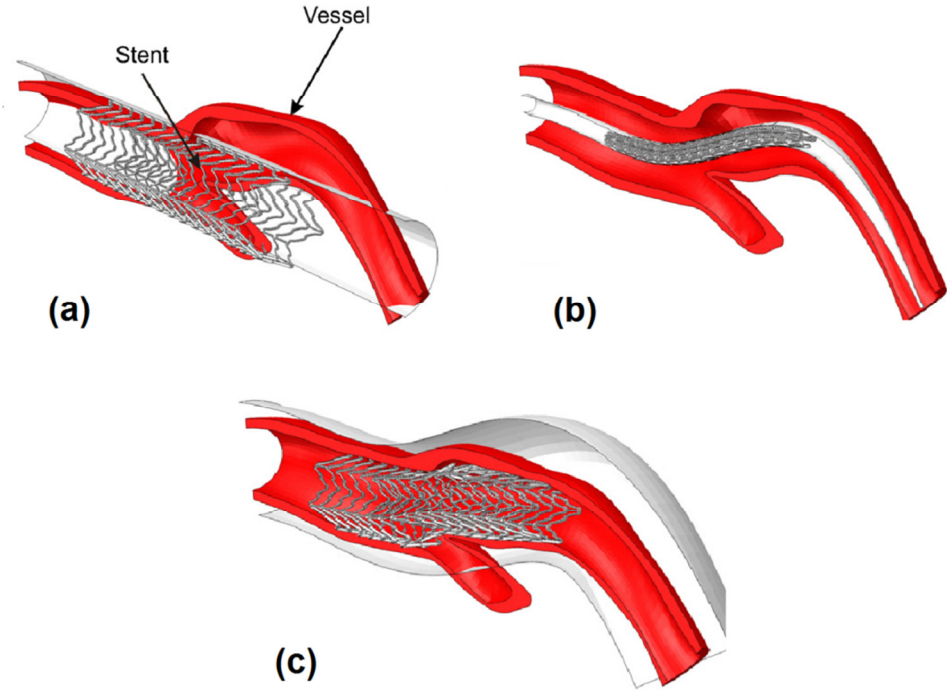

Figure 2.16–Stent deployment in the patient-specific bifurcation. Original configuration in (a), crimping and bending in (b) and expansion in (c) [39].

Another recent work involving arterial bifurcations was carried out by Mortier et al. (2009), where the expansion of three commercially available stents was compared utilizing a 3D model based on a patient-specific angiographic data. Geometrical information was obtained by rotational coronary angiography. The *in vivo*-based data consisted of a stack of circular representations of vessel cross-sections, defined by their center, radius and inclination. The NURBS surfaces of lumen boundaries were then created based on a point cloud that described the luminal cross section. To generate the outer wall, a circular approximation was obtained by scaling selected luminal circles, using a scaling factor of 1.6, based on anatomical data for healthy coronary arteries. The second NURBS surface allowed the creation of a structured hexahedral mesh of the vessel wall. The mesh was then split into three layers of equal thickness, corresponding to the three vessel layers, without considering plaque. The three-dimensional model generated, imported into the commercial software ABAQUS for structural analysis, is shown in Figure 2.17.

The intravascular stents were expanded applying an increasing pressure to a trifolded balloon. The stent models were positioned in the highly curved main branch by means of a guide wire [40]. The simulated stent insertion and deployment are shown in their different steps in Figure 2.18. The effect of new generation drug eluting stents was investigated, focusing on arterial wall stress distributions and morphology changes following the modeled intervention procedure.

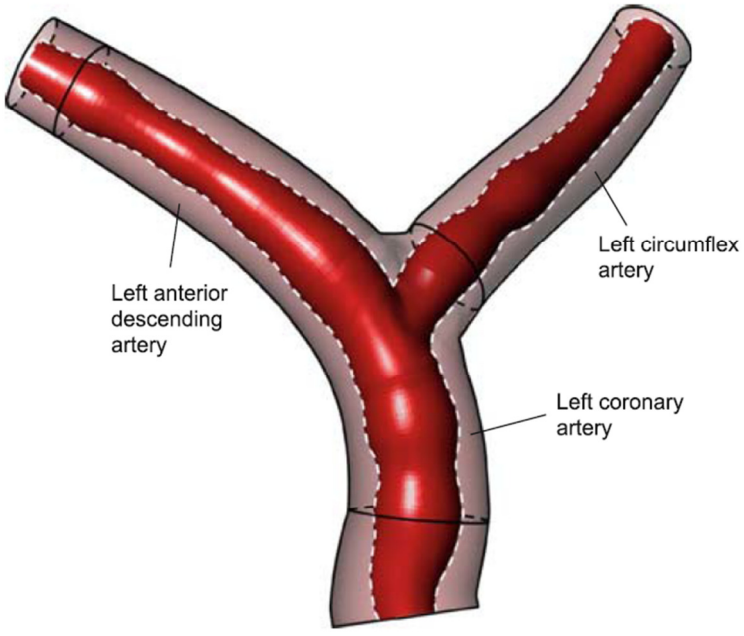

Figure 2.17 – 3D reconstruction of the coronary bifurcation obtained by rotational angiography. The circular cross sections used for the outer wall creation are shown [40].

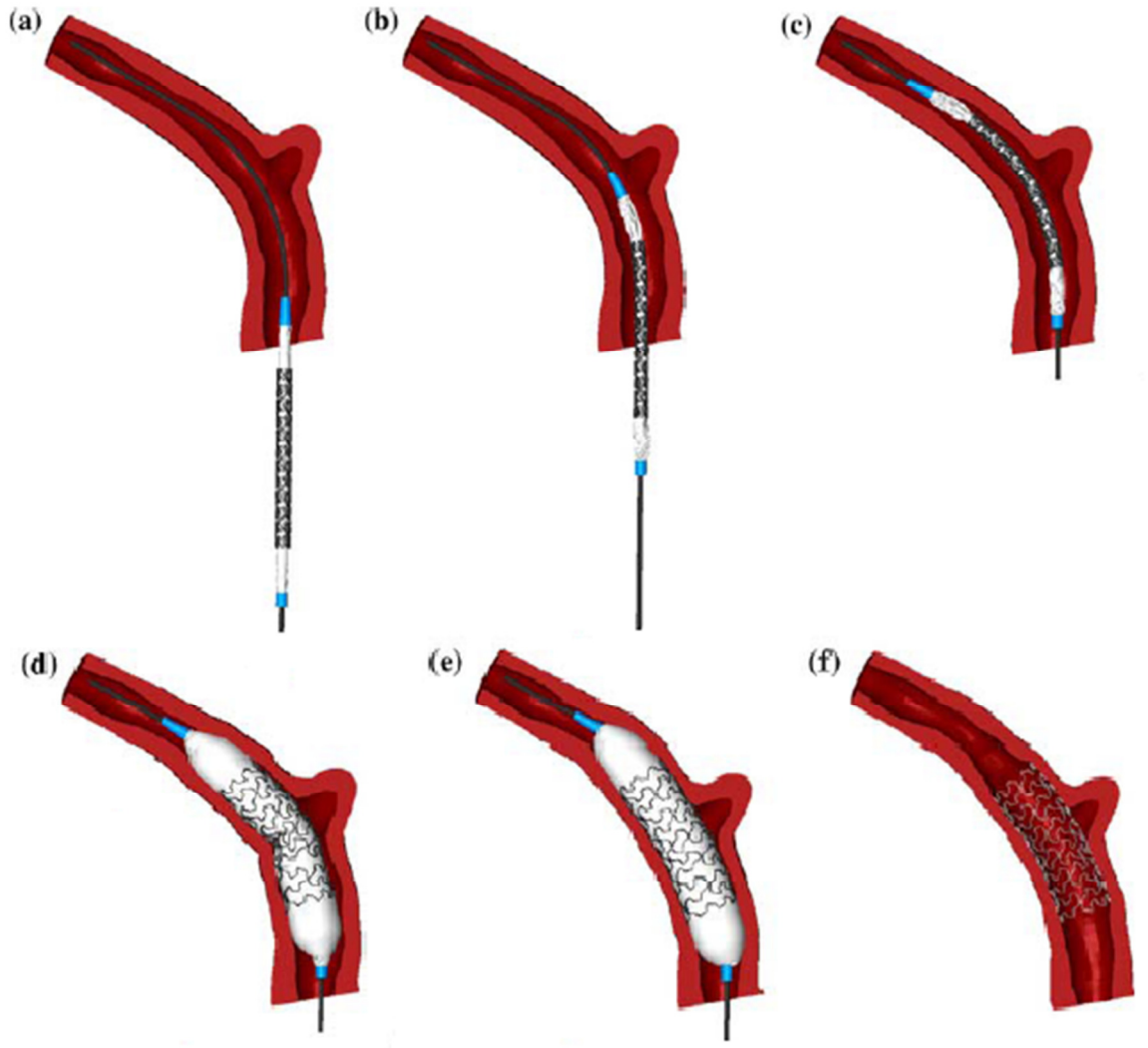

Figure 2.18–Simulation of the stenting procedure: initial configuration (a), intermediate position during insertion (b), complete insertion (c), partially inflated balloon (d), fully inflated balloon (e) and final state after balloon deflation and removal (f) [40].

To the author's knowledge, the study carried out by Mortier et al. is the most realistic numerical structural work involving coronary stenting in complex patient-specific arterial geometries. However, all the presented studies have many limitations which will be described in Paragraph 2.3.

2.2 State-of-the-art of image-based finite element models of medical devices

Following the direction of numerical analyses based on imaging techniques, 3D reconstructions of medical devices have also been used to obtain results continuously closer to the real *in vivo* procedures. In order to simulate a coronary stenting implantation, attempts have been made to model both the balloon and the stent based on computed tomography imaging.

De Beule et al. (2008) proposed a trifolded balloon model developed starting from micro-CT images of the balloon-catheter assembly, as stated in Paragraph 2.2.3. The balloon was utilized to perform computational simulations of balloon expandable stenting in coronary vasculature. The finite element assembly is shown in Figure 2.19. The numerical simulations were performed by the commercial code ABAQUS.

Works carried out demonstrated the benefits of using the trifolded balloon methodology, showing good qualitative and quantitative agreement with both the manufacturers' data and experimental tests [25]. The image-based model was also proposed for a further investigation carried out by Mortier et al. (2008) investigating the changes in stent deployment varying geometrical parameters, such as balloon length and positioning, showing the enormous influence they have on the transient stent expansion behavior [24].

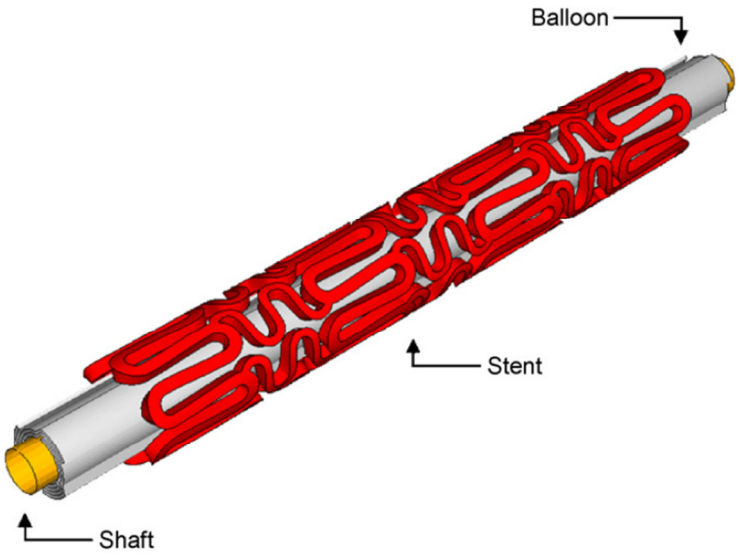

Figure 2.19 – Finite element configuration of inner shaft, trifolded balloon and stent models [25].

The use of image-based stent models is more challenging, due to their structural complexity. Badalucco et al. (2010) generated a micro-CT based geometrical model of a coronary stent, performing computational simulations in order to compare the results to those obtained with a CAD model. However, the results were discouraging, in that the CT images presented artifacts in terms of geometrical asymmetries and irregularities. Stress and strain distributions were not corresponding, as shown in Figure 2.20. The main cause of the conflicting results achieved is the different starting configuration, in which the CT-based model highlights asymmetries [41]. The geometrical differences can be viewed in Figure 2.21.

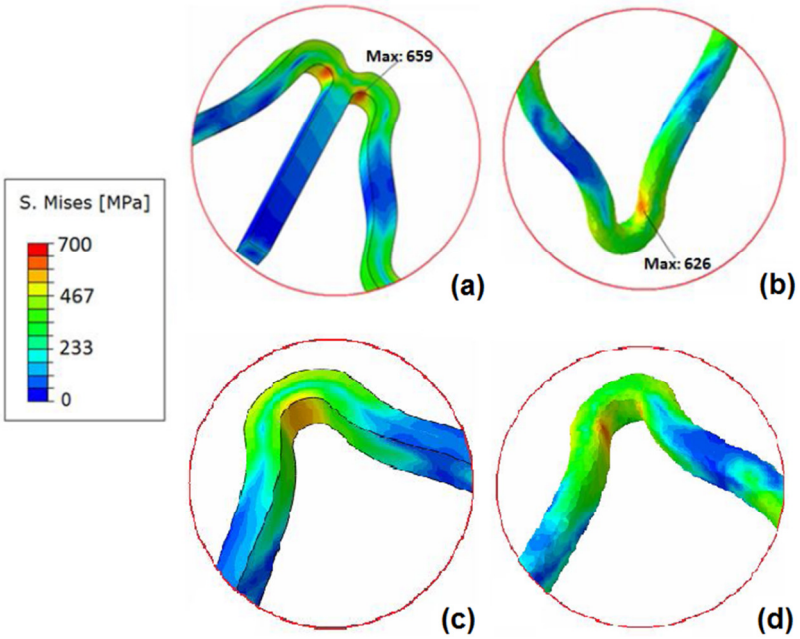

Figure 2.20 – Von Mises stress distributions in a stent strut. At the top, maximum stress for CAD (a) and CT-based (b) models. At the bottom, difference in stress distribution in the same strut for CAD (c) and CT-based (d) models [41].

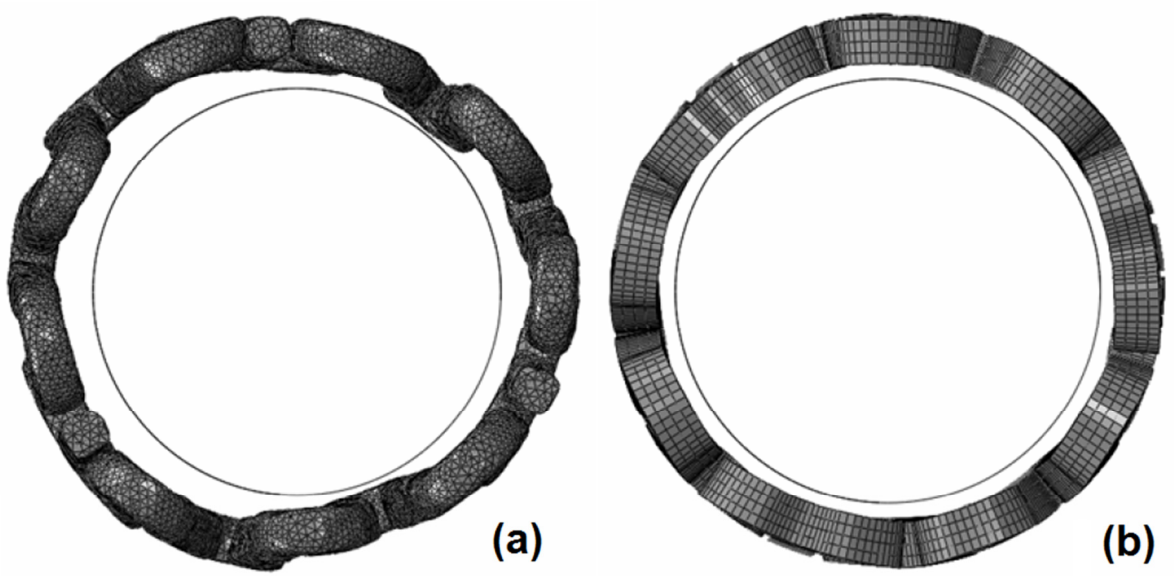

Figure 2.21 – Comparison between the two different initial configurations: micro CT-based model (a) and CAD model (b) [41].

2.3 Final considerations

The presented numerical studies are some of the most advanced structural works involving image-based finite element simulations of intravascular treatments. The methodologies described can accurately predict patient-specific clinical procedures, helping physicians in the decision-making process, by enabling virtual implantation prior to the actual procedure. Nevertheless, many limitations to an optimal realistic technique can be found.

As far as the image-based geometry modeling is concerned, the most advanced 3D reconstruction techniques take into account two medical image types providing different information, so that the advantages of each one can overcome the drawbacks of the other (see Paragraph 1.2). Among the presented studies, only Gijsen et al. (2008) base their geometry generation on more than one image type, i.e. CCA and IVUS images. The other analyzed works have to base their reconstructions on common wall thicknesses values.

Furthermore, although in many of the works several tissue components are detected, the consequent finite element simulations are heavily simplified in order to reduce computational cost. To the author's knowledge, no work involving stenting simulation in complex geometries considers atherosclerotic plaque, which strongly influences the results

acquired. Indeed, the plasticity properties exhibited by plaque tissue components are highly responsible for lumen widening after stent expansion.

Also, some of the geometries chosen for patient-specific 3D reconstruction appear to be fairly simple, reducing the purpose of image-based modeling. Gasser et al. (2007) reduce computational cost by slicing the arterial model, while the works presented in Paragraph 2.1.2 do not involve stent bending, in a configuration that does not seem close to the realistic procedure.

As far as the finite element simulations are concerned, the guidelines suggested by Martin et al. (2010) for computational modeling of stent deployment are often not followed. The numerical analysis for stent expansion should always take into account the balloon, and its presence cannot be neglected to achieve a realistic expansion [42]. However, Auricchio et al. (2010) model the stent expansion governing the radial displacement of an internal cylinder, while Holzapfel et al. (2005) and Gijsen et al. (2008) apply a direct pressure in the inner surface of the device.

Moreover, it has been reported that for the analysis of stent deployment, the stent should be free to expand and contract in the radial and longitudinal directions [27]. Nevertheless, the only image-based work among those mentioned not assigning constraints to the stent is the study carried out by Zahedmanesh et al. (2010).

The image-based medical device models, instead, have greater drawbacks. Patient-specific balloon models have never been used for numerical works, and balloon geometries based on CT images of the presented studies must be idealized in order to perform finite element simulations. When regenerating stent models, medical images have not allowed accurate analyses, in that small geometrical asymmetries heavily influenced the computational results.

The present thesis work follows the direction of the revised studies, with the attempt to compute numerical analyses able to replicate the stenting procedure more realistically. The image-based finite element method utilizes complex geometries, i.e. stenotic coronary bifurcations, to compare the anatomical differences following stenting procedure between real clinical cases and the numerical results. In the next chapter the modeling will be described.

Chapter 3

Selection of the angioplasty balloon numerical model

The third chapter clarifies the choice of the balloon model used for the finite element work. A comparison is carried out between two balloon configurations, investigating the effects of the use of a more realistic model.

Balloon-expandable stents are the most common medical device used in coronary interventions. In stenting procedure, the balloon is mounted on the catheter in a folded configuration and is used to deploy metallic stents. Commercially available angioplasty balloons present three to six folds [43, 44, 45, 46]. Increasing the number of folds, the expansion appears more uniform due to symmetry, as shown in numerical works [47].
Computational analyses of stent expansion have not usually taken into account the folded configuration of the balloon [27]. However, in order to simulate the realistic stenting procedure, and achieve increasingly accurate results, a few studies have developed folded balloon models. Works have been carried out with tri-folded and six-folded balloons [24, 25, 34, 48]. Following this direction, the presented work replicates a five-folded balloon model. In order to investigate the effect of realistic folded balloon models, a comparison of stent deployment will be presented using a five-folded and a multi-folded balloon configuration. In this way, the importance of folded balloon configuration will be explored.

3.1 Balloon models: five-folded and multi-folded

3.1.1 Geometries

In order to obtain the five-folded balloon configuration, the geometry of an unexpanded balloon was created using the commercial CAD software RHINOCEROS 4.0 Evaluation (McNeel & Associates, Indianapolis, IN, USA). The external diameter of the folded balloon was set to 0.7 mm, and the wing length chosen resulted in an expanded balloon diameter of 3 mm, an appropriate coronary stent diameter. The thickness was set to 0.03 mm. The tapered ends replicated the real clinical assembly, with the balloon ends constrained to the catheter. However, the CAD geometry still contained idealizations, such as sharp edges, and the creation procedure resulted highly time-consuming.
The method to obtain the multi-folded geometry was opposite, since the balloon was first created in the expanded configuration, with a central diameter of 3 mm. Subsequently, after a first step in which alternate nodes underwent a small radial displacement, an internal negative pressure (0.03 MPa) was applied, obtaining a deformed configuration that

fitted inside the crimped stent. Also, the final balloon elements were pulled imposing longitudinal displacement in order to lengthen the deflated balloon. The steps carried out to achieve such a configuration are shown in Figure 3.3.

3.1.2 Discretization

The balloon models were discretized using membrane elements. Such elements neglect the influence of one dimension, i.e. thickness, with respect to the other two, so forces are transmitted only on the plane setting flexional rigidity to zero. Membrane elements are commonly used to characterize thin surfaces, and appear adequate for the studied case. Discretization was achieved by means of a quad-dominated sweep technique.

The five-folded balloon domain was divided into 18525 quadrilateral membrane, reduced integration (M3D4R) elements. The mesh generated and the folded configuration used are shown in Figures 3.1 and 3.2.

The final mesh obtained for the multi-folded model consisted of 18144 quadrilateral reduced integration linear membrane elements (M3D4R). The radial view of the model before and after deflation is shown in Figure 3.4, in which the generated mesh can be appreciated.

3.1.3 Material

Basing the choice on commercially available medical devices, the material model reproduces polyethylene terephthalate (PET) mechanical properties. The density was assumed equal to 1256 kg/m^3. The material was considered linear elastic, having Young modulus of 1455 MPa and Poisson's ratio was assumed to be 0.3.

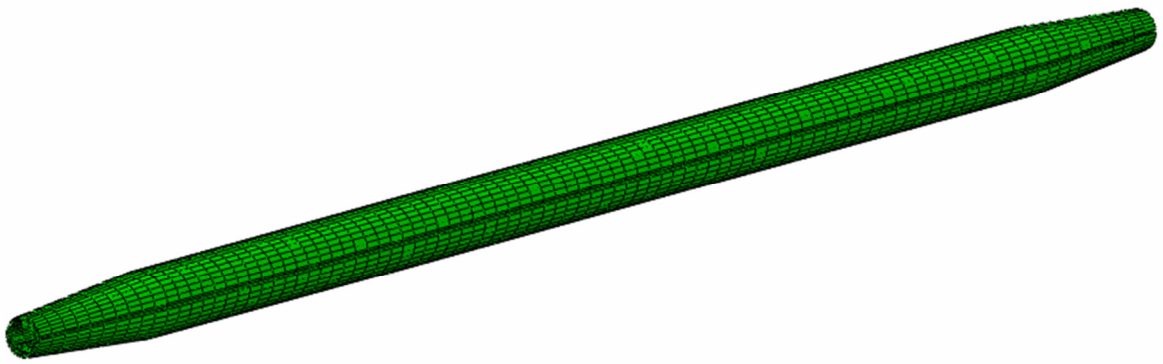

Figure 3.1 – Perspective view of the five-folded balloon model used.

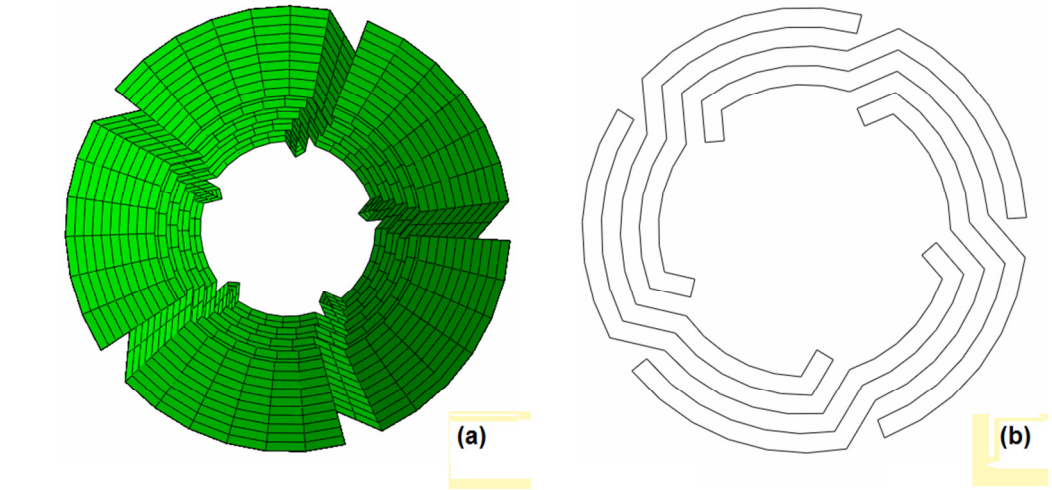

Figure 3.2 – Radial view of the balloon model, highlighting the five folds. Mesh generated (a) and central cross section (b).

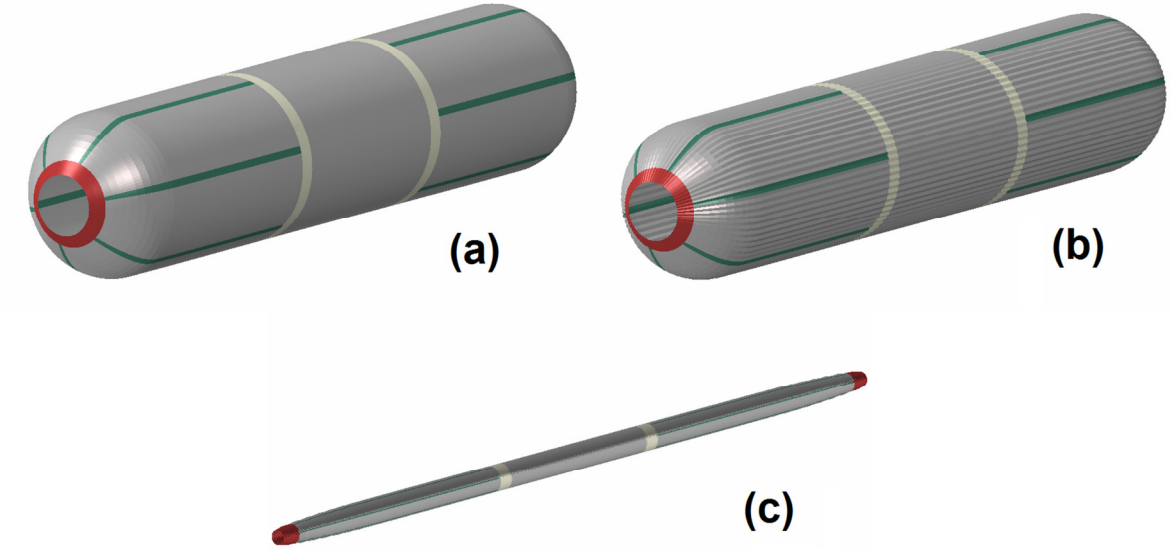

Figure 3.3 – Computational steps of balloon deflation. Initial expanded configuration (a), first step (b) and final deflated multi-folded configuration (c). Green lines represent the planes used to facilitate seeding, the red elements are the final elements, pulled in the longitudinal direction.

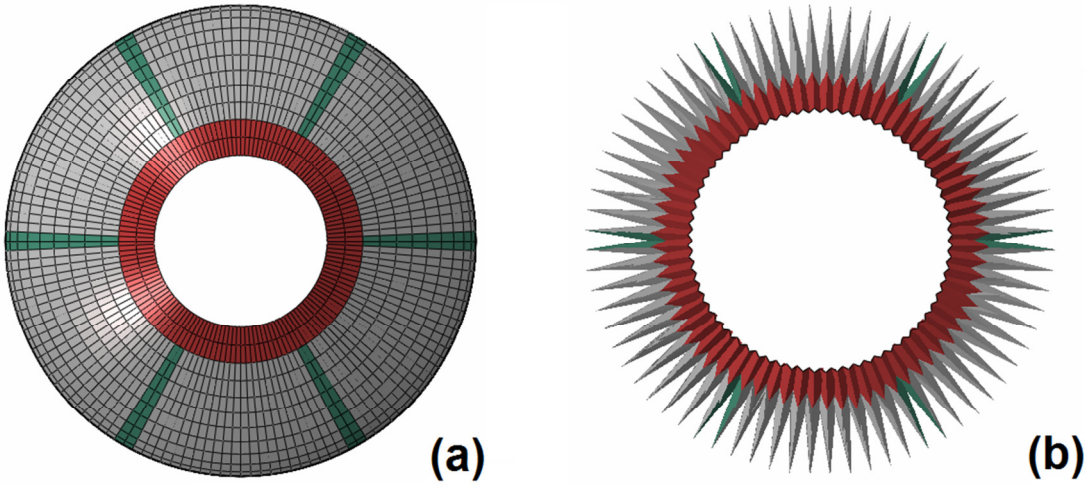

Figure 3.4 – Radial view of the balloon model; on the left discretization of the expanded configuration (a), on the right multi-folded configuration (b). The two images are not in scale.

3.2 Stent deployment simulations

In order to compare the influence of the two balloon models, stent expansion was simulated both with and without the coronary artery model, focusing on the mechanical behavior of the stent. To compare stent deployment, an examination of various geometrical parameters that were described in the work of Migliavacca et al. (2005) was carried out [49]. In order to fully assess the expansion, central radial recoil, longitudinal recoil and foreshortening were examined. The calculated quantities are thus defined:

$$Central\ Radial\ Recoil\ = \frac{R_{central}^{load} - R_{central}^{unload}}{R_{central}^{load}}$$

$$Longitudinal\ Recoil\ = \frac{L^{load} - L^{unload}}{L^{load}}$$

$$Foreshortening\ = \frac{L - L^{load}}{L}$$

where $R_{central}^{load}$, R_{distal}^{load}, L^{load} are the central radius, the distal radius and the longitudinal length, respectively, after the load application, while $R_{central}^{unload}$ is the central radius when the load is removed. L is the initial longitudinal length of the stent. Also, the mechanical behavior of the stent model was investigated, in terms of maximum Von Mises stress obtained at full expansion and after elastic recoil.

3.2.1 Coronary stent model

In order to compare stent deployment utilizing the presented balloon models, a commercially available coronary stent was modeled. The design in which the stent was created using the CAD software RHINOCEROS resembles the strut geometry of MULTI-LINK VISION coronary stent (Abbott Vascular, Abbott Park, IL, USA), an extremely widespread device. In particular, the stent model used in the numerical analyses had a nominal external diameter of 1.76 mm and a length of 13.12 mm.

The stent model was then discretized into 211468 hexahedral elements, as shown in Figure 3.5. The mesh density was chosen after accurate sensitivity analyses. The material model replicated the mechanical behavior of cobalt chromium alloys (i.e. Young's Modulus of 233 GPa and Poisson's ratio of 0.35).

To accurately simulate the actual intervention procedure, the stent was firstly crimped to an external diameter of about 1.1 mm by controlling the displacement of a cylindrical rigid surface in contact with the external diameter of the stent. Subsequently, the final configuration of the device was imported in the expansion analyses maintaining the post-crimping stress distributions.

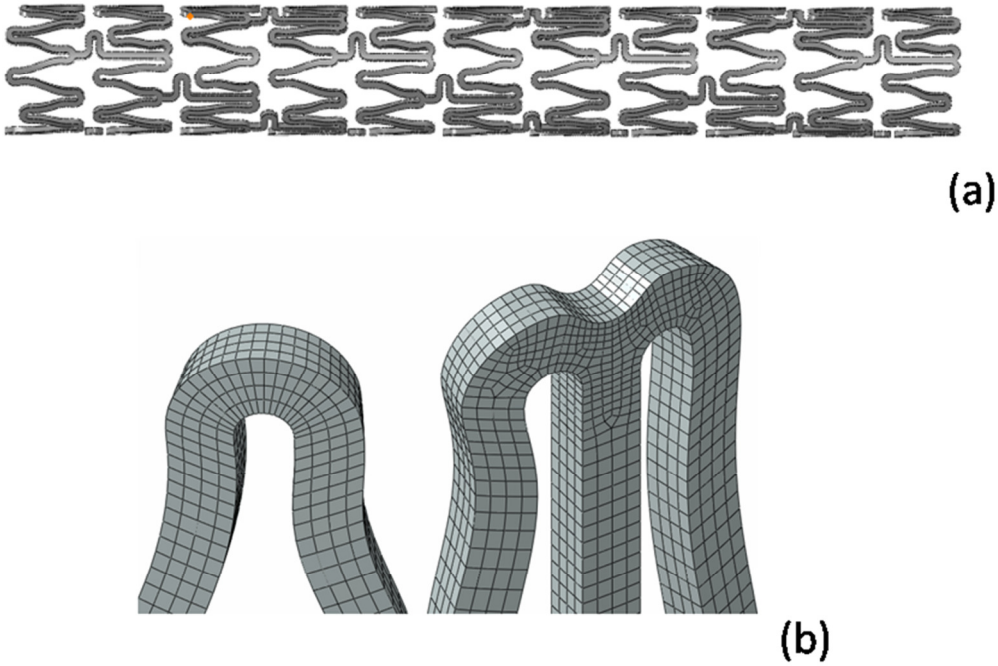

Figure 3.5 – Coronary stent model resembling the Multilink Vision stent (Abbott) (a) and close-up of the final mesh (b).

3.2.2 Free expansion

Firstly, the stent's free expansions were compared. The two balloon models described were set inside the crimped stent model, as the assemblies show in Figure 3.6. An inner guide was positioned internally and fully constrained, to simulate the catheter role. A gradually increasing pressure was applied to the inner balloon surface, up to 1.5 MPa. The balloon ends were constrained in the radial direction, in order to achieve a realistic stent expansion. All interactions were assumed frictionless and modeled with the general contact algorithm. As the analyses were carried out using the finite element software ABAQUS/Explicit, energies were monitored in all simulations, ensuring that the ratio of kinetic energy to internal energy remained under 5%, to achieve a quasi-static solution. Following this direction, an adequate viscous pressure applied to the stent surface and smooth amplitude curves helped to damp out the low frequency dynamic effects.

3.2.3 Coronary artery model

The case of stent deployment in a free expansion is a key step while proving the influence of the balloon model. However, to fully verify the effect of different balloon configurations, further computational work simulating *in-vivo* stent deployment became necessary. Thus, a linear 20 mm coronary artery segment was modeled. In order to

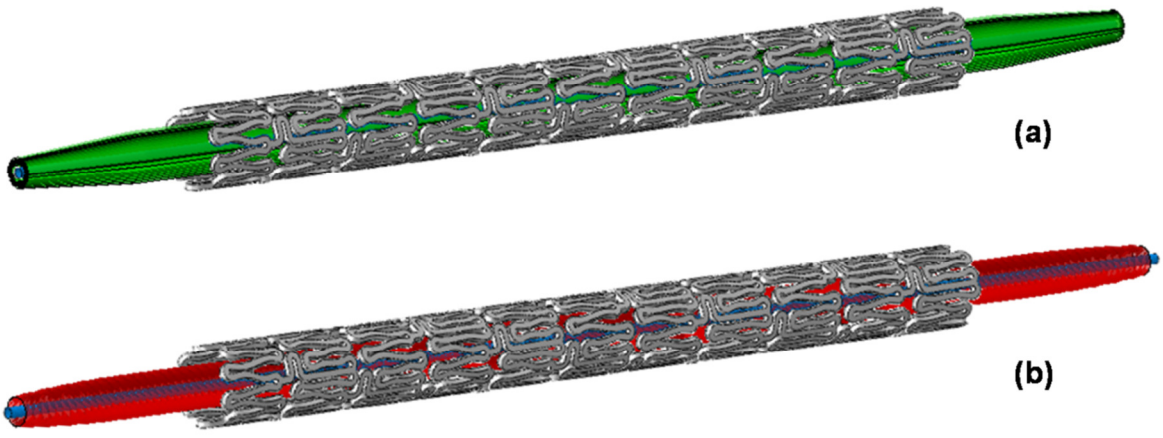

Figure 3.6 – Initial assemblies of free expansion simulations, with five-folded (a) and multi-folded (b) configurations.

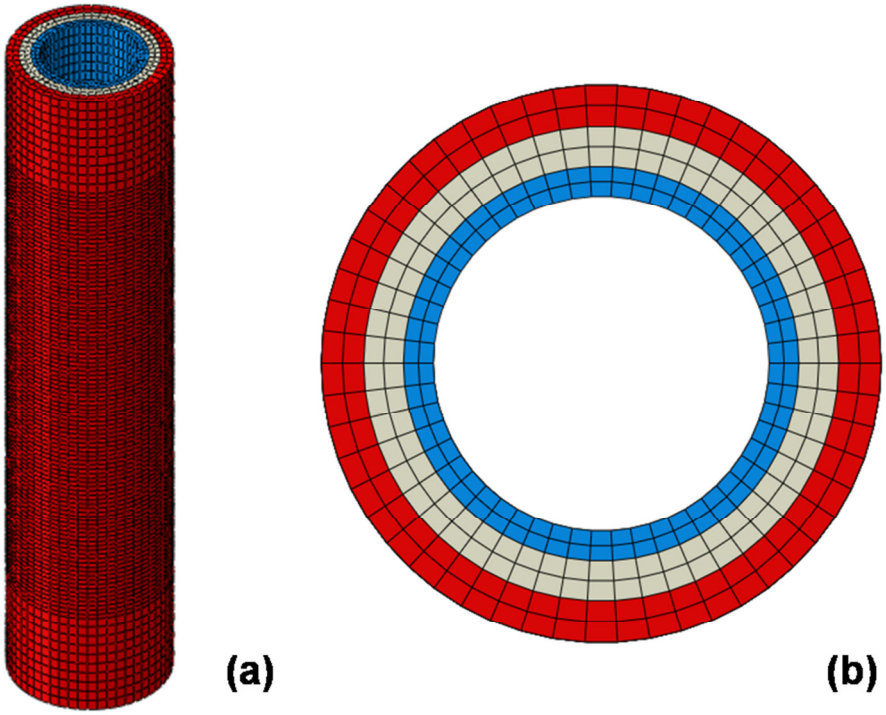

Figure 3.7 – Linear coronary segment. Full perspective view (a) and cross sectional view highlighting the three wall layers (b).

replicate correct anatomical features, the inner diameter was set to 2.7 mm and the wall thickness to 0.9 mm. The arterial segment was subsequently discretized using 38880 hexahedral elements.

Moreover, the arterial wall was divided into three layers (i.e. intima, media and adventitia) and each layer was characterized by different mechanical properties, expressed by a polynomial strain energy density function, obtained from the work carried out by Holzapfel et al. (2005) [50]. The generated mesh is shown in Figure 3.7, highlighting the three different wall layers.

3.2.4 In-vivo expansion

The assembly used for free expansion simulations was positioned inside the coronary artery model, to assess the stent and the artery response to balloon expansion. The ends of the arterial segment were constrained in radial and in circumferential directions, by means of a cylindrical coordinate system set internally to the vessel model. The boundary conditions were kept as for the free expansion analyses, and the interactions were still modeled without friction. An extra viscous pressure applied to the arterial model helped in

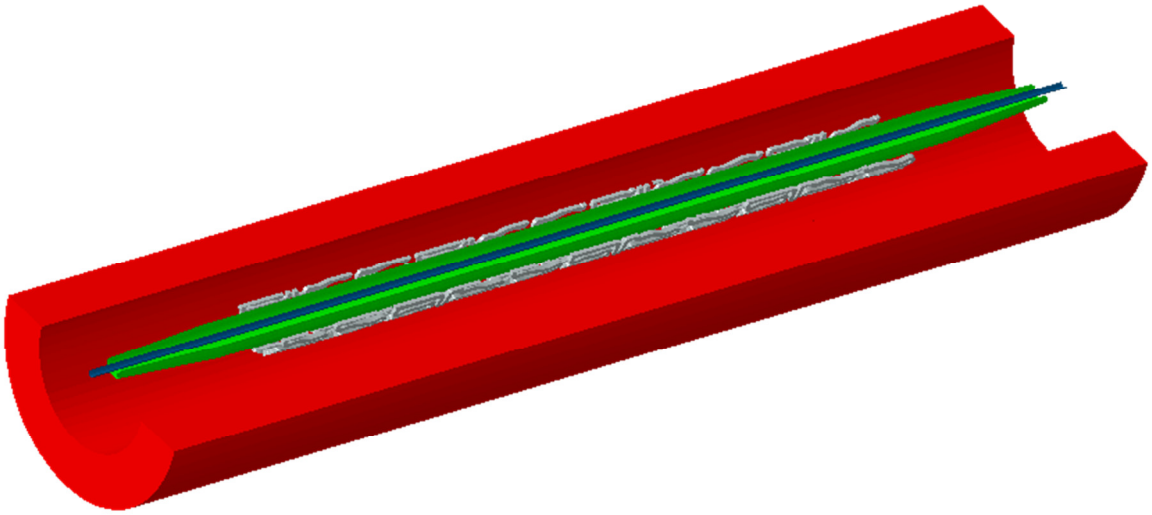

Figure 3.8 – Initial assembly used for expansion, to assess in-vivo stent deployment. The catheter (blue), balloon (green) and stent (silver) are positioned inside the linear coronary segment (red).

damping dynamic oscillations and keeping a negligible kinetic energy. The finite element configuration for *in-vivo* stent expansion, prior to balloon inflation, is shown in Figure 3.8.

3.3 Results

3.3.1 Free expansion

The gradual inflation of the two balloon configurations is shown in Figure 3.9, which highlights the different balloon expansion. The unwrapping of the wings makes the five-folded configuration more complicated to fully expand resulting in higher computational requests. The inflation dynamics are remarkably distinguishable. The cross sectional views prove that while the five folds are evident until the end, the multi-folded configuration soon takes an almost circular form. As expected, the less uniform expansion induced by the five-folded balloon inflation generated higher stress during expansion, even though the final Von Mises stresses after recoil in the two simulations are comparable. Nevertheless, despite the different balloon expansions, the stent deployment resulted strongly similar, in terms of both mechanical and geometrical parameters. As shown in Figure 3.10, the two stent expansions prove to be comparable. In both images, focusing on the strut positioning and orientation, the correspondence between the two expansions is clear. For a quantitative

proof, Table 3.1 provides the comparison details, reporting the values of the parameters considered in a stent deployment assessment.

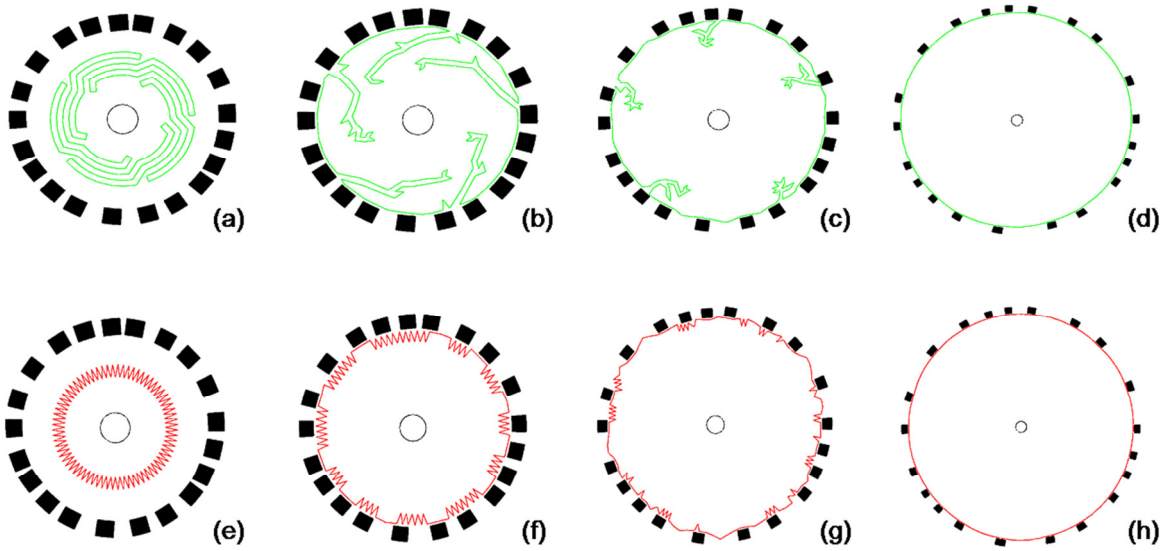

Figure 3.9 – Cross sectional cut of stent free expansion. The figures compare the behavior of the five-folded balloon (green, top row) to the multi-folded one (red, bottom row). The figures are not scaled, since interest is focused on the balloon performance.

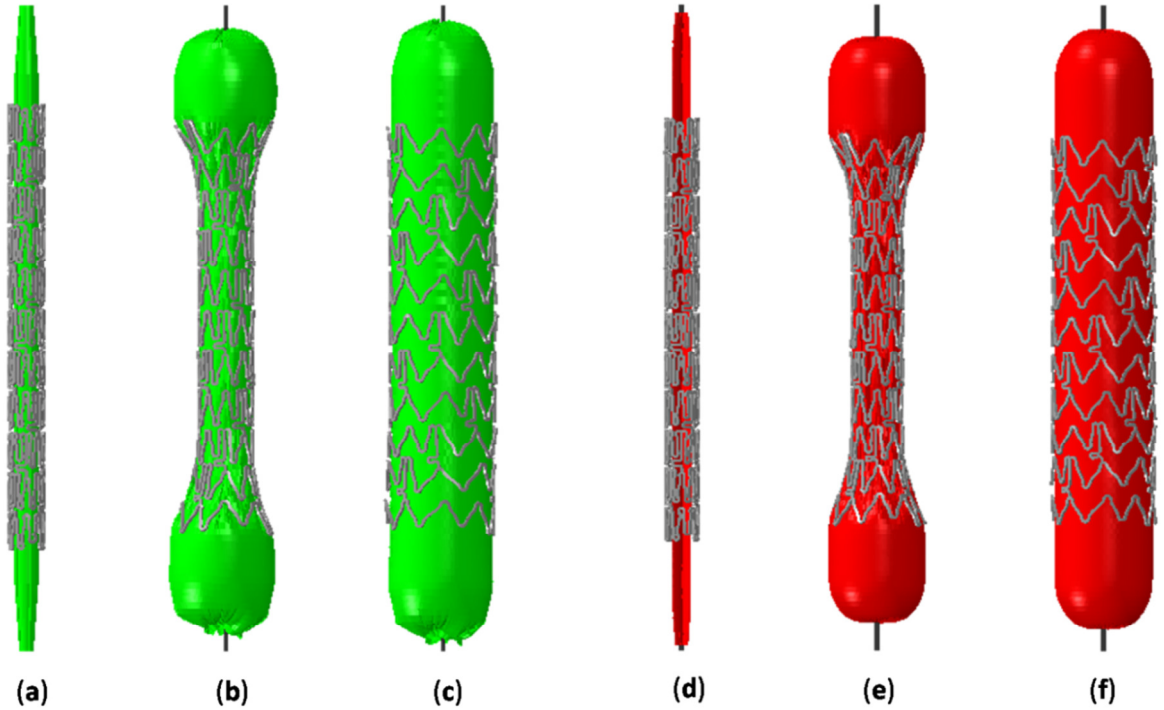

Figure 3.10 – Full view of the two free expansion simulations carried out. On the left, initial configuration (a), mid-expansion (b) and final expansion (c) of the five-folded model. On the right, initial (d), middle (e) and final (f) configurations of the multi-folded model.

Table 3.1 – Main geometrical and mechanical parameters calculated for the free expansion simulations using five-folded and multi-folded balloon models.

FREE EXPANSION COMPARISON		
	FIVE-FOLDED CONFIGURATION	**MULTI-FOLDED CONFIGURATION**
CENTRAL RADIAL RECOIL	2.362	2.297
LONGITUDINAL RECOIL	-0.350	-0.348
FORESHORTENING	8.285	8.004
MAX VON MISES STRESS AT FULL EXPANSION [MPa]	841	802
MAX VON MISES STRESS AFTER RECOIL [MPa]	556	551

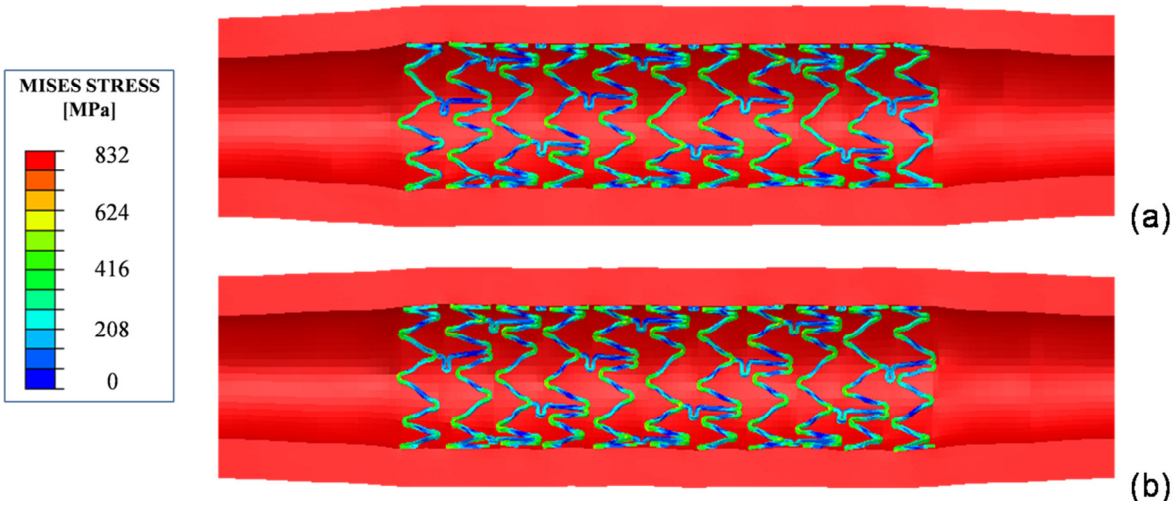

Figure 3.11 – Von Mises stress distributions for the five-folded (a) and the multi-folded (b) in-vivo expansions.

3.3.2 In-vivo expansion

The simulated *in-vivo* expansions confirmed the similarity achieved from the free expansion tests, proving a very low disparity between the two balloon models. Figure 3.11 shows the Von Mises stresses obtained on the coronary stent model during expansion. Again, the five-folded configuration causes higher stresses due to the expansion dynamics. The fewer number of folds causes asymmetric expansion of some struts, increasing the maximum stresses obtained. However, the geometrical configurations after the two stent deployments are very similar, as confirmed by the numerical results given in Table 3.2.

Table 3.2 – Main geometrical and mechanical parameters calculated for the in-vivo expansion simulations using five-folded and multi-folded balloon models.

IN-VIVO EXPANSION COMPARISON		
	FIVE-FOLDED CONFIGURATION	**MULTI-FOLDED CONFIGURATION**
CENTRAL RADIAL RECOIL	2.497	2.325
LONGITUDINAL RECOIL	-0.218	-0.284
FORESHORTENING	8.986	8.948
MAX VON MISES STRESS AT FULL EXPANSION [MPa]	831	802
MAX VON MISES STRESS AFTER RECOIL [MPa]	615	583

3.4 Final considerations

As proved by the results described in Paragraph 3.3, the computational studies reproducing both free and *in-vivo* expansions have demonstrated that stent deployment is not greatly influenced by the balloon configuration.

Balloon inflations have remarkably different dynamics, causing higher Von Mises stress on some stent struts using the five-folded model. However, an accurate numerical analysis of the main geometrical parameters describing stent behavior, listed in the previous tables, confirmed the minor differences between the two balloon configurations.

In conclusion, a more realistic folded configuration, as the five-folded model presented, does not result in an improved assessment of the mechanics of stent expansion. Moreover, the use of the five-folded model causes an increase of the time needed for the preparation of the geometrical model, its discretization and the computational power required for the simulations. In light of the results obtained, the balloon model for further numerical analyses carried out, described in the following chapters, will exploit the multi-folded configuration.

Chapter 4

Computational model of a patient-specific stenting procedure

In the fourth chapter, the structural model of the real clinical intervention is described. The steps carried out to achieve a realistic 3D reconstruction of the coronary bifurcated region are explained, as well as the methods used to create CAD geometries of the intravascular devices used in the stenting procedure. Also, the final simulation details are described, as well as the preliminary analyses (crimping and bending) performed in order to make the final analysis possible.

4.1 Image-based coronary bifurcation model

Aiming to increase the realistic traits of finite element studies of cardiovascular treatments, the presented work replicates a coronary stenting intervention performed at Hospital Doctor Peset (Valencia, Spain) by means of numerical modeling. The patient-specific image-based coronary bifurcation was obtained by the reconstruction work carried out by Cárdenes et al. (2011), who utilized a method based on CCA and CT imaging, as described in Paragraph 1.2.2 [23]. In the considered case, two coronary stents were implanted in a stenotic left anterior descending (LAD) artery, in a strongly bifurcating region which involves two diagonal branches. The geometry provided by Cárdenes et al. consisted of a triangulated surface representing the lumen of the stenotic coronary region, so also corresponding to the inner coronary wall. The LAD main branch was characterized by an inlet diameter equal to 3.5 mm, while the outlet lumen diameter was 1.9 mm. The diagonal branches had smaller lumens, with diameters of 2.1 mm and 1 mm, respectively for the first and the second branch. The main branch length was equal to about 38.17 mm, whereas the first branch was 24.99 mm and the second one was 17.47 mm.

As shown in Figure 4.1, the surface presented a remarkable narrowing in the segment between the two bifurcations, representing the stenosis. Here, the inner diameter resulted equal to about 1.2 mm.

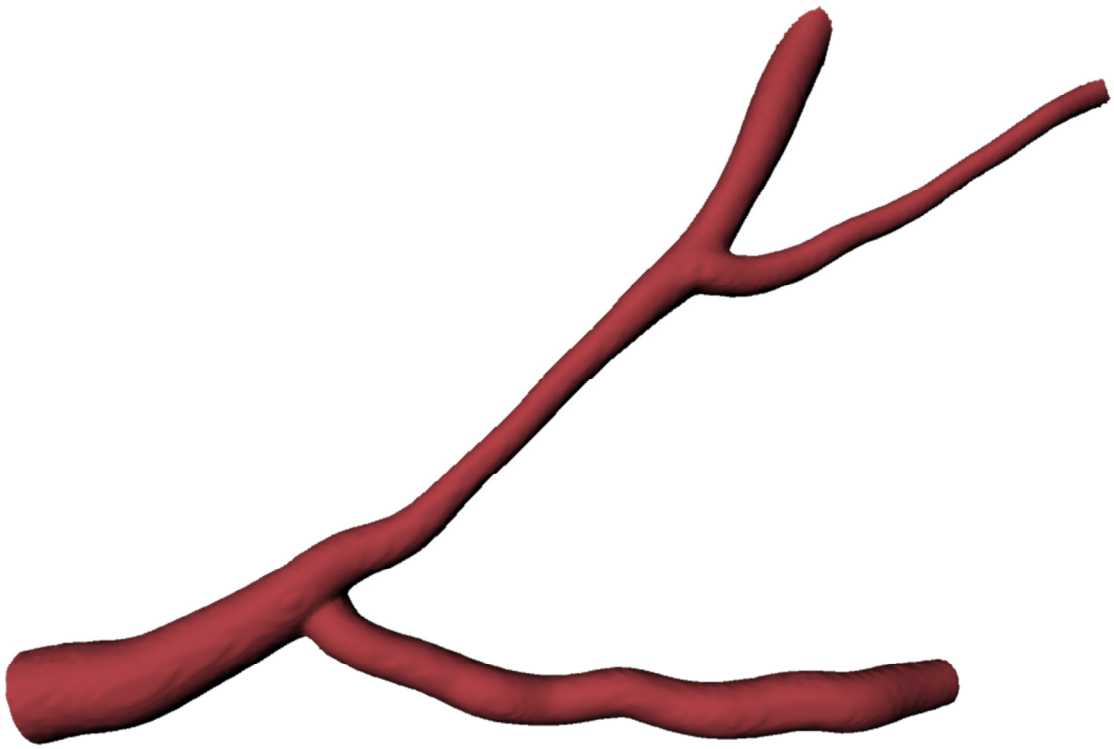

Figure 4.1 – Triangulated surface provided by Cárdenes et al., based on a patient-specific diseased coronary region [23].

4.1.1 3D reconstruction from medical images

Starting from the image-based internal surface of the artery, three steps were implemented to create a realistic representation of the 3D solid arterial wall: computation of the vessel centerline, branching of the bifurcation and creation of the external wall.

The first step carried out in order to accurately reconstruct the 3D geometry was the centerline identification. This procedure was performed using the open-source software package VMTK, a vascular modeling toolkit able to semi-automatically capture vessel centerlines [51]. The method is based on Voronoi diagrams, considering the centerline path the locus of points described by the centers of maximal spheres inscribed in the vessel. An inscribed sphere is considered maximal when no other inscribed sphere can contain it. Therefore, for every point belonging to the Voronoi diagram, there is a sphere centered in that point which is a maximal inscribed sphere. The procedure to acquire vessel centerlines can be better understood observing Figure 4.2, which shows the various steps operated by VMTK. The obtained centerlines for the presented bifurcations model were checked and

accurately fitted the arterial path, as shown in Figure 4.3. Such centerlines were calculated using the following VMTK script:

```
vmtksurfacereader -f stl –ifile FILENAME.stl --pipe vmtksurfaceviewer --pipe
vmtkcenterlines --pipe vmtkcenterlineviewer –ofile CENTERLINEFILENAME.vrml
```

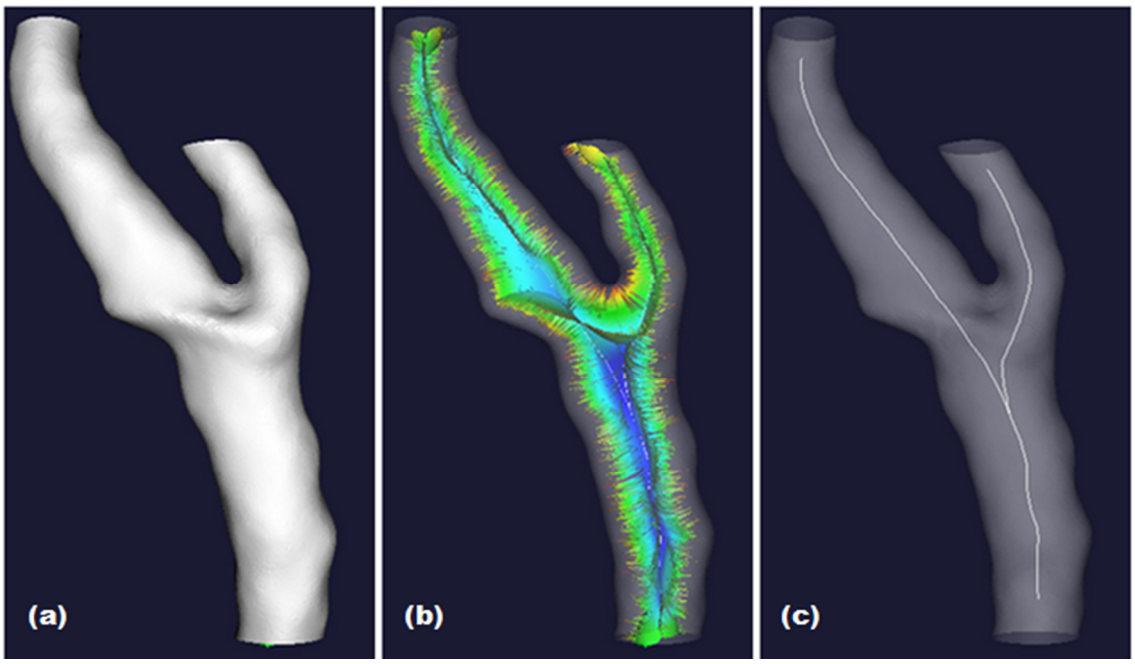

Figure 4.2 – Representation of the centerline acquisition method. Arterial surface imported (a), maximum inscribed sphere radii, from small (red for small, blue for large) (b), and final centerlines (c) [51].

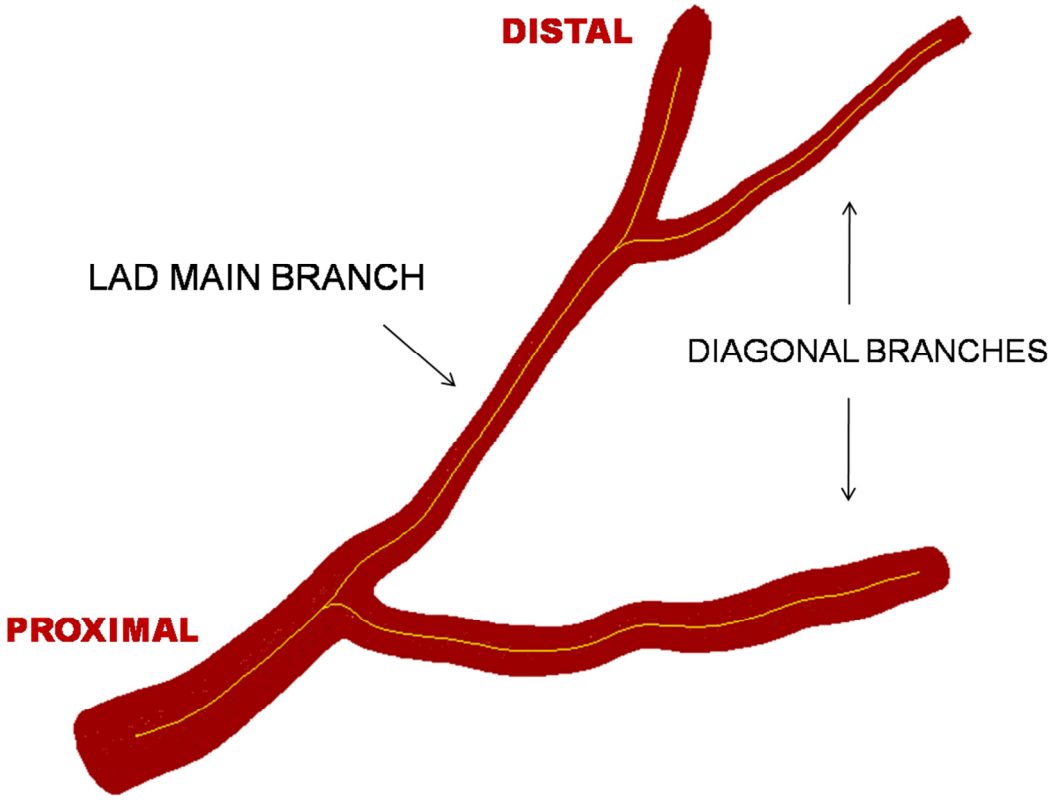

Figure 4.3 – Centerline representation (yellow) in the bifurcation lumen (red). The main branch is distinguished from the diagonal marginal branches. Also, proximal and distal regions are indicated.

The computed centerlines were then used to split the bifurcating region into separate branches. Such geometry partition will be subsequently exploited to optimize the geometry discretization and obtain a better mesh quality. In order to operate branch splitting, VMTK firstly splits the centerlines and constructs a tube around each centerline made from the envelope of maximum inscribed spheres. For each bifurcation, two points are identified: the first is located where the centerline intersects another centerline's tube; the second is set one maximum inscribed sphere upstream (see reference points in Figure 4.4). At this point, three tracts can be detected along each centerline and along each constructed tube, which is divided into groups. Once this operation is performed, the surface can be split into the branches corresponding to centerline groups. Defining a sphere a function with support in 3D and values negative inside and positive outside its surface, the same can be said for the created tubes, as they result from the envelope of inscribed spheres. Computing the value of the tube function for the various branches identified, VMTK can accurately separate the branch surfaces, as shown in Figure 4.4

For the model considered in the presented study, the inner wall surface and the respective centerlines were imported, and the subsequent segmentation was automatically operated, splitting the coronary bifurcations into the five branches, as shown in Figure 4.5. Branch splitting was achieved implementing the following script:

```
vmtksurfacereader -f stl -ifile INPUTFILE.stl --pipe vmtksurfaceviewer --pipe
vmtkcenterlines --pipe vmtkcenterlineviewer --pipe vmtkbranchextractor --pipe
vmtkbranchclipper -groupids 3 -ofile OUTPUTFILE.stl
```

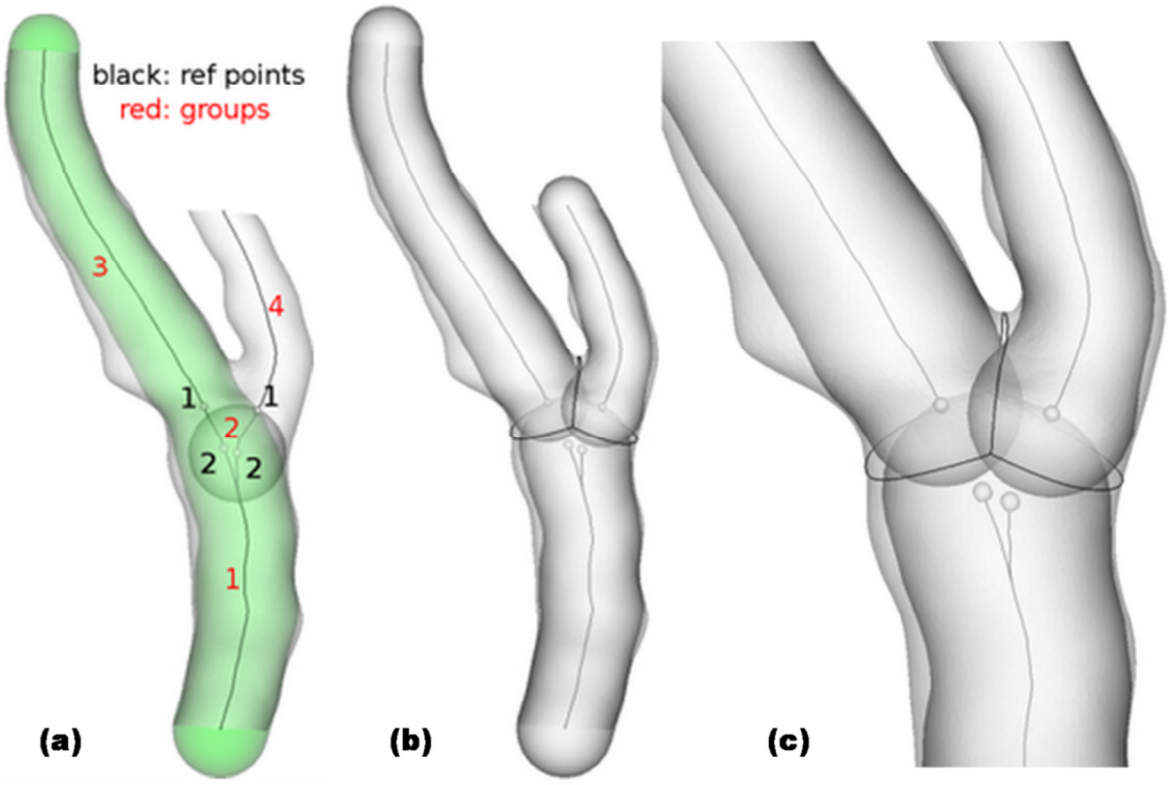

Figure 4.4 – Branch splitting operated by VMTK. First, tubes are created and reference points for each centerline are identified (a). These operations make the splitting possible (b), close-up in (c) [51].

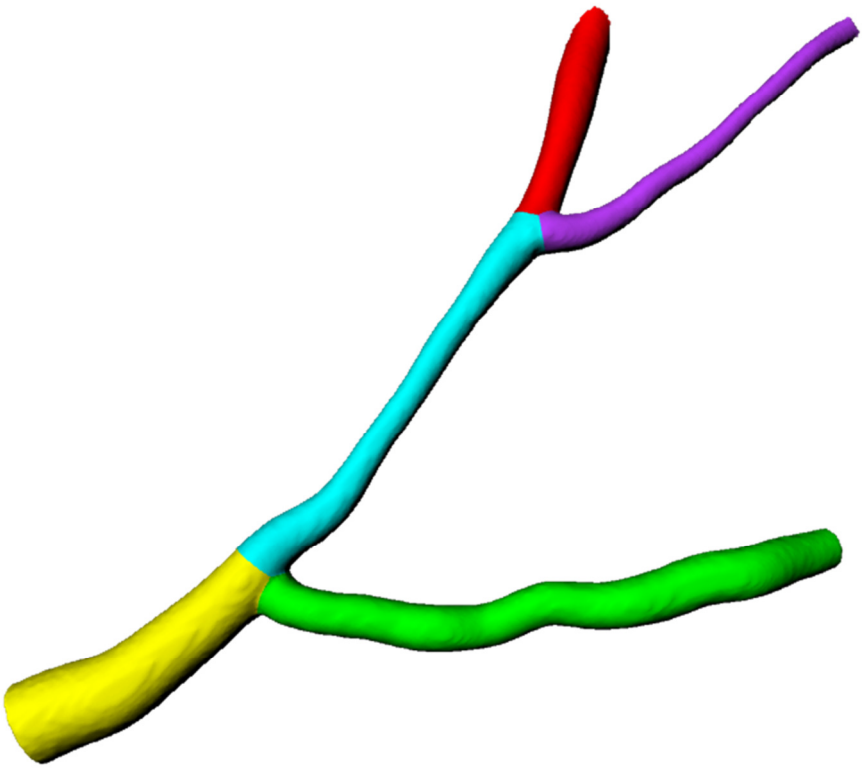

Figure 4.5 – Branch segmentation of the coronary inner wall.

Lastly, the acquired centerlines were the basis for the outer wall surface reconstruction. In order to obtain an accurate reconstruction, anatomical geometrical parameters were taken into account. Starting from the healthy regions of the model, i.e. the most proximal and distal segments of the main branch and the two diagonal branches, the non-diseased parts were set to fit physiological values of LAD wall thickness, confirmed by several medical articles [50, 52, 53]. Regarding the diagonal branches, the wall thicknesses to outer diameter ratios were kept constant. Such values well fit the coronary proportions found in literature [54]. Basing the reconstruction on physiological values of these proportions, the final main branch inlet external wall diameter resulted equal to 5.3 mm, while the outlet outer diameter was set to 3 mm. The first and second diagonal branches were created with external diameters of 3.2 and 1.6 mm, respectively.

Once the diameters were established, the surfaces were generated using the CAD software RHINOCEROS. Circumferences lying on planes perpendicularly to the centerlines were created and the single branches' external surfaces were generated by connecting them and smoothing the obtained loft surface. The separate surfaces were then connected using adequate fillet radii, obtaining the final outer wall LAD surface. As for the inner wall

surface, after the determination of the external wall centerline, the geometry was separated into five branches, to facilitate the subsequent meshing procedure. The final 3D reconstruction is shown in Figure 4.6. In order to highlight the wall thicknesses used and point out the remarkable stenosis in the arterial model, the inner and outer wall profiles are shown in Figure 4.7.

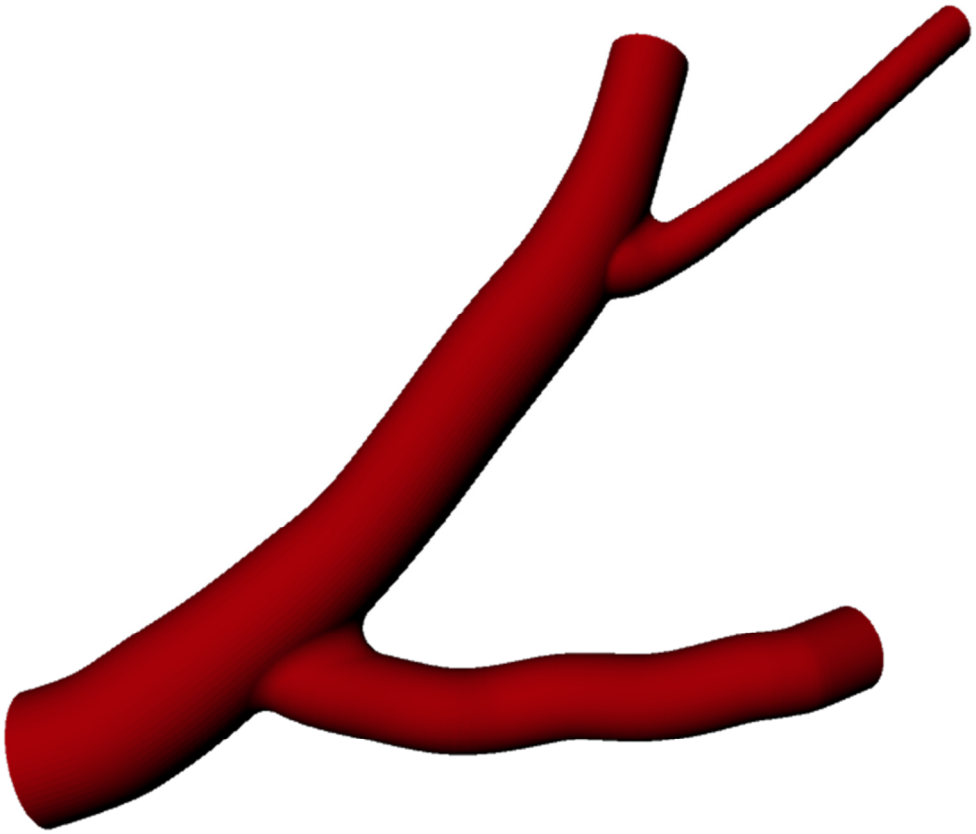

Figure 4.6 – Final LAD outer wall surface recreated.

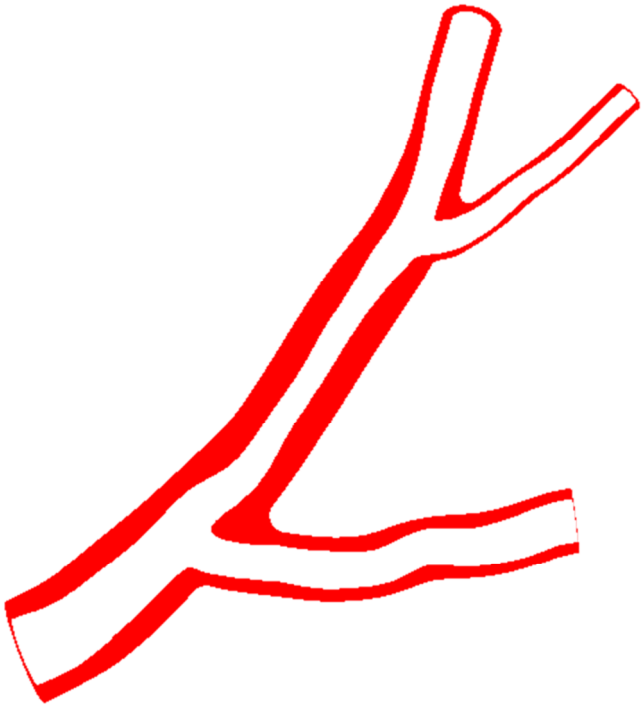

Figure 4.7 – Inner and outer coronary wall profiles. The main stenotic region is located between the two bifurcations.

4.1.2 Discretization

Once the vascular region was fully built, the domain was discretized in order to undergo the finite element analyses. Such a procedure was accomplished using the mesh generation software ANSYS ICEM CFD (ANSYS Inc., Canonsburg, PA, USA). The single branches obtained by the previous segmentation were imported, both for the inner and for the outer wall surfaces. Cutting planes perpendicular to the centerline were positioned along the coronary vessels in order to facilitate the meshing method. The hexahedral meshing procedure utilized the blocking strategy, a technique in which an adequate block topology was built to fit the vascular geometry. The blocks are hexahedrons whose edges can be associated to respective curves built along the model. For the specific coronary bifurcating model, a 3D block topology was firstly created around the whole geometry, and then further refined splitting block edges and moving block vertices. In particular, eight blocks were created along the wall circumference. The final blocking topology constructed is shown in Figure 4.8, focusing on the way blocks were built along the branches and in the bifurcated region.

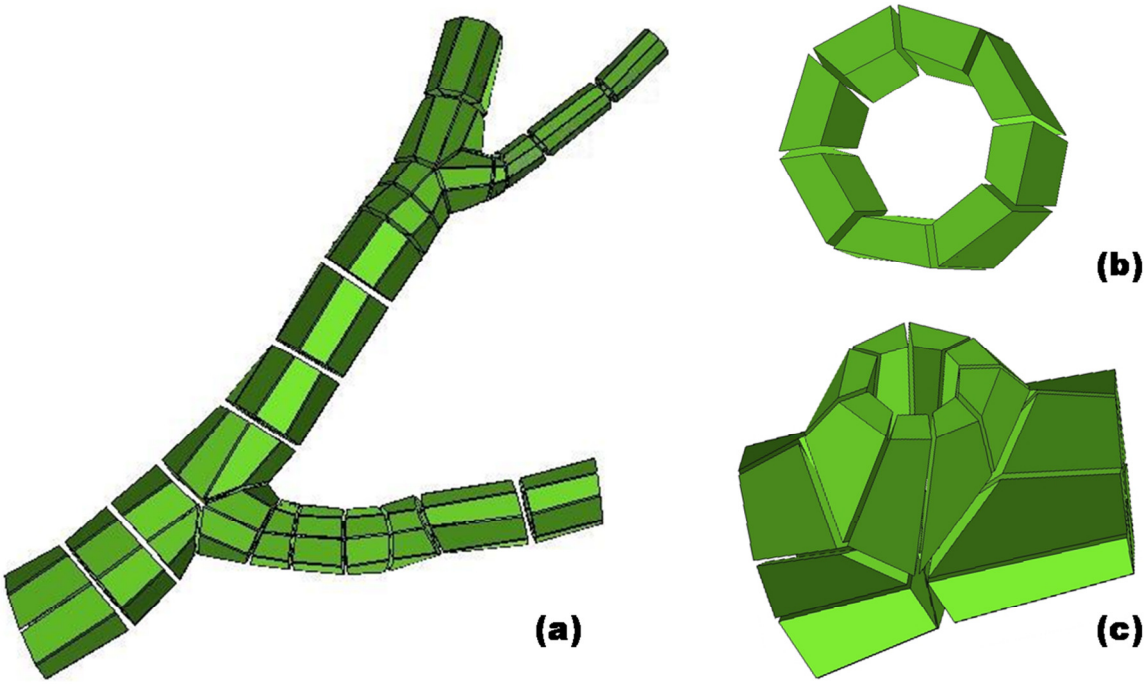

Figure 4.8 – Blocking topology used for mesh generation (a), with close-ups of the eight blocks per section (b) and of the bifurcated region (c).

The meshing software, with the appropriate blocking topology, automatically discretized the geometry, providing a projection-based mesh, where the block faces were projected to the closest model surface, following the assigned orientation. Along the coronary wall thickness six elements were generated, assigning an exponential distribution to the nodes, in order to have a higher mesh density towards the lumen, improving the accuracy of simulations without a futile increase of computational cost. After smoothing and checks of element quality, the final mesh consisted of 198334 hexahedral elements. In order to highlight the meshing of the bifurcation regions and the wall thickness discretization, close-ups can be appreciated in Figures 4.9 and 4.10.

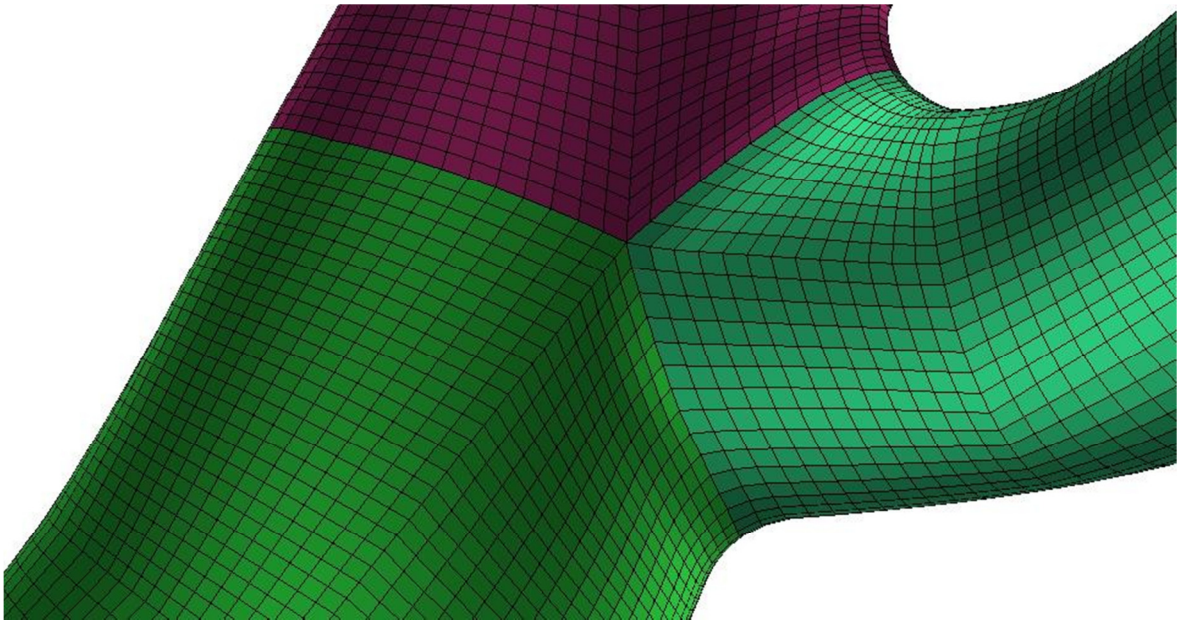

Figure 4.9 – Mesh close-up in the bifurcating region.

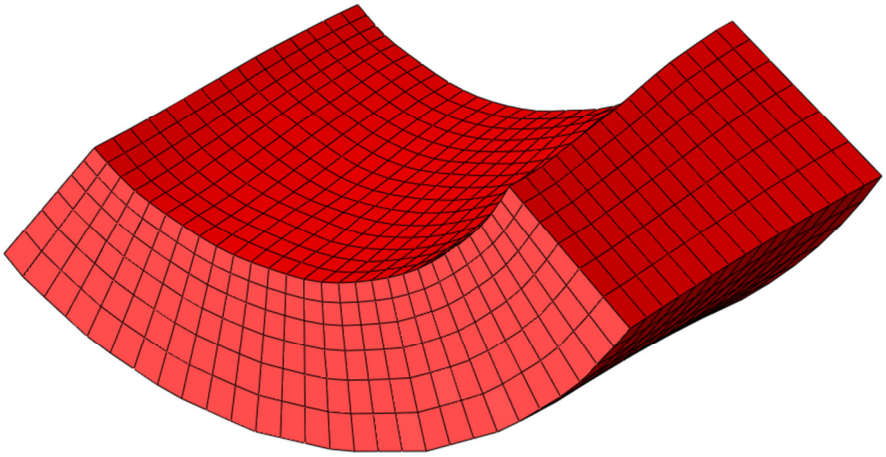

Figure 4.10 – Slice of the vessel wall discretization. The coronary LAD wall is divided into six elements, and the nodes follow an exponential distribution, increasing mesh density towards the lumen.

4.1.3 Plaque identification

As described in Paragraph 2.3, many recent works simulating stent deployment in patient-specific vasculature do not take into consideration plaque components. Nevertheless, the plasticity properties of the diseased tissue greatly influence the behavior of both the stent and the arterial model. In order to achieve a realistic distribution of plaque elements, an algorithm was written using the commercially available software package MATLAB (MathWorks Inc., Natick, MA, USA). The developed function takes as input the coordinates of nodes, the elements and the centerline of the outer arterial wall. Then, the

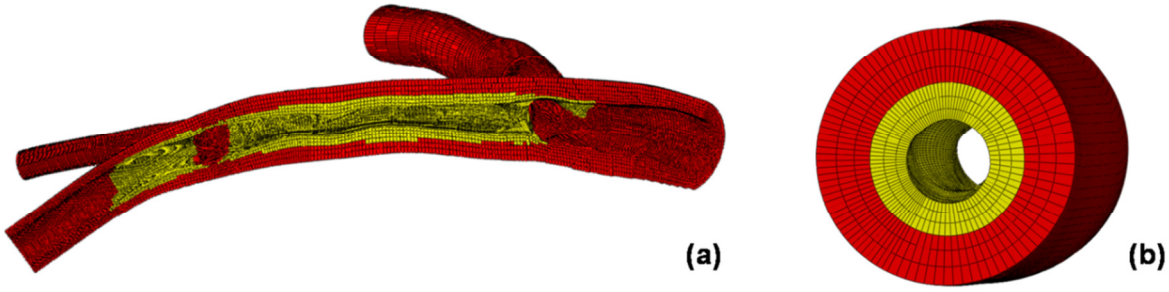

Figure 4.11 – Plaque distribution (yellow) inside the coronary model (red) mesh. On the left, a cut of the main branch in a full view (a). On the right, a slice of the middle stenotic region (b).

algorithm computes the distance of the nodes from the centerline and compares it to the radius that a healthy artery would have in the same position. The generated function considers the arterial healthy radius varying linearly from the inlet radius value to the outlet one, according to the position along the centerline. If the distance of a node is lower than the physiological lumen radius, elements defined by that node were recognized as belonging to the stenotic region of the model. Figure 4.11 shows where the plaque components were obtained.

4.1.4 Material properties

In order to characterize the material model for the coronary artery wall, mechanical properties were obtained from the work carried out by Holzapfel et al. (2005) [50]. The experimental data acquired in the circumferential direction was fitted by means of a hyperelastic isotropic constitutive law. The law describing the material model was based on a sixth-order reduced polynomial strain energy density function (SEDF):

$$U = C_{10}(\bar{I}_1 - 3) + C_{20}(\bar{I}_1 - 3)^2 + C_{30}(\bar{I}_1 - 3)^3 + C_{40}(\bar{I}_1 - 3)^4 + C_{50}(\bar{I}_1 - 3)^5 + C_{60}(\bar{I}_1 - 3)^6 \quad (1)$$

where C_{i0} are material parameters (see Table 4.1) and $\bar{I}_1$is the first invariant of the deviatoric part of the left Cauchy-Green deformation tensor. In order to ease computational analyses, the three arterial wall layers were not differentiated, and the coronary vessel was described with the mechanical properties of the middle layer (tunica media), intermediate of the three. The material parameters to fit the experimental data were automatically calculated using the finite element software ABAQUS.

Atherosclerotic plaques, on the other hand, can be composed of different tissues, from soft fatty tissues to cholesterol crystal to calcifications. Therefore there cannot be a univocal

Table 4.1 – Coefficients of the strain Energy density function for arterial wall and plaque (data in MPa).

	C_{10}	C_{20}	C_{30}	C_{40}	C_{50}	C_{60}
VESSEL WALL	6.52E-03	4.89E-02	9.26E-03	7.60E-01	-4.30E-01	8.69E-02
PLAQUE	2.38E-03	1.89E-01	-3.89E-01	3.73	-2.54	5.73E-01

way to mechanically characterize such tissue. With the aim of simulating mechanical fracture of atherosclerotic plaques, the material was described with an isotropic hyperelasto-plastic model. The hyperelastic part of the stress-strain curve was implemented using the SEDF (1), in which the material parameters C_{i0}were modified to describe the stress-strain curves obtained by Loree et al. (1994) for cellular plaques (see Table 4.1) [55]. The plastic behavior was modeled by means of a perfect plasticity law, with elastic limit set to 0.25 MPa. Both arterial wall and plaque were assumed to have density equal to 1.12 g/cm^3.

4.2 Stent model

In order to accurately simulate the stenting intervention that took place in Hospital Doctor Peset, the same coronary devices were replicated. The cardiovascular procedure consisted in the implant of two 15 mm Endeavor Resolute coronary drug-eluting stents, manufactured by MEDTRONIC (Minneapolis, MN, USA). These stents are characterized by a unique construction process, in which metal modular rings, having circular cross-sections, are first deformed plastically forming crown-shaped loops, and secondly the rings are laser-fused one to another [56]. Such an innovative process, shown in Figure 4.12, guarantees an excellent radial strength and a smooth delivery by means of the edgeless struts.

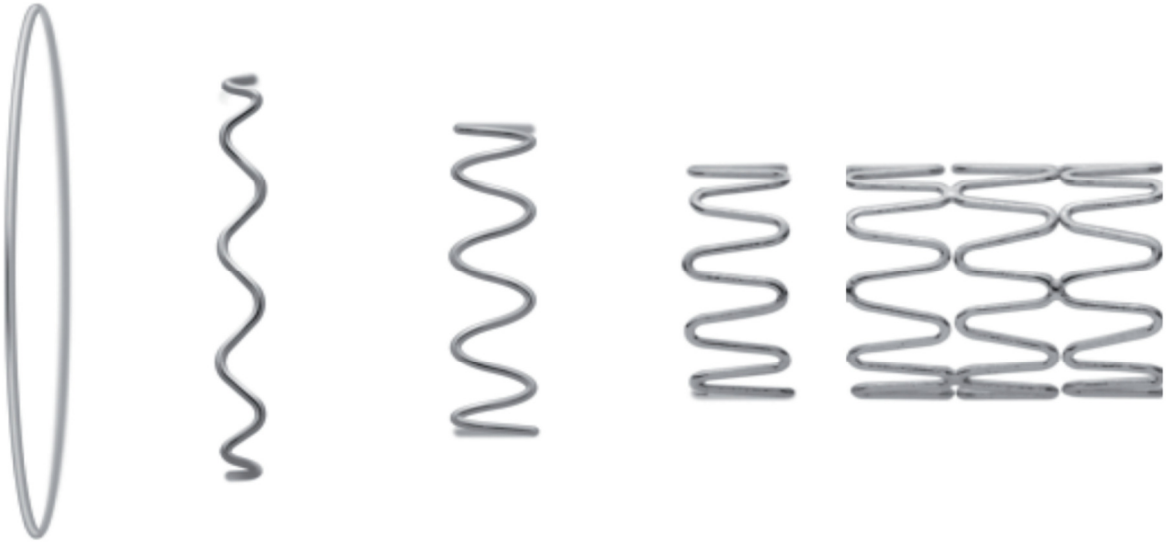

Figure 4.12 – From left to right, construction phases of the Endeavor stent. Single rings are deformed plastically to the desired shape and subsequently laser-fused together. [56]

4.2.1 Geometry

The creation of an accurate solid geometry of the coronary device implanted was performed using the CAD software RHINOCEROS 4.0 Evaluation. The first step to achieve the modular ring was the creation of a centerline curve having the correct inclinations and an adequate curvature radius. Offset curves were generated in order to reproduce the actual strut thickness of 0.0036 inches (91 μm). The ring surface was then created by means of a sweep technique, with a circular cross section. Once the single crowns were made, they were bent to create the rings and subsequently fused together using the Boolean difference method, until a final length of 15 mm was achieved. The built stent was characterized by an external diameter of 1.6 mm.

The various steps to create the single crowns are shown in Figure 4.13, while the final stent solid geometry can be appreciated in Figure 4.14.

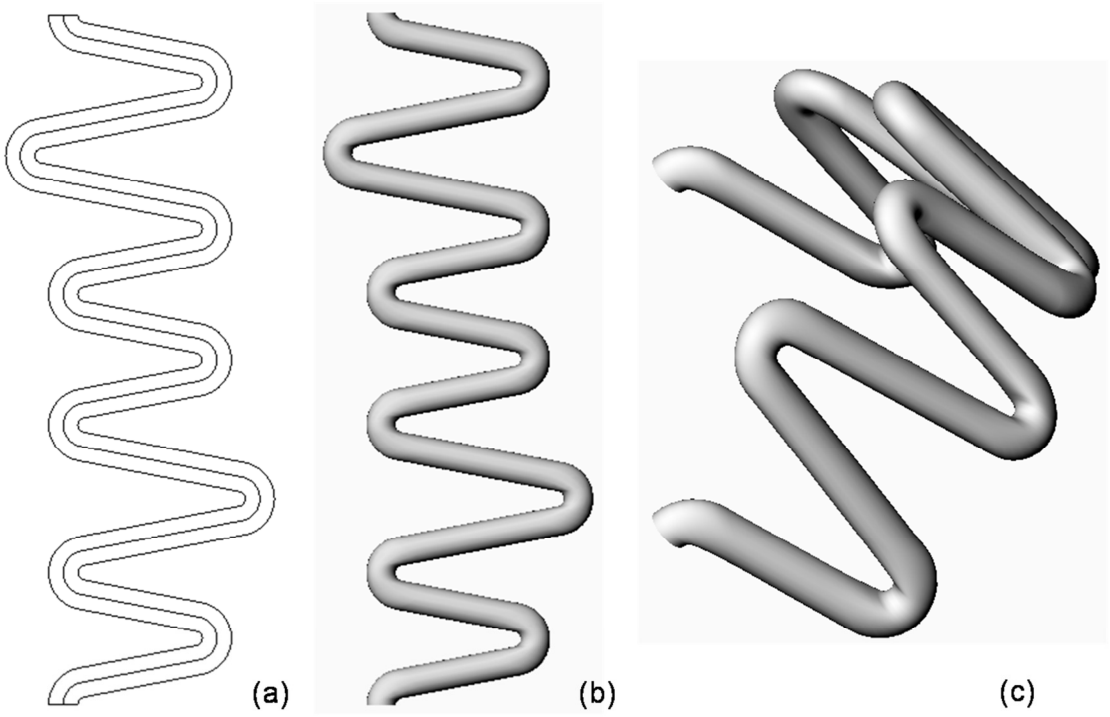

Figure 4.13 – Steps for the creation of the crown-shaped rings. Centerline curve with offset (a), single straight strut (b) and bent strut (c).

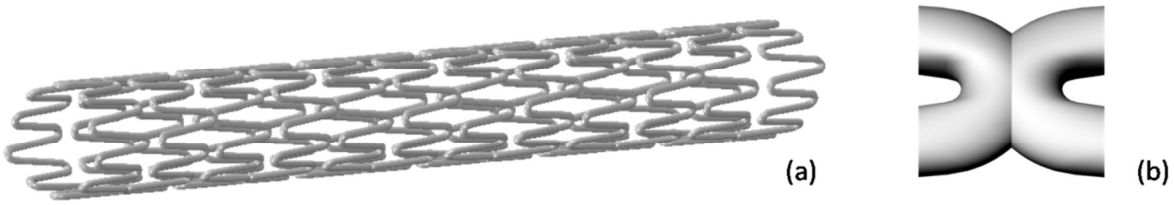

Figure 4.14 – Final 15 mm Endeavor stent model (a) and close-up of the fusion region (b).

4.2.2 Material properties

The Endeavor coronary stent is constructed of a cobalt-chromium alloy. The material model was created using the typical mechanical properties of biocompatible Co-Cr alloys, which were defined in the work of Poncin et al. (2003) [57]. Thus, the cobalt alloy behavior was assumed isotropic and elasto-plastic. The high stiffness and ductility of the model are shown in Figure 4.15.

The material constants used are listed below:

- Young's modulus (E) = 233 GPa
- Poisson's ratio (υ) = 0.35

- Yield stress = 414 MPa
- Fracture stress = 933 MPa
- Deformation at break = 44.8 %
- Density (ρ) = 8.5 g/cm^3

4.2.3 Discretization

In order to generate a high-quality mesh, the CAD surface representing the stent was firstly partitioned, dividing the strut curved regions from the straight ones, in order to facilitate discretization. Secondly, the circular cross sections were discretized by means of a bidimensional quadrilateral mesh. Such mesh was dragged along the strut surface to create solid elements. The curved parts were characterized by a highly dense linear discretization, while the straight regions were divided by means of a bell-curve distribution, in order to generate more elements closer to the curves. After a sensitivity analysis, the chosen mesh presented 32 cross-sectional elements and an increased mesh density where the stress gradient reaches its peak values, as shown in Figure 4.16. The final discretization consisted in 272384 linear hexahedral elements of type C3D8R; it can be appreciated in Figure 4.17.

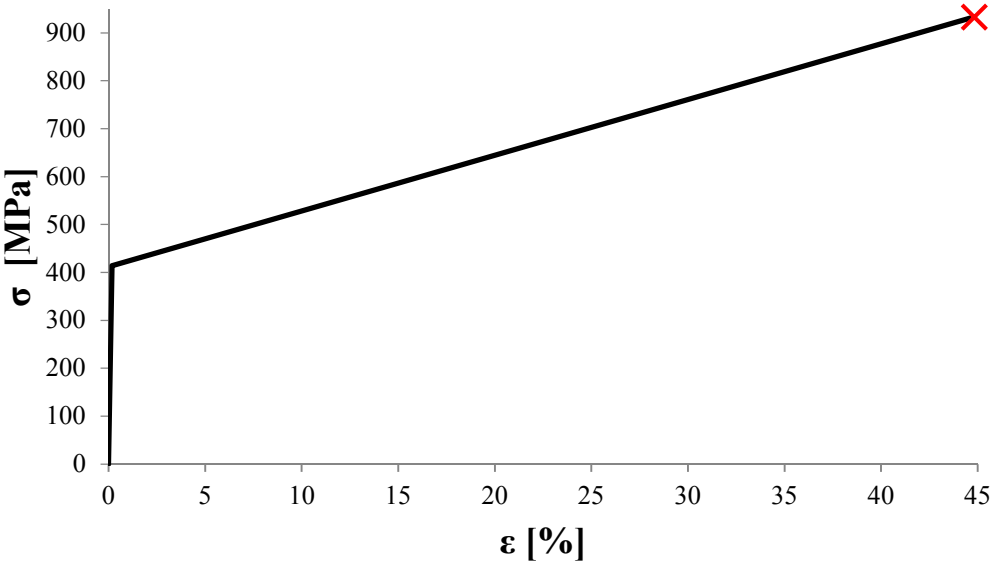

Figure 4.15 – Stress-strain curve for the Cobalt alloy modeled.

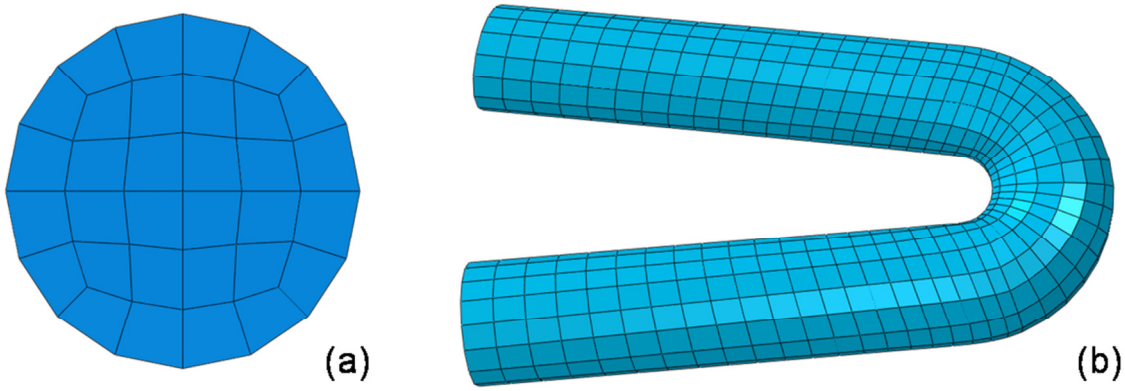

Figure 4.16 – Final generated mesh. Close-ups of cross section and curved strut.

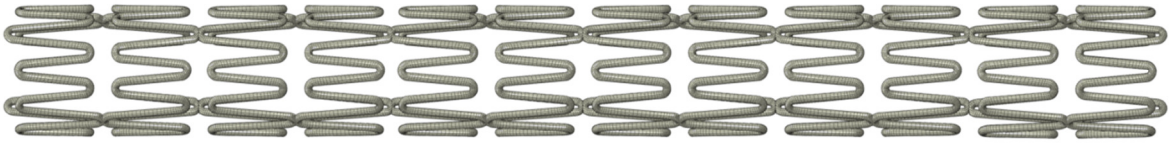

Figure 4.17 – Final mesh generation for the whole 15 mm Endeavor coronary stent model.

4.3 Preliminary simulations

Some preliminary numerical simulations were required to compute the stents implantation with a realistic approach. In particular, the devices used in the intervention procedure, i.e. angioplasty balloon catheters and coronary stents, had to undergo preliminary loading conditions to be accurately positioned inside the tortuous bifurcating region. Also, the stress distribution achieved in the stent model before the actual deployment cannot be neglected to obtain truthful results.

4.3.1 Balloon bending

In order to perform angioplasty and stent expansion simulations, the balloon models created had to be positioned inside the patient-specific bifurcation.

The multi-folded balloons used were imported in the deformed deflated configuration (see Paragraph 3.1.1). First, adequate CAD geometries of the catheter and the outer guide were generated using the centerlines obtained using VMTK. This procedure was carried out creating circumferences perpendicular to the centerline and constructing a loft surface. Subsequently, in the bending procedure, the nodes composing a balloon end were subject

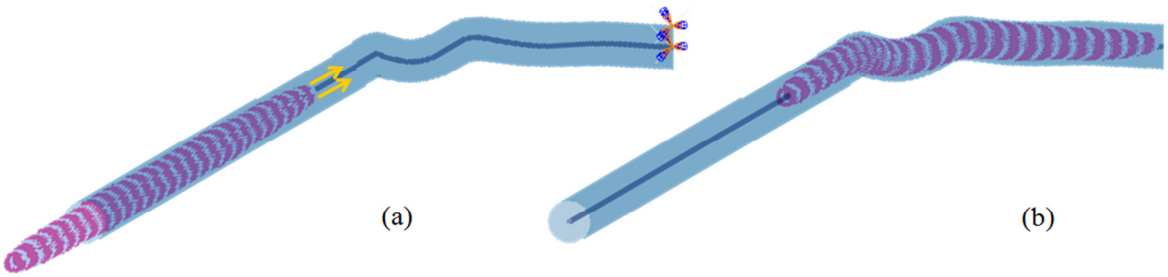

Figure 4.18 – On the left, initial assembly for balloon bending, with loads and encastre constraints displayed (a). On the right, bent balloon model inside the guides (b). Rigid body properties are assigned to balloon elements colored in purple.

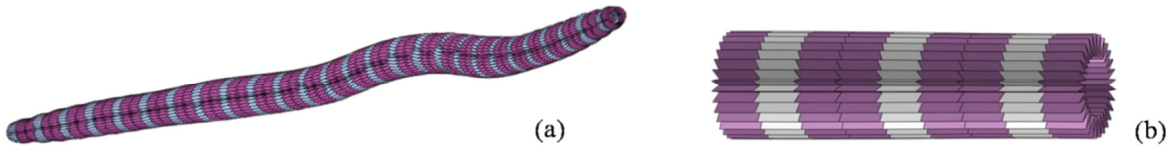

Figure 4.19 – Final finite element bent balloon model (a), and close-up (b) highlighting the regions subjected to constraint.

to concentrated loads pulling the whole model along the created guide, which was fully constrained. Contacts between the balloon internal surface and the guide were modeled with the general contact algorithm, imposing a hard frictionless contact. Self-contact was assumed for the whole balloon model. In order to bend the balloon maintaining the multi-folded configuration, several elements were subject to a rigid body constraint. The simulations were performed using the finite element package ABAQUS/Explicit. The initial assembly and the bent balloon are shown in Figure 4.18; highlights on the regions subjected to constraint can be appreciated in Figure 4.19.

4.3.2 Stent crimping

The Endeavor coronary stent is supplied to the cardiology personnel already crimped tightly around the balloon [53]. Such a procedure induces a high level of plasticization on the struts that affects the subsequent stent deployment. In order to simulate the actual crimping process, a rigid cylindrical surface was created and placed around the stent model (see initial assembly in Figure 4.20). By means of a radial displacement control, the cylinder decreased its diameter to achieve a final external stent diameter of 1.1 mm, a common coronary stent post-crimping value. The rigid surface then underwent an opposite

radial displacement, leaving the stent to recover its elastic deformations. All contacts were modeled having a hard normal behavior and a frictional tangential behavior, with friction coefficient set to 0.3. The numerical studies were computed using ABAQUS/Standard, resolving a non-linear static analysis, neglecting all inertia effects. The high local stress distribution, present even after elastic recovery, can be appreciated in the radial views in Figure 4.21. The whole 15 mm stent model, before and after crimping procedure, is shown in Figure 4.22.

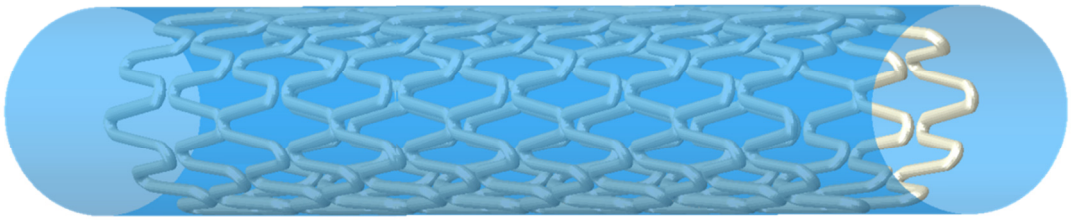

Figure 4.20 – Initial assembly of the crimping simulation. An external cylinder is controlled in displacement gradually reducing its diameter.

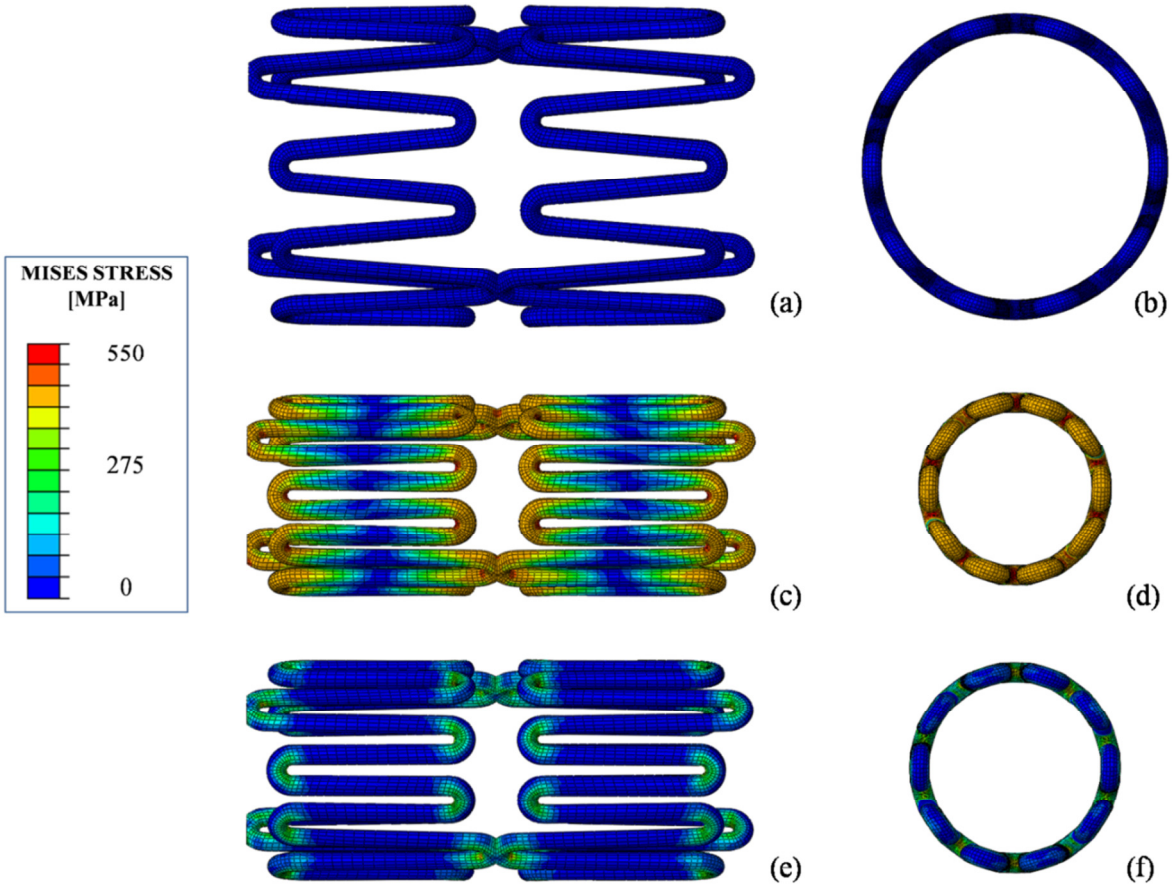

Figure 4.21 – Longitudinal view of two struts and radial views of the stent model with Von Mises stress distribution, before (a, b), at full crimping (c, d) and after elastic recovery (e, f).

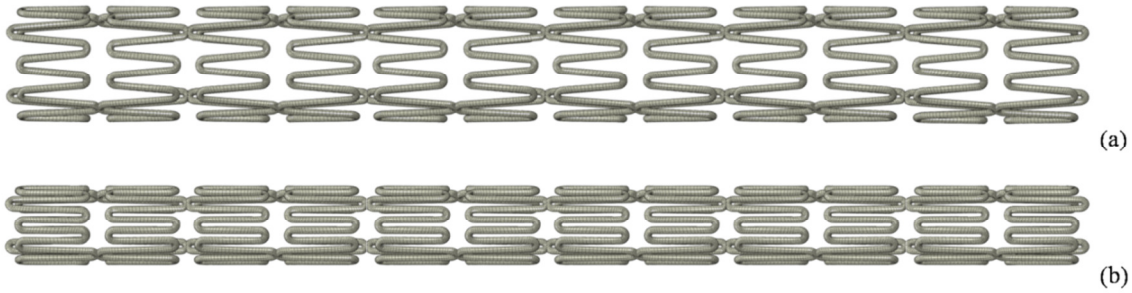

Figure 4.22 – The Endeavor stent model used in the coronary intervention that took place, before (a) and after (b) the simulated crimping process.

4.3.3 Stent bending

After crimping, the two coronary stent models underwent bending simulations to be accurately positioned in the complex patient-specific geometry. In order to perform the bending analyses, two guide models were created based on the patient-specific bifurcation. To obtain realistic stress distributions on the bent struts, the stent was pushed against the guide imposing longitudinal displacement to the nodes composing the laser-fused links between the struts, as shown in Figure 4.23. The regions were also constrained in the radial and circumferential direction. Such boundary conditions were removed once the links approached the first curve, in order to let the stent bend freely along the guide.

A final step was added after complete bending, constraining one stent node on the distal end, allowing the stent to adapt to the bending guide and reach a less critical stress configuration. Contacts were set to have friction coefficient equal to 0.3 and the normal behavior was modeled with a linear pressure-overclosure having stiffness of 1000. The guide was considered a rigid body and was fully constrained. In order to start from a realistic stress distribution along the stent model, the stress distribution was imported from the previously described crimping simulation. The finite element study was carried out using ABAQUS/Standard, in order to achieve quasi-static simulations.

An example of stent bending was performed prior to the patient-specific case. A 10 mm Endeavor Resolute coronary stent was first crimped and subsequently bent using a guide with a 30° angle. The results, which can be found in Figures 4.24 and 4.25, show how the bending occurred step by step, and how the stress distribution changed during the analysis, starting from the imported stress distribution due to crimping. Von Mises stresses reach their maximum values where two subsequent struts have different inclination, and soon drop in linear segments of the guide.

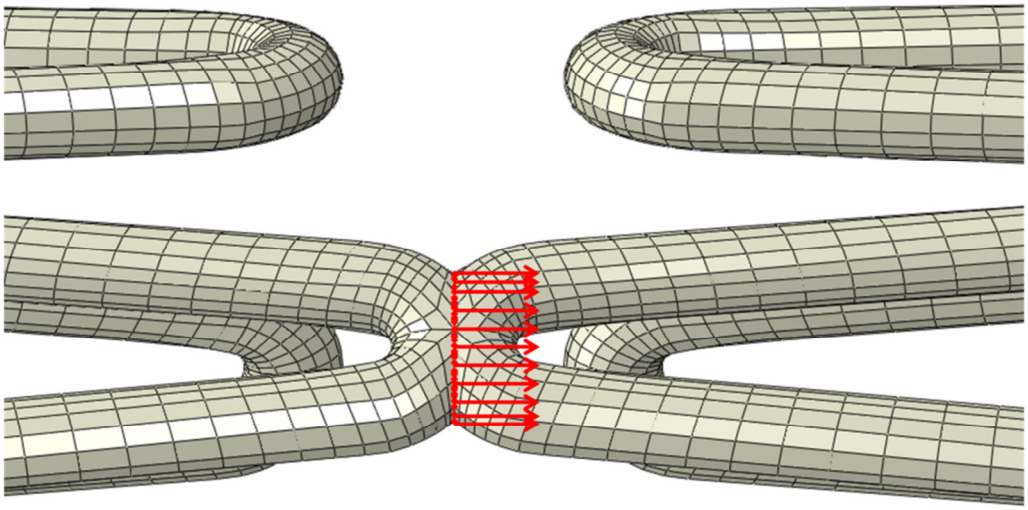

Figure 4.23–Close-up of the nodes on which the boundary conditions are applied during bending. The node set is the fused region between two crowned-shaped rings.

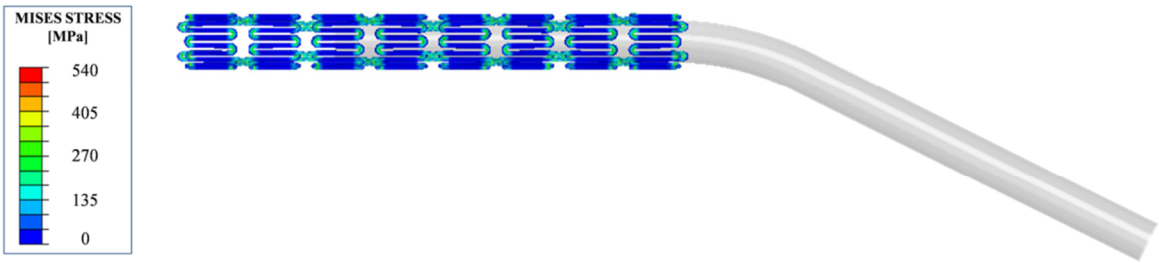

Figure 4.24–Example bending: initial assembly. The stent model presents post-crimping stress distribution.

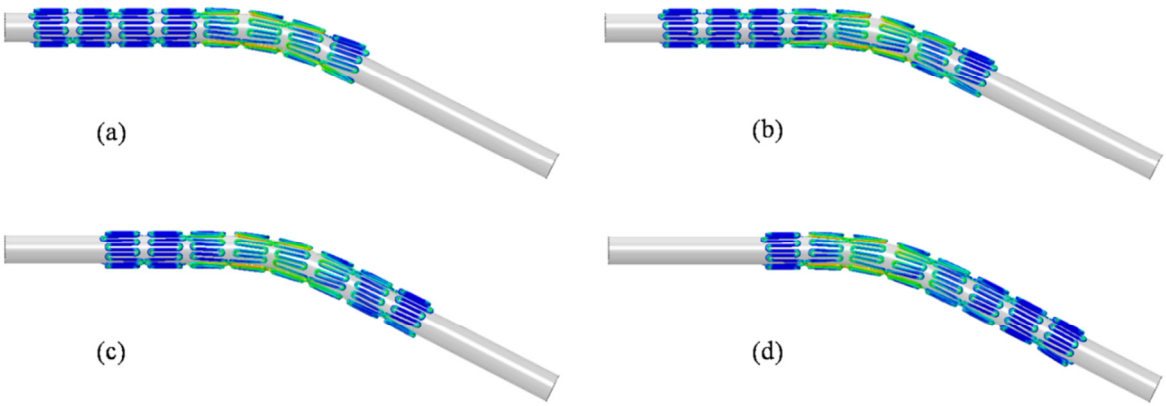

Figure 4.25 – Example bending: four steps of the bending analysis. It is noticeable how the stress has its peaks in the most bent regions. Elsewhere, stresses do not change heavily.

4.4 Patient-specific stenting simulation

The actual stenting intervention case that took place consisted of a provisional side branch T-stenting procedure involving two drug-eluting coronary stents. Initially an angioplasty procedure was performed, helping the subsequent stent insertion, by means of a pre-dilation 15 mm balloon with an external diameter of 2.5 mm and a pressure of 13 atm. Subsequently two Endeavor Resolute coronary stents were implanted in the stenotic region. Firstly the distal stent was expanded by means of a 2.75 mm diameter balloon at a pressure of 12 atm. Secondly the proximal stent was expanded using a larger 3 mm x 15 mm balloon, reaching a maximum inflation pressure of 14 atm. The second stent was positioned creating an overlap between the two devices of about 2-3 mm. The stenting intervention was successful, as proved by post-stenting CT angiographies.

4.4.1 Angioplasty procedure

In order to simulate the angioplasty prior to stent implantation, a 2.5 mm x 15 mm balloon was imported in the deformed configuration obtained by a previous bending analysis. The balloon was positioned centrally in the region characterized by the highest degree of atherosclerosis. Once the deflated balloon model was inserted in the region of interest, an increasing pressure acted on the internal balloon surface reaching a maximum value of 1.3 MPa. The load was applied gradually using a smooth amplitude curve. The balloon was constrained around a catheter guide modeled on the pre-interventional lumen centerline, by assigning rigid body properties to the end elements of the balloon and setting a hard contact between such elements and the external surface of the guide. The catheter model was fully constrained. The arterial bifurcation had its end nodes constrained in the longitudinal direction by means of four cylindrical coordinate systems. The time period of the inflation step was set to 0.5 s.

Subsequently, to simulate the balloon deflation and to allow the arterial elastic recoil, a second step was carried out with duration of 0.2 s, neglecting previous interactions and maintaining boundary conditions for the catheter and the artery models.

All contacts were modeled as frictional, with the penalty coefficient set to 0.2 for the interaction between the balloon model and the guide, and decreased to 0.06 between balloon and artery surfaces [58]. The described finite element analysis was performed

using ABAQUS/Explicit. Thus, energies were monitored to guarantee the achievement of quasi-static results. Moreover, an adequate semi-automatic mass scaling governed the time increment. To dampen dynamic oscillations, viscous pressure was applied to the external surface of the arterial model.

4.4.2 Double stenting procedure

After undergoing crimping and bending analyses, the two coronary stent models achieved an adequate configuration to fit the bifurcated patient-specific artery, enlarged after angioplasty procedure. Two 19 mm balloon models were created in the inflated configuration and deflated as multi-folded. After bending along a guide created following the post-angioplasty lumen, the balloons were positioned inside the two stents. The expansion of the two stent models was simulated applying an increasing pressure to the internal surfaces of the balloon models, and carried out in four different steps, performed using ABAQUS/Explicit.

In order to replicate the actual stenting intervention, the distal stent was expanded first. In this step, having a time period of 0.42 s, an increasing pressure acted on the balloon's inner surface, reaching a maximum of 1.2 MPa. The balloon was constrained as for the angioplasty step, the guide was considered a rigid body having an encastre constraint and the artery maintained the previous boundary conditions. Contacts were created between the stent and the artery, the balloon and the stent, the balloon and the artery, the balloon and the guide.

The second step allowed elastic recoil of the stent and artery models, with a duration of 0.1 s. The only contact maintained was the one between the stent and the artery.

The third step simulated the proximal stent expansion. An overlap of about 2 mm between the two stents was left, to obtain the realistic configuration. The expansion was simulated as for the distal stent, modifying the maximum pressure load to 1.4 MPa. Also, interactions between the two stent models and between the proximal balloon and the expanded distal stent were considered. The step had a duration of 0.42 s.

The final step allowed full elastic recovery and the reaching of an equilibrium condition. The time period was set to 0.5 s.

Contacts involving the arterial surface were all modeled using a hard normal behavior and a frictional tangential behavior with penalty of 0.06. All other contacts had a friction

Table 4.2 – Steps summary for the stenting intervention simulated.

STEP	DESCRIPTION	LOADS	BCS	CONTACTS
1	Angioplasty balloon inflation	Pressure of 1.3 MPa acting on the balloon inner surface		Balloon – catheter, balloon – artery.
2	Elastic recoil post-angioplasty	No loads applied		Interactions removed.
3	Distal stent expansion	Pressure of 1.2 MPa acting on the distal balloon inner surface	Artery: end nodes constrained in the longitudinal direction.	Balloon – stent, balloon – artery, balloon – catheter, stent –artery.
4	Elastic recoil post distal expansion	No loads applied	Balloons: end elements rigid.	Stent – artery.
5	Proximal stent expansion	Pressure of 1.4 MPa acting on the proximal balloon inner surface	Catheter guides: fully constrained.	Balloon – stents, balloon – artery, balloon – catheter, stents –artery, stents with each other.
6	Elastic recoil post proximal expansion	No loads applied		Stents –artery, stents with each other.

coefficient of 0.2. Energies were monitored, so that the ratio of kinetic to internal energy did not exceed 5%. An adequate viscous pressure was applied to the stents' surfaces during all steps. All steps are summarized in Table 4.2.

4.5 Post-analysis assessments

The simulations carried out contained various quantities which could help coronary stent design and facilitate clinical choices, predicting patient-specific interventional outcomes.
Firstly, the ratio of kinetic energy to internal energy was constantly monitored in order to obtain quasi-static simulations, thus neglecting time and inertial effects. Such a ratio must not be greater than 5%, especially where plastic deformations are present.
Secondly, the crimping simulations were assessed, in terms of stress distribution on the stent struts and final diameters obtained, which had to be compatible with the patient-specific bifurcation lumen.

The bending simulations were evaluated focusing on the stresses reached and on the plastic deformations obtained. High plastic strain variations would give great importance to the whole lumen path during insertion.

The double stenting procedure was thoroughly analyzed starting from geometrical considerations, looking into the stent expansion, the lumen opening reached and the strut deformations. Stresses on the stent were investigated by examining the Von Mises stress distribution and the regions most heavily affected by stent expansion. Particular attention was paid to the local stresses obtained where the overlap between the stents occurred, a critical part of the intervention. The arterial response to the stenting procedure was investigated in terms of maximum principal stress distribution, highlighting where the peaks were reached.

Finally, the post-interventional lumen obtained after the whole finite element analysis was compared to the real post-stenting lumen, using the triangulated surface obtained by Cárdenes et al. by means of the previously described reconstruction technique (see Paragraph 1.2.2). The comparison between the lumen geometry pre and post-stenting procedure is shown in Figure 4.26.

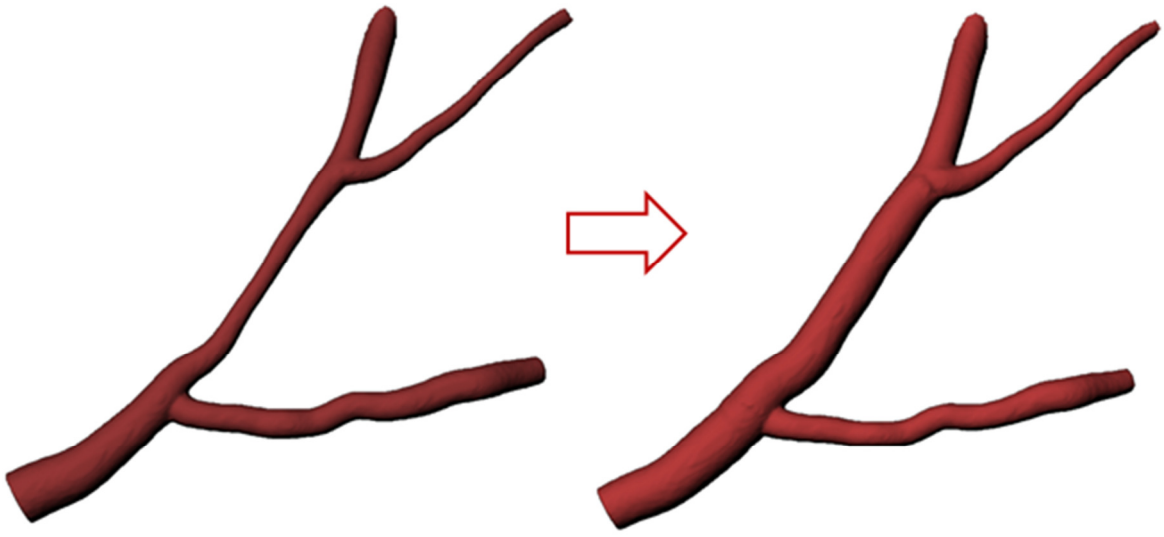

Figure 4.26 – Triangulated surface of the bifurcated coronary artery before (left) and after (right) the intervention [23].

Chapter 5

Results and discussion

The fifth chapter shows the results obtained and discusses the outcomes in terms of geometrical considerations and of mechanical stresses and strains obtained on the stent models and on the arterial wall. Furthermore, a comparison between the finite element results and the actual intervention is made.

5.1 Verification of quasi-staticity

Before analyzing any mechanical result, the quasi-staticity condition has to be verified, ensuring the reliability of the simulations performed with an explicit dynamics model. As previously mentioned, such condition is validated by monitoring the energy plots during the whole analyses, focusing on the ratio between kinetic energy and internal energy. In particular, such ratio has to be close to zero in all the parts of the model, especially in plastic materials, where permanent plastic deformations could arise. Therefore, the most important energy checks have to be performed on the two stents.

The preliminary simulations of stent crimping and bending were performed using ABAQUS/Standard, a product that solves static stress-analyses, so no kinetic energy is present and inertial effects are neglected by definition.

The subsequent simulation of the stenting intervention was performed using ABAQUS/Explicit, a product solving explicit dynamic problems. Thus, the simulation had energy plots carefully monitored. Plastic strains were already high, due to the previous simulations, so great attention was paid to the ratio of kinetic energy to internal energy (E_K / E_I) for each stent model to avoid unrealistic permanent plastic deformations. It is suggested that the kinetic energy of the deforming material should not exceed a small fraction (typically 5% to 10%) of its internal energy throughout the process [59].

Figure 5.1 shows the E_K / E_I ratio during the double stenting simulation for the two stent models. It is maintained lower than 5% throughout the whole analysis. Such ratios ensure that the process operates in the quasi-static regime. As predictable, kinetic energy increases during stent expansion and rapidly goes to zero in subsequent steps. The contact between the two stents does not greatly affect the E_K / E_I ratio and is noticeable by a very slight increase in the distal stent kinetic energy.

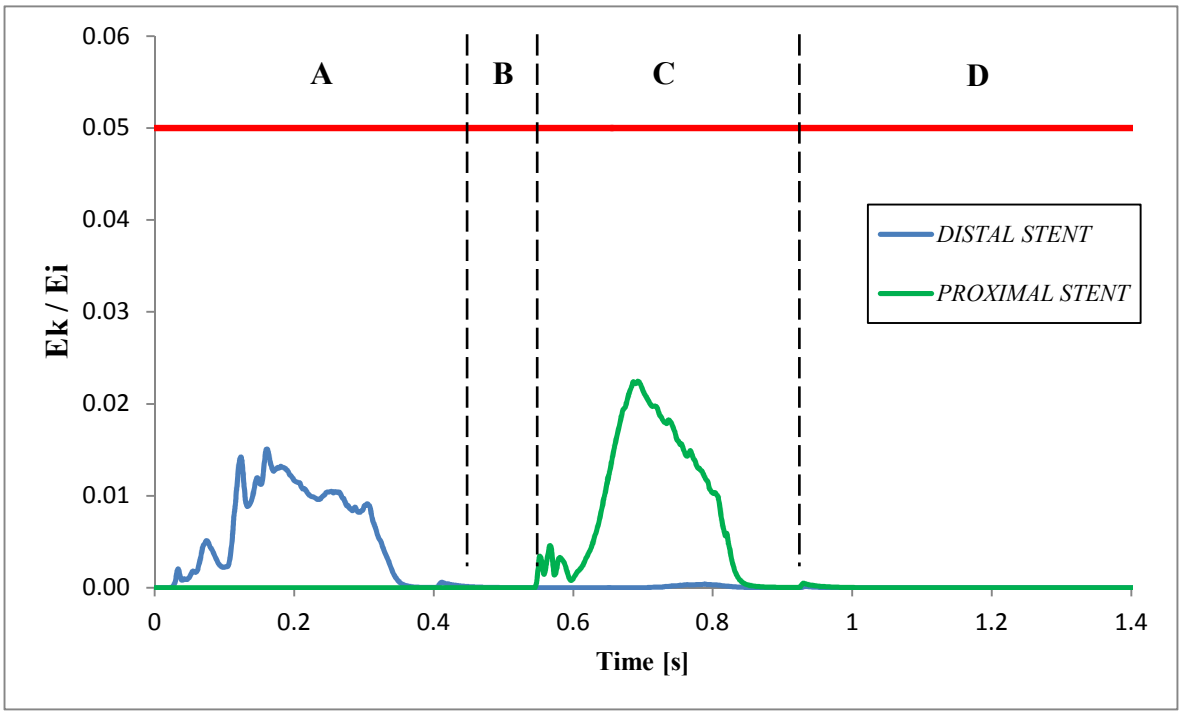

Figure 5.1 – Ratio of kinetic to internal energy for both stents during the four steps of stenting implantation: distal stent expansion (A), elastic recoil (B), proximal stent expansion (C) and final recoil (D). The ratios for both the stent models are significantly under the 5% limit suggested (red line).

5.2 Preliminary simulations: crimping and bending

5.2.1 Crimping simulations analysis

Through the crimping simulations, the stent decreased its external diameter from 1.6 mm to 1.1 mm. The Von Mises stress distribution appeared to be greatly symmetrical, having peak local stresses in the curved regions (see Fig. 5.2). The elastic recoil after crimping caused the stent external diameter to increase from 1 mm to 1.1 mm (see Fig. 5.3). The stent is able to remain in the crimped configuration due to the high plastic strains generated. The plastic limit is reached in the curved regions only and not in the straight parts of the struts, causing the crowned-shaped rings to maintain different curvature radii, without modifying the straight parts. Figure 5.4 shows the equivalent plastic strains (PEEQ) distribution on a curved region of a strut.

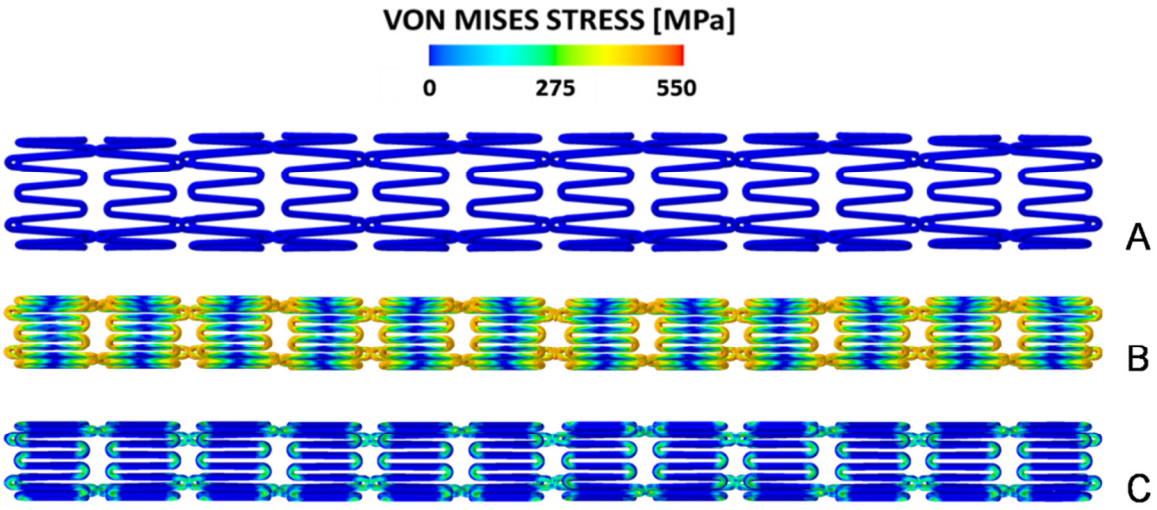

Figure 5.2 – Von Mises stress distribution on the whole stent model, at initial configuration (A), at full crimping (B) and after elastic recoil (C).

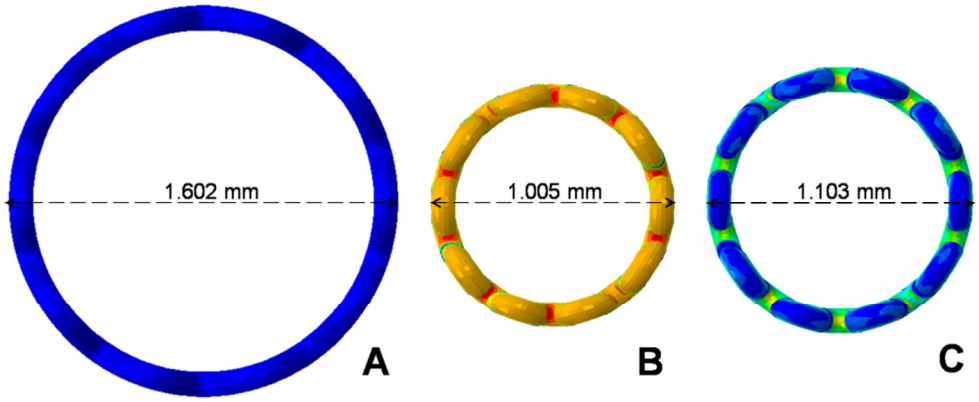

Figure 5.3 – Cross sectional views and diameters of the stent models at full crimping (A) and after elastic recoil (B).

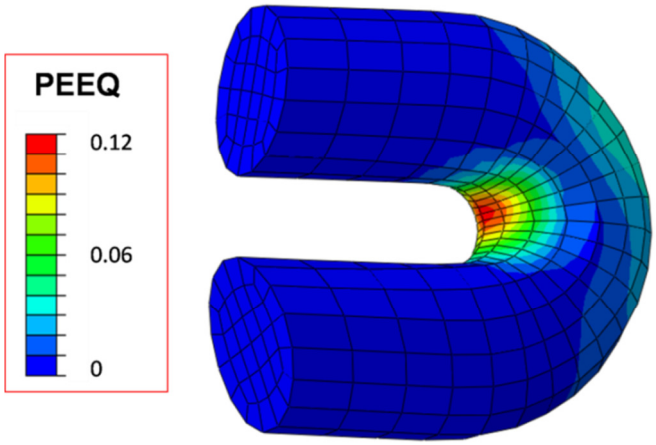

Figure 5.4 – PEEQ contour map of a curved region of a central stent strut after crimping procedure.

5.2.2 Bending simulations analysis

The two coronary stent models underwent bending simulations utilizing different guides, in order to be accurately positioned inside the tortuous coronary lumen. The stents modified their stress distributions along the struts, and the variations during stent advancement are shown in Figures 5.5 and 5.6. Also, the importance of the final step, when all the displacement boundary conditions were removed, is noticeable, as the stress distribution in the most proximal struts of the stents changes remarkably, decreasing its local peaks and reaching a new static equilibrium. The plastic deformation maps (see Fig. 5.7) clearly state that no plasticity is added by the bending of the stent. This result is relevant and makes the history of bending negligible while positioning the stent, also considering that the arterial tracts preceding the coronary bifurcations have greater diameters and higher curvature radii, which would not affect such a small intravascular device. In the light of these outcomes, it has been proved that for accurate mechanical analysis the stent model could be bent only in its final path, reaching the final configuration. Table 5.1 provides the numerical results of the bending simulations in terms of Von Mises stress and PEEQ, proving how the stress distribution changes heavily, while the maximum equivalent plastic strain increases its value less than 1% during the analysis.

As a result of the two preliminary simulations, the bent stent models were able to be correctly positioned in the patient-specific coronary bifurcation. The accurate post-bending configuration of the stent models is shown in Figure 5.8.

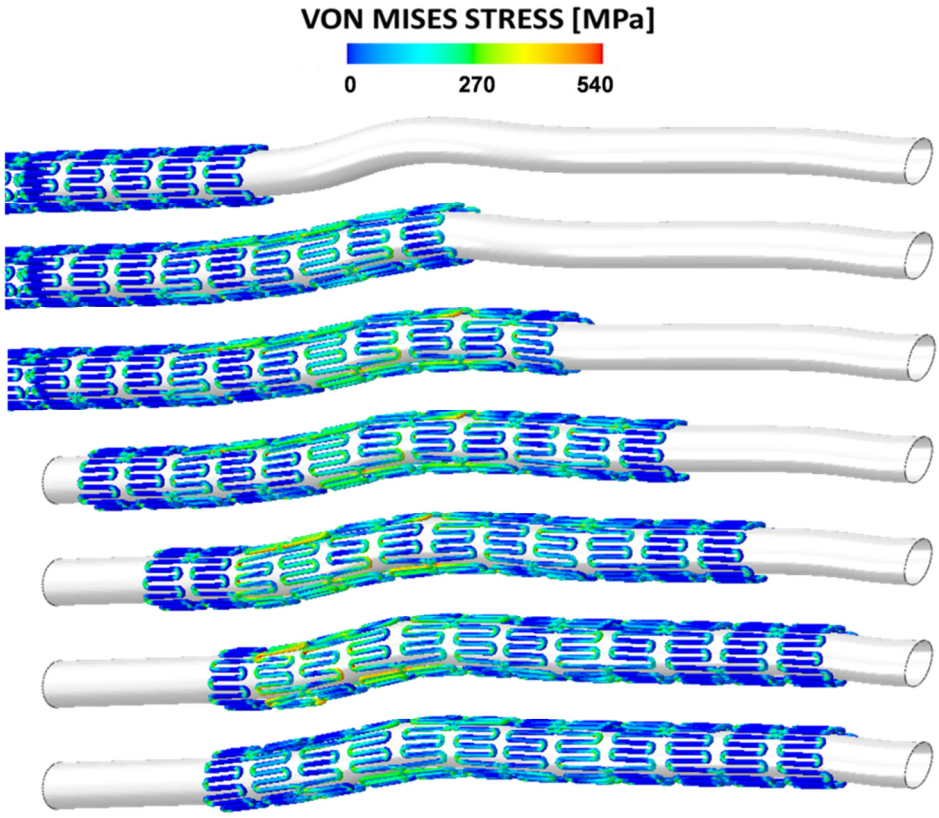

Figure 5.5 – Simulation of the proximal stent advancement along the guide created.

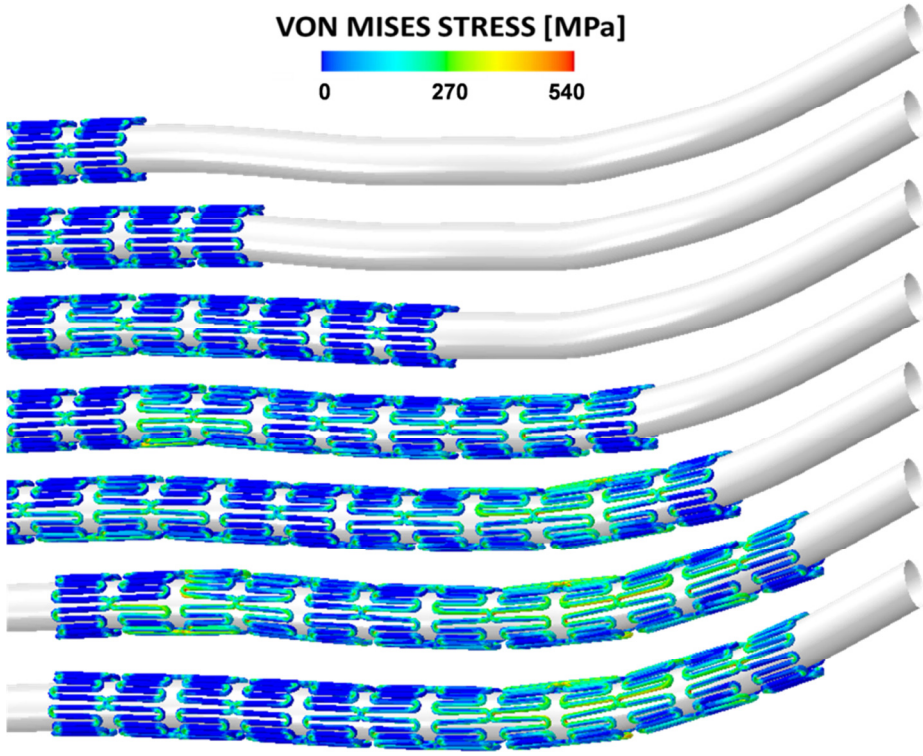

Figure 5.6 - Simulation of the distal stent advancement along the guide created based on the post-angiography centerline.

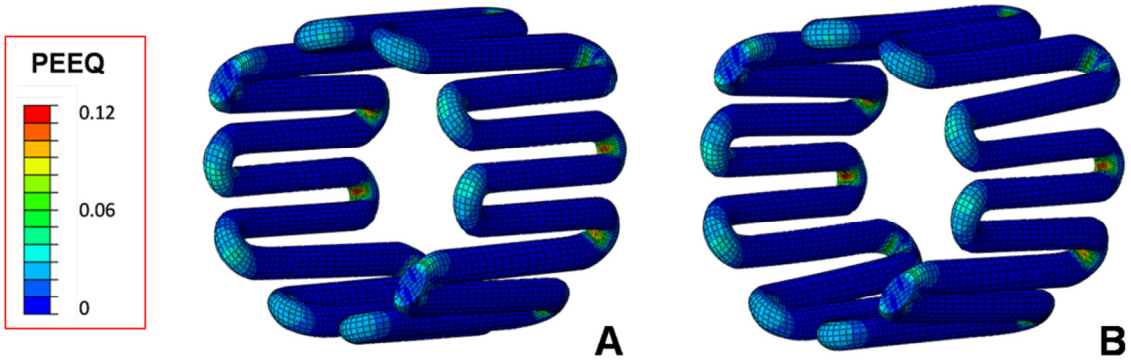

Figure 5.7 – Plastic equivalent strain map on a middle stent ring, before (A) and after (B) bending simulation. It is noticeable how the bending deforms the strut without changing the PEEQ distribution.

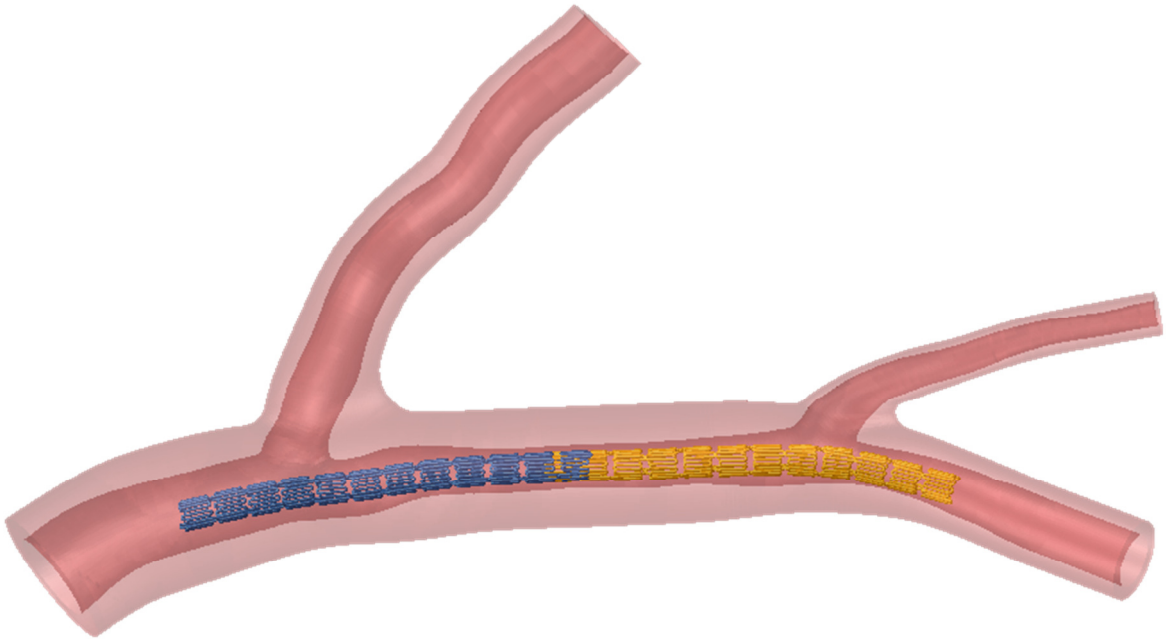

Figure 5.8 – Crimped and bent stent models positioned inside the post-angiography bifurcation.

Table 5.1 – Stress and PEEQ peaks reached during the bending simulations for the two stents.

	PRE-BENDING	MAX ACHIEVED	POST-BENDING
PROXIMAL STENT			
σ max [MPa]	454	546	533
PEEQ	0.1179	0.1187	0.1187
DISTAL STENT			
σ max [MPa]	454	544	539
PEEQ	0.1179	0.1181	0.1181

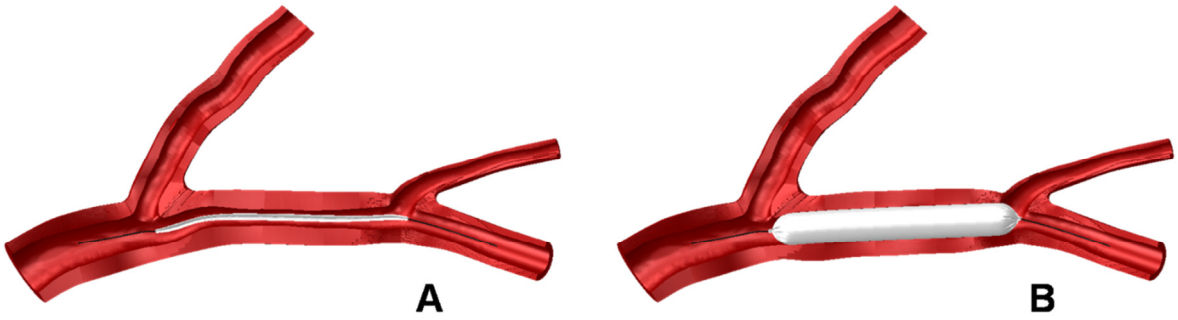

Figure 5.9–Angioplasty intervention simulation. The balloon is inserted to the most stenotic region of the coronary artery (A), and subsequently inflated to a 2.5 mm diameter (B).

5.3 Angioplasty simulation assessment

Figure 5.9 shows the first step of the clinical intervention: the balloon angioplasty simulation. The final expanded configuration to 2.5 mm of diameter was achieved by means of a gradually increasing pressure acting on the internal balloon surface. Changes in the lumen opening are relevant at full expansion, but diminish after the strong arterial elastic recoil (see Fig. 5.10). The coronary stenosis degree decreases from a maximum of about 77% to approximately 69%. Such results determine an easier stent positioning in the stenotic region, but are not satisfactory in terms of lumen re-opening. This could justify the subsequent stents implantation.

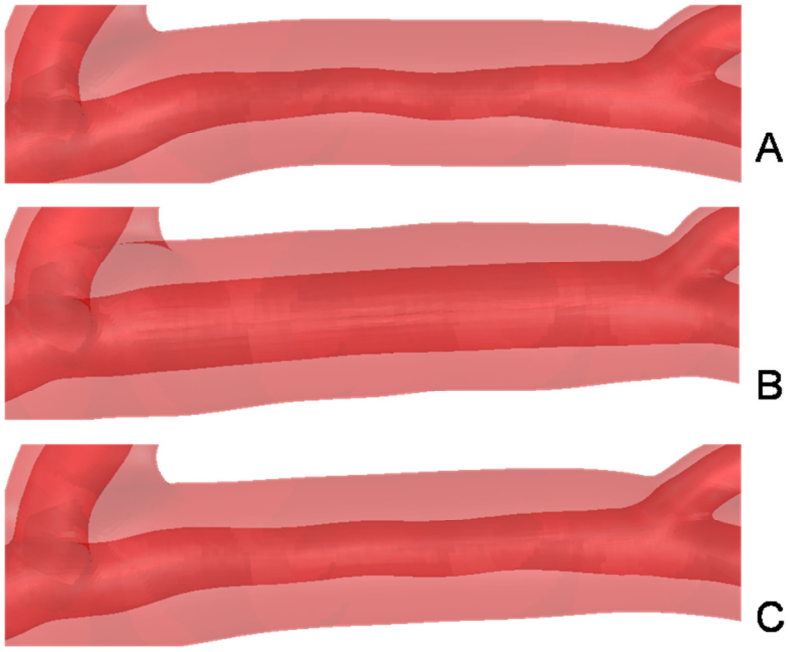

Figure 5.10 – Changes to the lumen of the stenotic region with angioplasty intervention. Region of interest before procedure (A), at balloon full expansion (B) and after procedure (C).

5.4 Double stenting procedure assessment

The following steps performed in order to replicate the whole intervention, from angioplasty to stents implantation, are shown in Figure 5.11. The stenotic artery enlarges its lumen as expected and the tortuous vessel path is straightened. Despite the high initial stenosis degree, the stenting procedure is successful. The Von Mises stress distribution maps on both stents, shown in Figure 5.12, reveal peak stresses in the inner part of the curves, reaching a maximum stress of 914 MPa in the distal stent. The overlap between stents was a critical region of the procedure, and a fair increase in local stresses was achieved in the distal stent struts close to the proximal device, subsequent to the expansion of the latter (see Fig. 5.13).

Figures 5.14 and 5.15 depict the single stent deployments, underlining the variations in the Von Mises stress contour maps. The innovative balloon expansion can be appreciated, in which the balloon ends slide across the internal catheter guide during inflation, reproducing the stent expansion procedure more realistically than previous models.

Higher plastic strains are achieved during expansion, allowing the stents to maintain their expanded configuration inside the coronary artery, as proved by the contour maps in Figure

5.16. Table 5.2 provides the history of maximum stress and PEEQ obtained by the two Endeavor stents during the whole procedure.

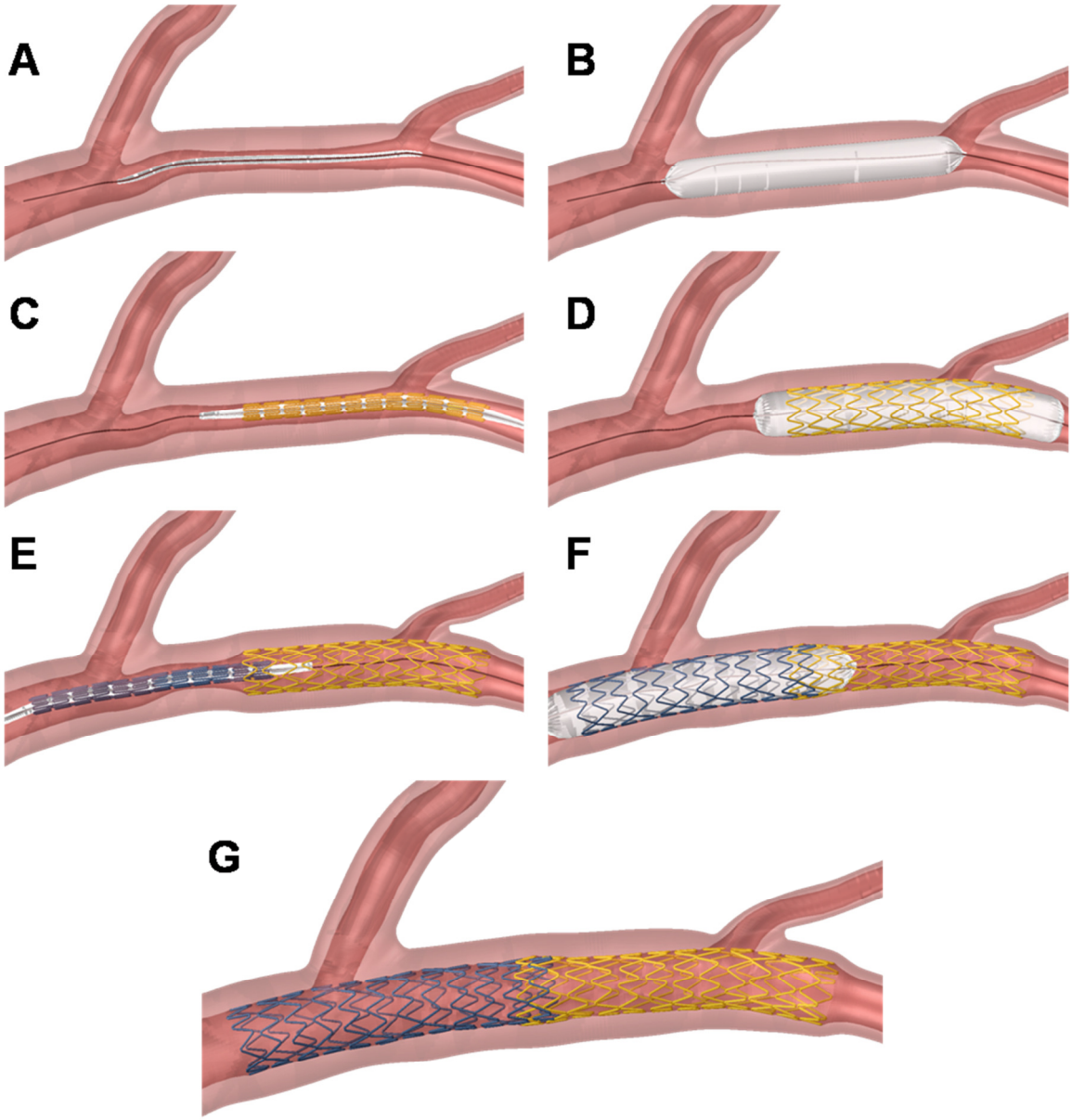

Figure 5.11 – Intervention simulation steps. Insertion of angioplasty balloon using catheter modeled on pre-interventional lumen (A), angioplasty balloon inflation (B), distal stent and balloon insertion using catheter modeled on post-angioplasty lumen (C), distal stent expansion (D), proximal stent and balloon insertion (E), proximal stent expansion (F) and final configuration after elastic recoil (G).

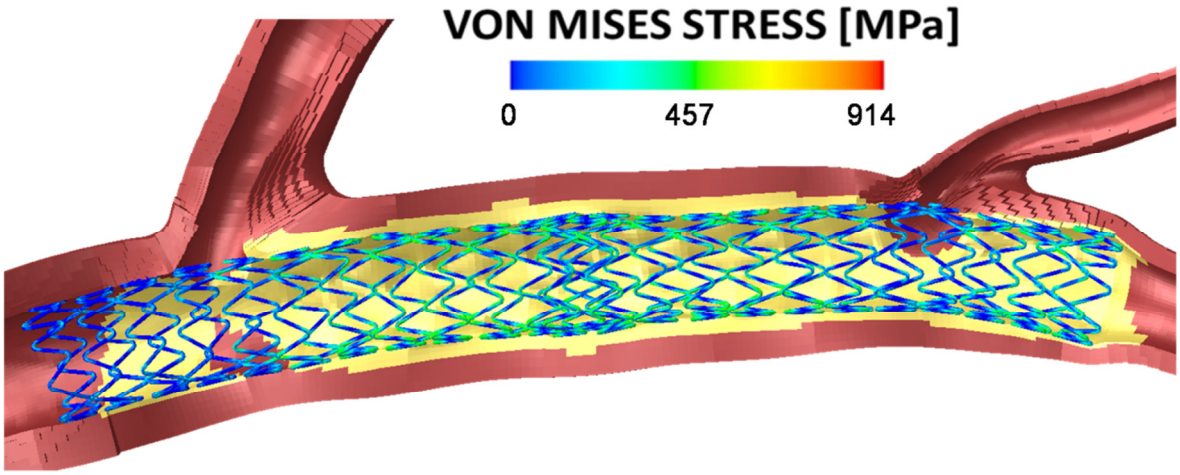

Figure 5.12 – Von Mises stress distribution for the two stent models implanted in the stenotic bifurcated artery.

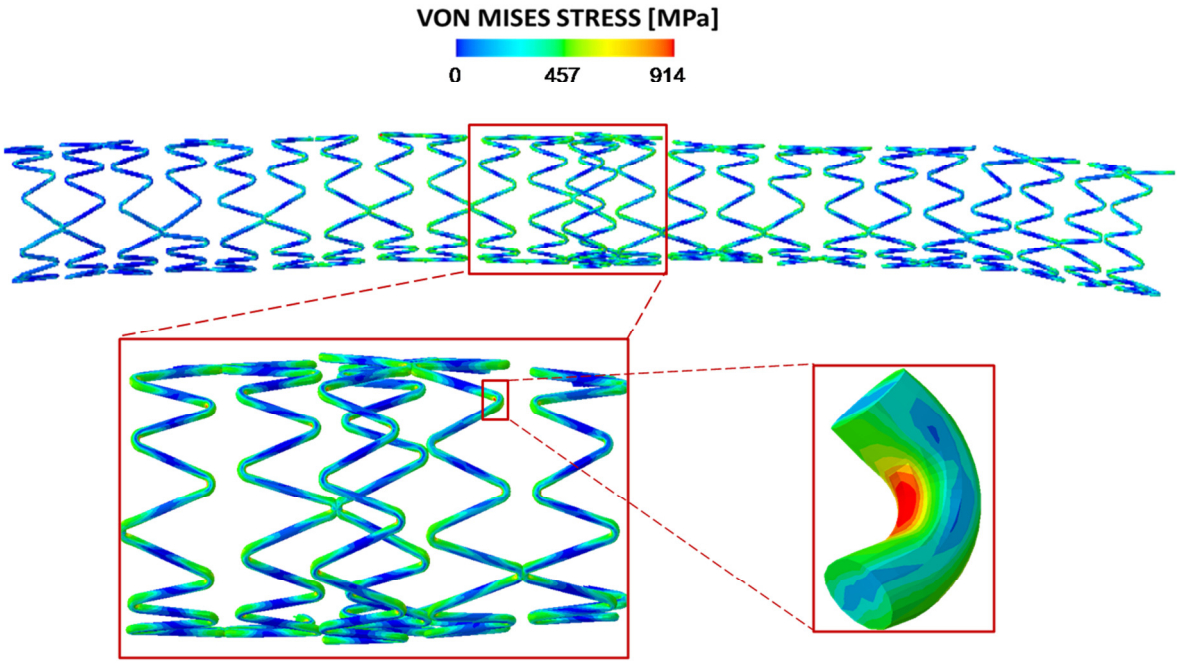

Figure 5.13 – Von Mises stress contour map of the two stents after the final elastic recoil. The overlap region is magnified, as well as the curved region characterized by the maximum stress achieved.

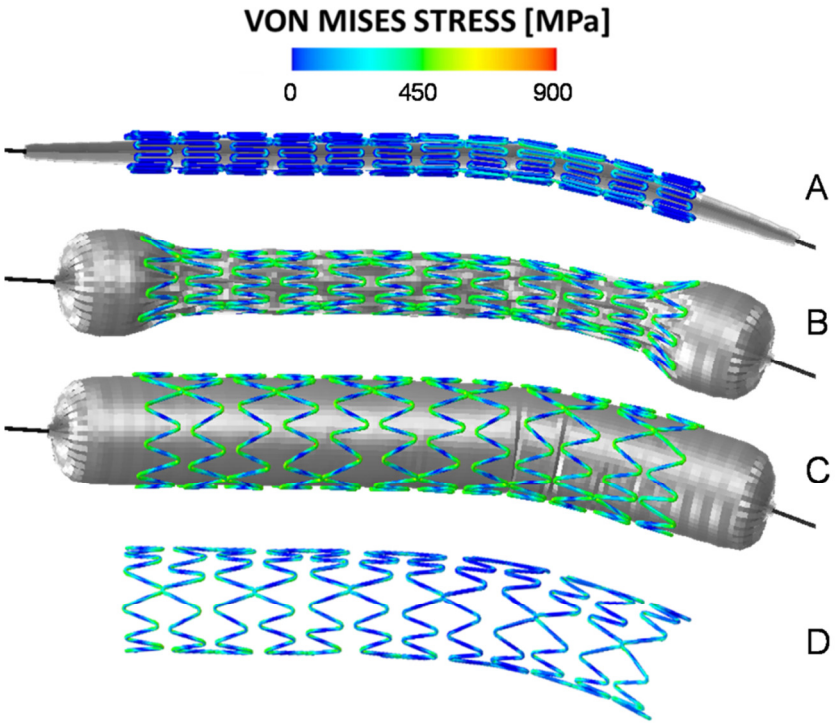

Figure 5.14 – Distal stent deployment, with Von Mises stress variations, during the various steps: initial configuration (A), mid-expansion (B), full expansion (C) and after elastic recoil (D). Balloon shortening is remarkable.

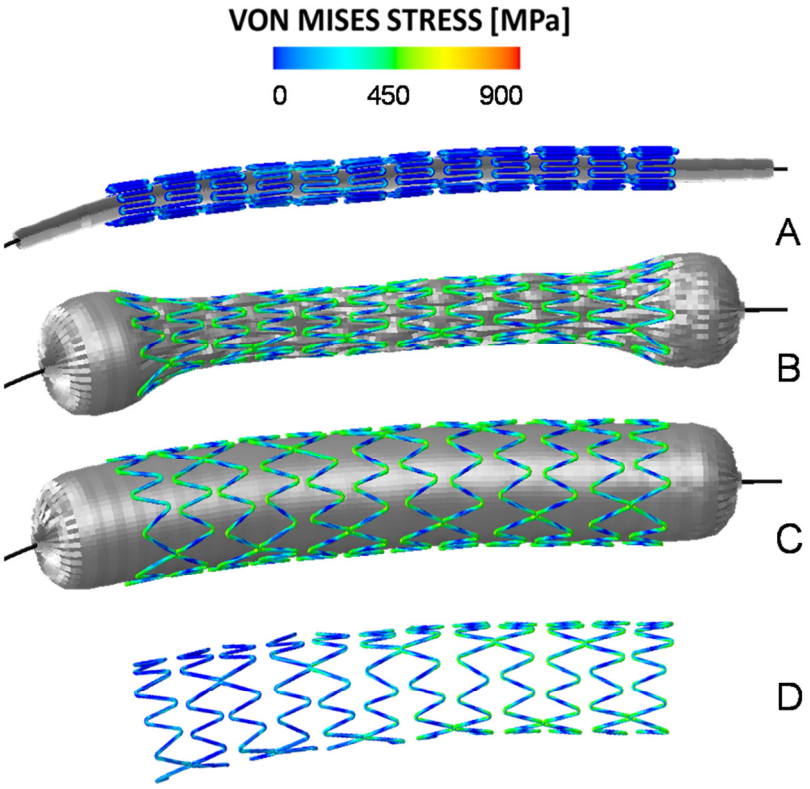

Figure 5.15 – Proximal stent deployment, with Von Mises stress variations, during the various steps: initial configuration (A), mid-expansion (B), full expansion (C) and after elastic recoil (D).

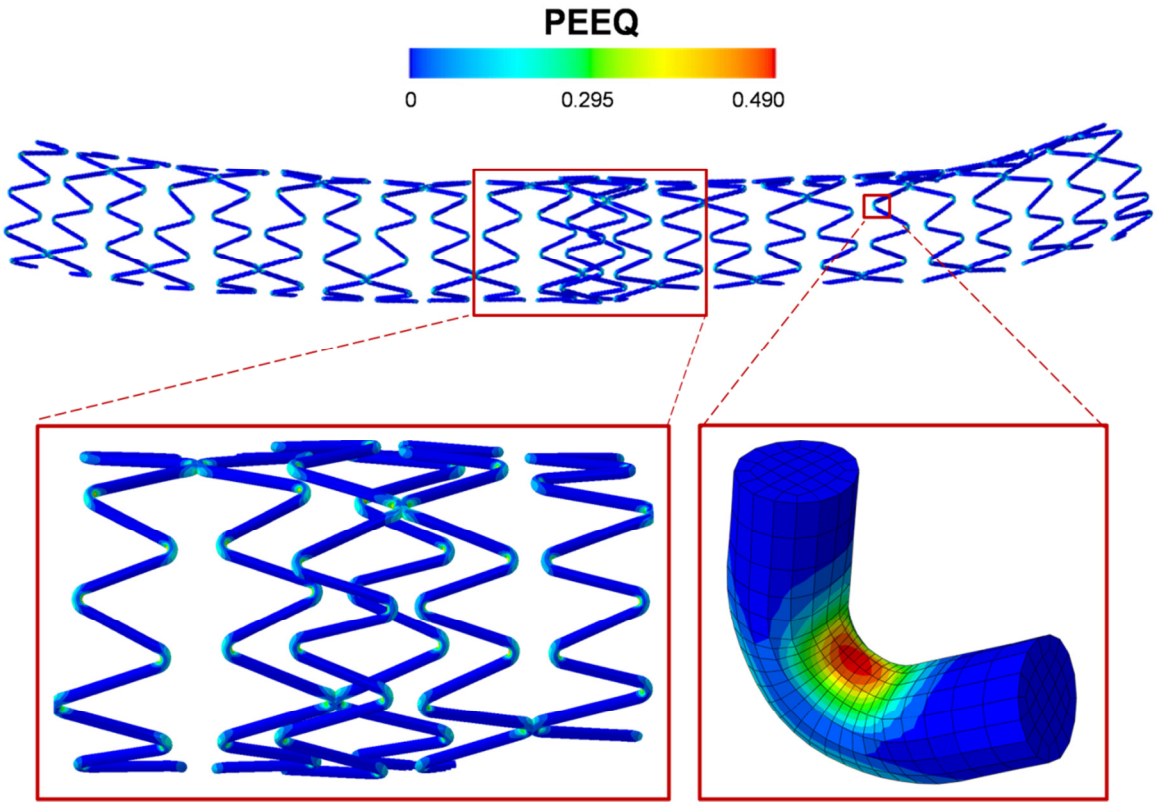

Figure 5.16 – Plastic deformation map for the two Endeavor stent models. Close-ups of the overlap region and of the local stress map of a curved part of the struts.

Table 5.2 – History of stresses and plastic deformations for the two stent models.

	σ max [MPa]		PEEQ max	
	DISTAL	PROXIMAL	DISTAL	PROXIMAL
CRIMPING	546	546	0.1179	0.1179
RECOIL	454	454	0.1179	0.1179
BENDING	539	533	0.1181	0.1187
DISTAL EXPANSION	900	533	0.4207	0.1187
PROXIMAL EXPANSION	914	907	0.4376	0.4491
FINAL RECOIL	914	884	0.4376	0.4491

The arterial response to the intervention, in terms of maximum principal stress obtained, is shown in Figure 5.17. The stress variations during the intervention can be appreciated in Fig. 5.18. The stresses caused by the angioplasty intervention soon decrease to zero, and subsequently rise to higher levels after stents implantation. The stents implantation procedure, on the other hand, causes permanent stresses acting on the arterial wall. Peak local stress values are reached close to the distal bifurcation, where the second diagonal branch starts. Also, high stresses are obtained in correspondence with the overlap between the stents. These regions appear to be the most critical during the intervention, considering the potential stronger correlation between the stress values induced on the arterial wall and the pathobiologic response. It has been proved that stents subjecting the artery to higher stress levels lead to a significantly greater neointimal thickening at stent struts, and generally provoke a more aggressive pathological response [60].

The stress map on arterial cross sectional slices appears to change remarkably in the longitudinal direction, depending on the coronary geometry and on stent positioning (see Fig. 5.19). The higher principal stresses are obtained by the arterial wall, and decrease in the elements modeled with plaque behavior. The most proximal region of the bifurcation is not heavily affected by stent implantation, as proved by the low stresses attained, caused by a larger initial diameter and no presence of plaque components. The lumen opening, allowing the normal physiological blood flow to be restored, is ideal, as proved by the steps depicted in Figure 5.20.

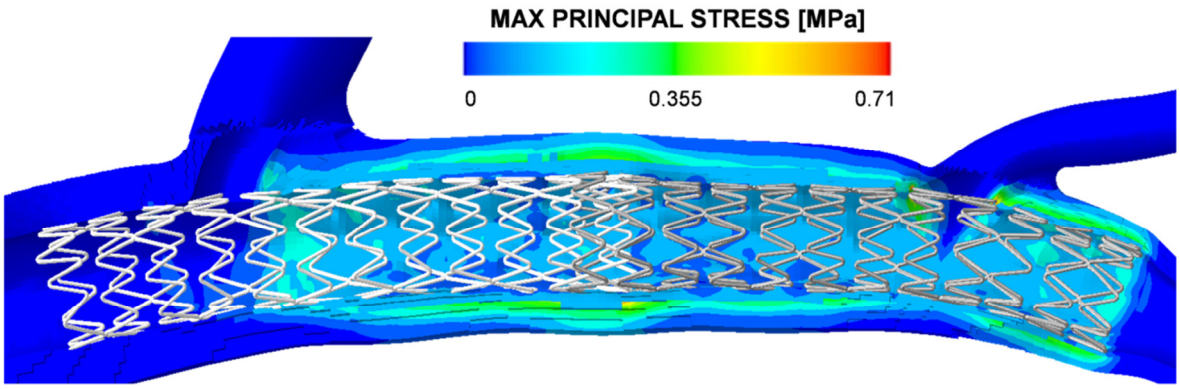

Figure 5.17 – Maximum principal stress contour map for the arterial wall at final step, with Endeavor stents implanted.

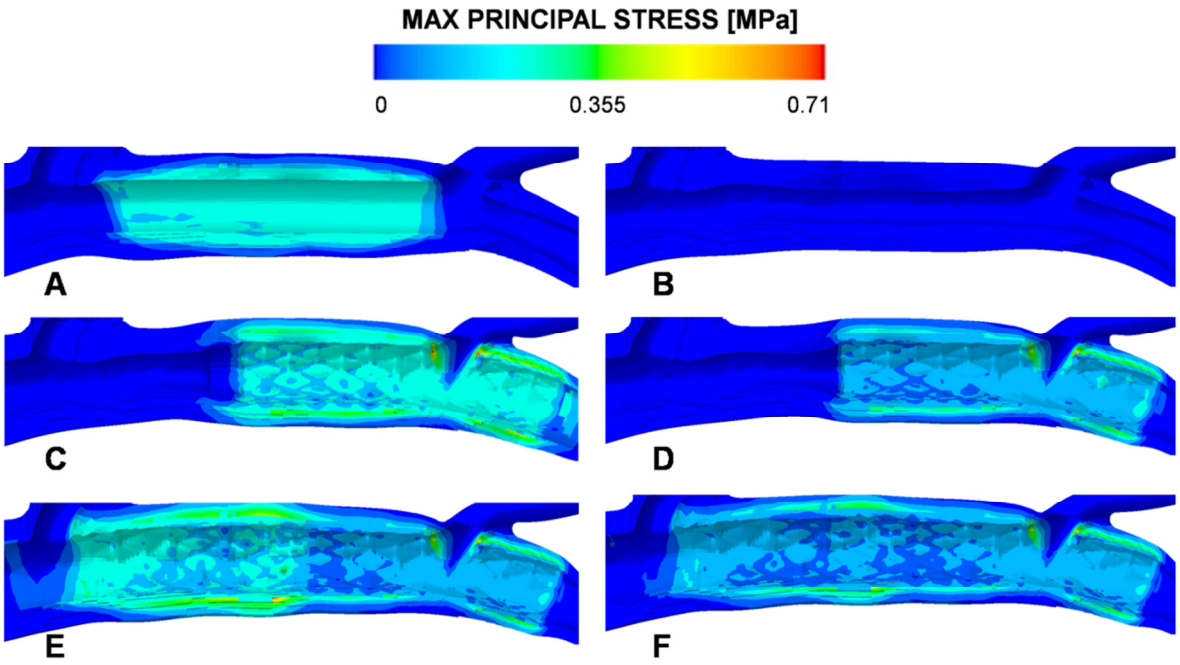

Figure 5.18 – Contour map of maximum principal stress in the arterial wall during angioplasty (A), after angioplasty (B), after distal stent expansion (C), after elastic recoil (D), after proximal stent expansion (E) and in final configuration (F).

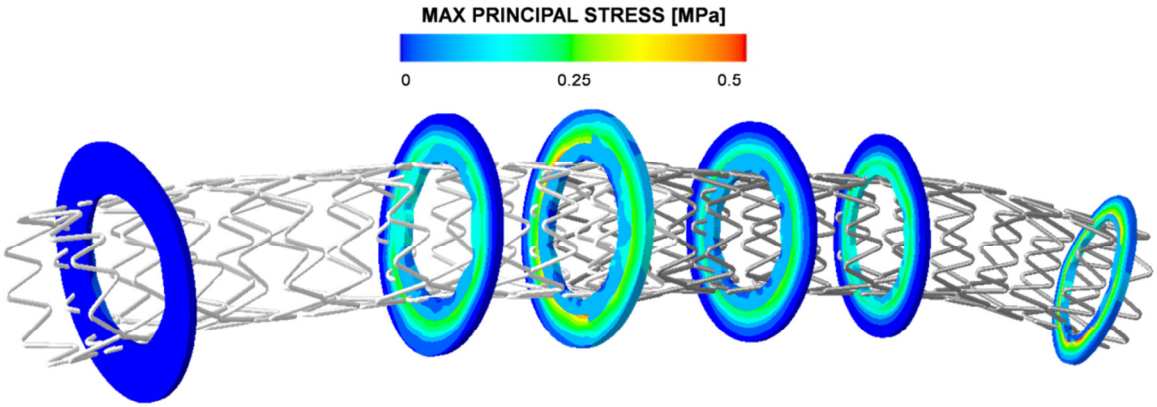

Figure 5.19 – Contour map of arterial wall stress in slices along the main branch of the bifurcation in the final configuration, after elastic recoil

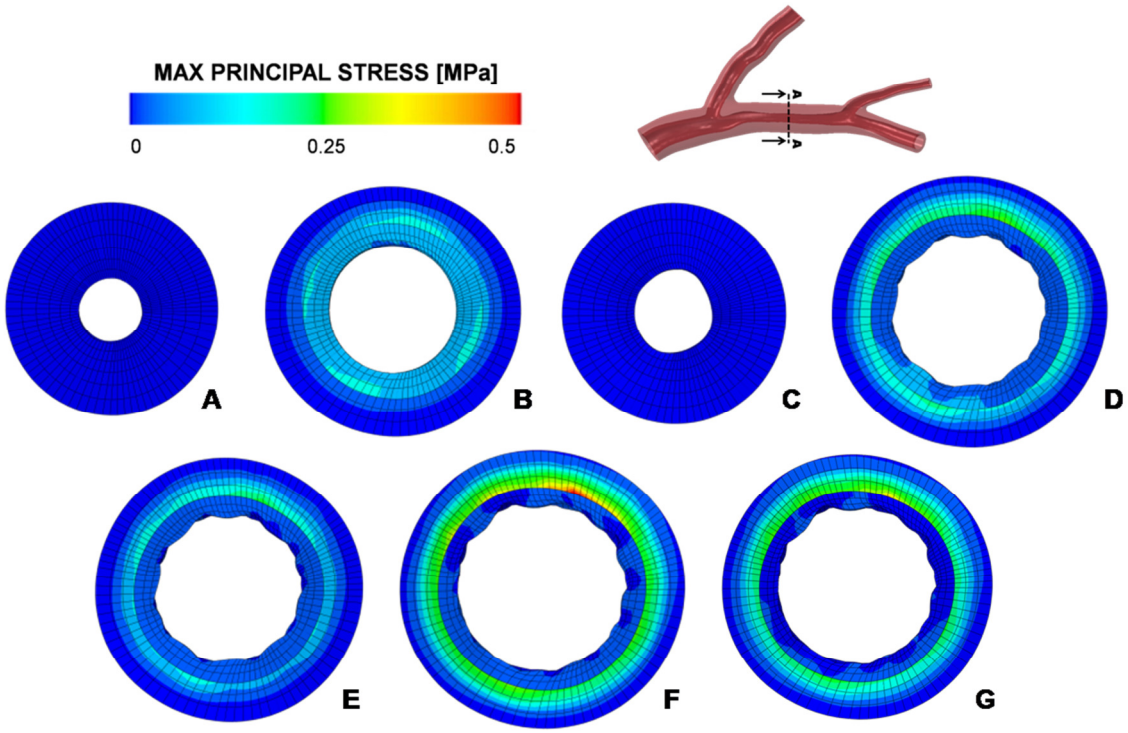

.Figure 5.20 – Cross sectional views of a highly stenotic region of the main branch. The variation of geometry and stress distribution are justified by the performed steps: initial configuration (A), angioplasty (B), post-angioplasty (C), distal stent expansion (D), subsequent elastic recoil (E), proximal stent expansion (F) and final configuration (G).

Figure 5.21 highlights the differences in the post-interventional lumen between the finite element results and the image-based reconstruction of the actual stenting procedure case that took place in Hospital Doctor Peset [23]. The overall results show an acceptable concordance, proving the feasibility of the use of finite element simulations in predicting patient-specific stenting intervention outcomes. However, some differences can be noticed as, for instance, the greater straightening of the stenotic vessel achieved in the computational analysis (see highlighted region in Fig. 5.21). This result can be explained by the presence of surrounding tissue, not considered in the numerical work. Such an assumption could be justified considering the effective anatomy of the larger coronary arteries, such as the LAD artery, that wraps around the outside of the heart and sends the smaller arteries inward. Also, calcifications could be present in the diseased vessel wall, preventing the real main branch from straightening. Unfortunately, the lack of information regarding the atherosclerotic plaque does not allow a detailed characterization of the diseased tissue, which was all modeled as a homogeneous soft cellular plaque. The

presence of hard atherosclerotic plaque could change the post-intervention lumen geometry.

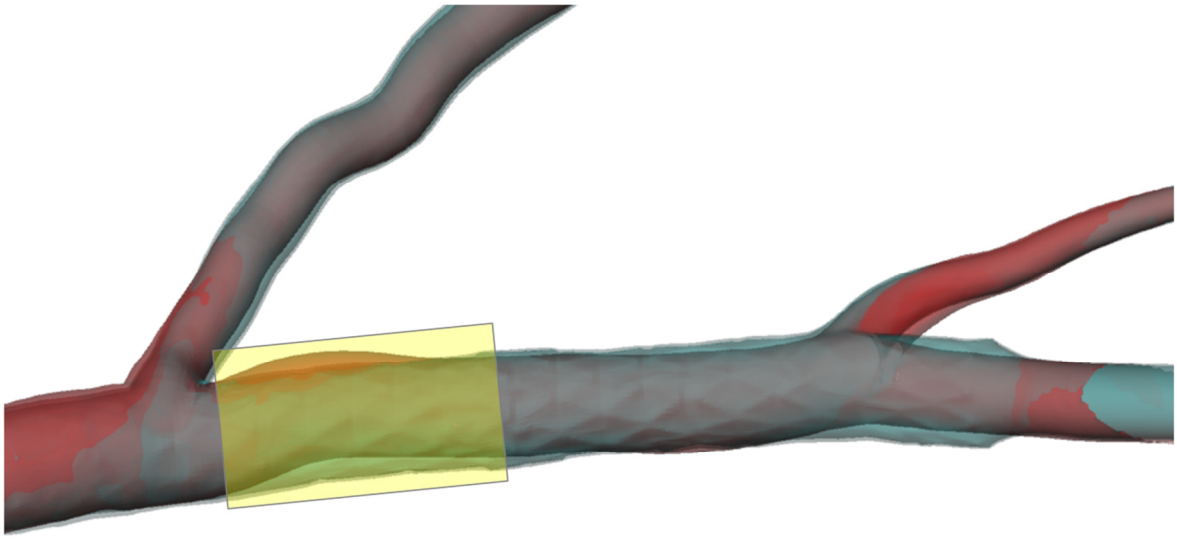

Figure 5.21 – Comparison between the post-stenting lumen geometry between the actual intervention (red) and the computational results (blue). The greater vessel straightening in the finite element simulation is highlighted in yellow.

Chapter 6

Conclusions, limitations and further development

In the sixth chapter, the main conclusions are reported, followed by the limitations of the presented model and its possible further developments.

6.1 Conclusions

The presented work aimed at replicating an actual coronary stenting intervention performed in a realistic manner. The reliability of computational analyses has been consolidated in the past decade, providing comparable results to *in vitro* studies and adding the advantages of being more flexible and cost-saving. However, most of the finite element models simulating stenting procedures lack patient-specificity, using idealized arterial geometries, thus providing only general guidelines.

Recently some computational work has been carried out using 3D reconstructions of coronary regions obtained from medical images. Nevertheless, the state-of-the-art of image-based finite element studies of stenting interventions appears to be poor, often not considering the presence of plaque or complex bifurcated arteries.

Therefore, the model implemented in this work aimed at overcoming such limitations, utilizing a patient-specific vascular geometry of an atherosclerotic left anterior descending (LAD) coronary artery that included two bifurcations with its diagonal branches. The arterial geometry was reconstructed from routine medical images, i.e. conventional angiography and computed tomography angiography. More advanced vascular imaging techniques could provide more information on the diseased arterial wall, but they usually increase invasiveness and are less common in clinical practice.

The patient-specific coronary artery was created starting from the triangulated surface of the vessel lumen, achieving the final 3D reconstruction using the vessel centerline and common values of LAD wall thickness and physiological internal diameter. Then, atherosclerotic plaques were identified based on the distance from the vessel centerline, knowing the values of healthy LAD lumen.

The CAD models of the commercial devices used in the intervention were created in order to replicate the stenting procedure that took place. The actual clinical case was simulated in every step, based on the procedural indication provided by the clinicians of Hospital Doctor Peset (Valencia).

The feasibility of the implementation of a patient-specific model replicating an actual clinical case was proved. Moreover, the finite element results were compared with the real

post-interventional ones, showing acceptable concordance. To the author's knowledge, in the coronary stenting computational field, such an investigation has never been performed.
The routine application of the presented numerical models could help clinicians in their intervention strategies, well predicting *in-vivo* outcomes. Various stenting procedure options could be simulated for patient-specific cases, comparing results in terms of lumen re-opening and mechanical behavior of the intravascular devices and of the arterial wall. By examining the biomechanical influence of specific stenting strategies, intervention planning could be greatly facilitated.
Coronary stent designers could also rely on such results to optimize strut geometries and materials, decreasing local stresses on the struts or on the arterial wall.

6.2 Limitations and further development

Some limitations are still affecting the implemented numerical models. Firstly, the triangulated surface of the pre-stenting lumen, from which the 3D reconstruction of the artery was achieved, presents some simplifications as, for instance, the circular cross section hypothesized along the whole geometry. Atherosclerotic vessel lumens are usually not perfectly circular, due to the asymmetrical presence of plaque. This assumption originates in the choice of using the two most common vascular imaging techniques, routinely used in medical practice.
As far as the mechanical properties of tissues are concerned, the artery was considered isotropic and homogeneous, even though the vessel wall is strongly anisotropic, due to the collagen fibers orientation and characterized by three different layers. Also, plaque was wholly modeled as soft cellular plaque, as a result of the lack of information about its composition. The high variability of plaque components, its degree of calcification and the presence of lipids make it an extremely difficult material to be characterized.
As far as loading conditions are concerned, the computational simulations do not consider the pre-tension to which the coronary wall is subjected (generally about 6-10 kPa). Also, arterial blood pressure (averaged 100 mmHg) inside the vessels was neglected.

In the light of these considerations, further development of the presented model can provide more accurate results and additional information from both the clinical and the design point of view. Future developments include the following:

- The use of anisotropic arterial wall modeling, taking into consideration the collagen fibers orientation.
- A more detailed and differentiated reconstruction of arterial geometry and characterization of the atherosclerotic plaque. This could be possible using more recent vascular imaging techniques, such as IVUS and OCT, capable of the identification of various plaque components. However, modeling the mechanical behavior of such tissues would still remain a critical issue.
- Computational simulations of different stenting procedures prior to the intervention in order to evaluate several options during clinical planning.
- The evaluation of drug-elution in patient-specific cases, to assess the efficacy of the drug treatment in specific vascular geometries.
- Computational fluid dynamics simulations investigating blood flow after the stenting procedure (see Fig. 6.1). Such analyses would add important information to clinicians in order to assess the modified environment in terms of bulk-flow or near-wall hemodynamic variables [61, 62].

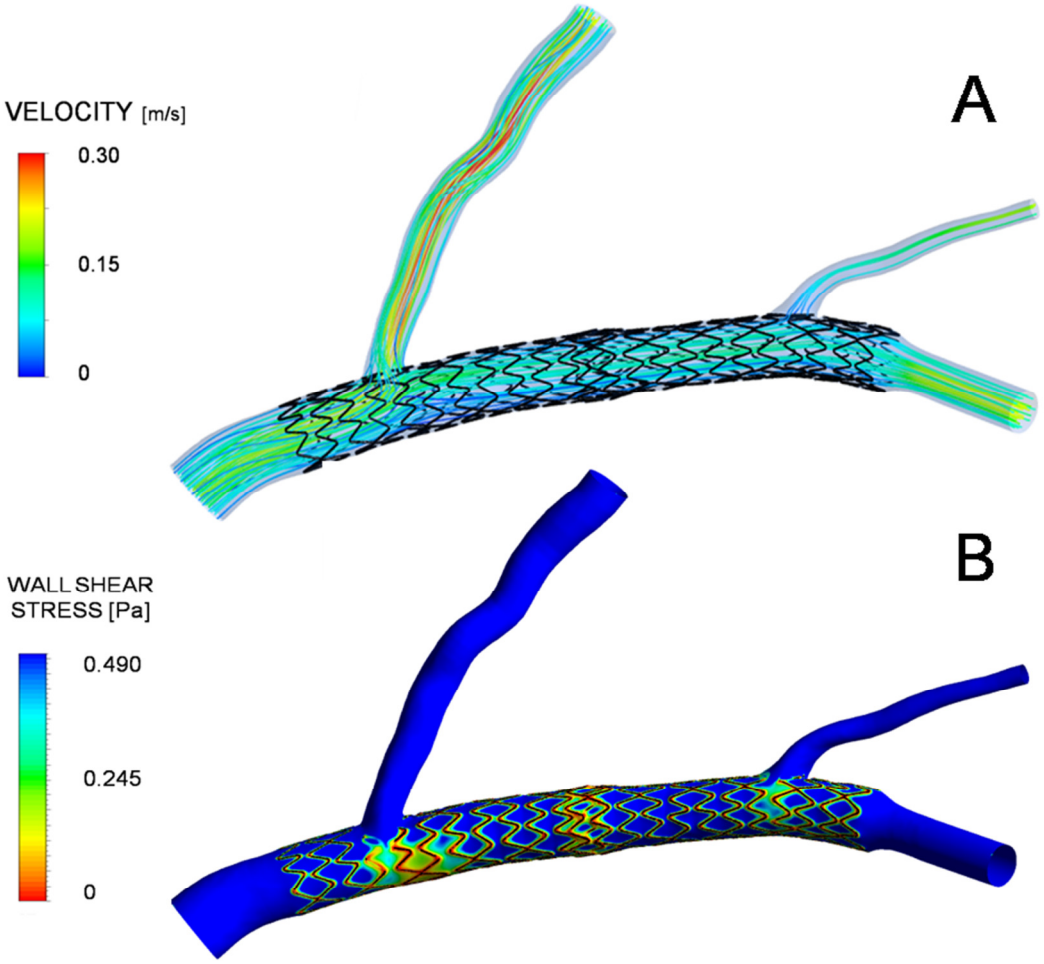

Figure 6.1 – Fluid dynamics analysis of streamline velocity (A) and wall shear stress (B) obtained simulating blood flow in the post-interventional arterial model [62].

References

[1] de Feyter PJ, Nieman K. New coronary imaging techniques: what to expect? Heart. 2002;87(3):195-197.

[2] Lederlin M, Thambo JB, Latrabe V, Corneloup O, Cochet H, Montaudon M, Laurent F. Coronary imaging techniques with emphasis on CT and MRI. Pediatr Radiol. 2011;41(12):1516-25.

[3] Schoenhagen P, White RD, Nissen SE, Tuzcu EM. Coronary imaging: angiography shows the stenosis, but IVUS, CT, and MRI show the plaque. Cleve Clin J Med. 2003;70(8):713-9. Review.

[4] Friedrich MG. Current status of cardiovascular magnetic resonance imaging in the assessment of coronary vasculature. Can J Cardiol. 2010;26 Suppl A:51A-55A. Review.

[5] Baumüller S, Leschka S, Desbiolles L, Stolzmann P, Scheffel H, Seifert B, Marincek B, Alkadhi H. Dual-source versus 64-section CT coronary angiography at lower heart rates: comparison of accuracy and radiation dose. Radiology. 2009;253(1):56-64..

[6] Zimmerman SK, Vacek JL. Imaging techniques in acute coronary syndromes: a review. ISRN Cardiol. 2011;2011:359127.

[7] www.heartscanplus.com

[8] Budoff MJ, Achenbach S, Duerinckx A. Clinical utility of computed tomography and magnetic resonance techniques for noninvasive coronary angiography. J Am Coll Cardiol. 2003;42(11):1867-78. Review

[9] Bourantas CV, Garg S, Naka KK, Thury A, Hoye A, Michalis LK. Focus on the research utility of intravascular ultrasound - comparison with other invasive modalities. Cardiovasc Ultrasound. 2011;9(1):2. Review.

[10] Pohle K, Achenbach S, Macneill B, Ropers D, Ferencik M, Moselewski F, Hoffmann U, Brady TJ, Jang IK, Daniel WG. Characterization of non-calcified coronary atherosclerotic plaque by multi-detector row CT: comparison to IVUS. Atherosclerosis. 2007;190(1):174-80.

[11] Schmitt J, Kolstad D, Petersen C. Coherence Tomography opens a window onto coronary artery disease. Optics Photonics News, 2004.

[12] Steinman DA. Image-based computational fluid dynamics modeling in realistic arterial geometries. Ann Biomed Eng. 2002;30(4):483-97. Review.

[13] Taylor CA, Steinman DA. Image-based modeling of blood flow and vessel wall dynamics: applications, methods and future directions. Ann Biomed Eng. 2010;38(3):1188-203.

[14] Wischgoll T, Choy JS, Ritman EL, Kassab GS. Validation of image-based method for extraction of coronary morphometry. Ann Biomed Eng. 2008;36(3):356-68.

[15] Galassi AR, Tomasello SD, Capodanno D, Seminara D, Canonico L, Occhipinti M, Tamburino C. A novel 3-d reconstruction system for the assessment of bifurcation lesions treated by the mini-crush technique. J Interv Cardiol. 2010;23(1):46-53.

[16] Dvir D, Marom H, Assali A, Kornowski R. Bifurcation lesions in the coronary arteries: early experience with a novel 3-dimensional imaging and quantitative analysis before and after stenting. EuroIntervention. 2007;3(1):95-9.

[17] Antiga L, Ene-Iordache B, Caverni L, Cornalba GP, Remuzzi A. Geometric reconstruction for computational mesh generation of arterial bifurcations from CT angiography. Comput Med Imaging Graph. 2002;26(4):227-35.

[18] Bijari PB, Antiga L, Wasserman BA, Steinman DA. Scan-Rescan reproducibility of carotid bifurcation geometry from routine contrast-enhanced MR angiography. J Magn Reson Imaging. 2011;33(2):482-9.

[19] van der Giessen AG, Schaap M, Gijsen FJ, Groen HC, van Walsum T, Mollet NR, Dijkstra J, van de Vosse FN, Niessen WJ, de Feyter PJ, van der Steen AF, Wentzel JJ. 3D fusion of intravascular ultrasound and coronary computed tomography for in-vivo wall shear stress analysis: a feasibility study. Int J Cardiovasc Imaging. 2010;26(7):781-96.

[20] Slager CJ, Wentzel JJ, Schuurbiers JC, Oomen JA, Kloet J, Krams R, von Birgelen C, van der Giessen WJ, Serruys PW, de Feyter PJ. True 3-dimensional reconstruction of coronary arteries in patients by fusion of angiography and IVUS (ANGUS) and its quantitative validation. Circulation. 2000;102(5):511-6.

[21] Bourantas CV, Kourtis IC, Plissiti ME, Fotiadis DI, Katsouras CS, Papafaklis MI, Michalis LK. A method for 3D reconstruction of coronary arteries using biplane angiography and intravascular ultrasound images. Comput Med Imaging Graph. 2005 ;29(8):597-606.

[22] Tu S, Holm NR, Koning G, Huang Z, Reiber JH. Fusion of 3D QCA and IVUS/OCT. Int J Cardiovasc Imaging. 2011;27(2):197-207.

[23] Cárdenes R, Díez JL, Larrabide I, Bogunović H, Frangi AF. 3D modeling of coronary artery bifurcations from CTA and conventional coronary angiography. Med Image Comput Comput Assist Interv. 2011;14(Pt 3):395-402.

[24] Mortier P, De Beule M, Carlier SG, Van Impe R, Verhegghe B, Verdonck P. Numerical study of the uniformity of balloon-expandable stent deployment. J Biomech Eng. 2008;130(2):021018.

[25] De Beule M, Mortier P, Carlier SG, Verhegghe B, Van Impe R, Verdonck P. Realistic finite element-based stent design: the impact of balloon folding. J Biomech. 2008;41(2):383-9.

[26] Connolley T, Nash D, Buffière JY, Sharif F, McHugh PE. X-ray micro-tomography of a coronary stent deployed in a model artery. Med Eng Phys. 2007;29(10):1132-41.

[27] Martin D, Boyle FJ. Computational structural modeling of coronary stent deployment: a review. Comput Methods Biomech Biomed Engin. 2011;14(4):331-48. Review.

[28] Chau AH, Chan RC, Shishkov M, MacNeill B, Iftimia N, Tearney GJ, Kamm RD, Bouma BE, Kaazempur-Mofrad MR. Mechanical analysis of atherosclerotic plaques based on optical coherence tomography. Ann Biomed Eng. 2004;32(11):1494-503.

[29] Gasser TC, Holzapfel GA. Modeling plaque fissuring and dissection during balloon angioplasty intervention. Ann Biomed Eng. 2007;35(5):711-23.

[30] Auer M, Stollberger R, Regitnig P, Ebner F, Holzapfel GA. 3-D reconstruction of tissue components for atherosclerotic human arteries using ex vivo high-resolution MRI. IEEE Trans Med Imaging. 2006;25(3):345-57.

[31] Holzapfel GA, Stadler M, Gasser TC. Changes in the mechanical environment of stenotic arteries during interaction with stents: computational assessment of parametric stent designs. J Biomech Eng. 2005;127(1):166-80.

[32] Kiousis DE, Gasser TC, Holzapfel GA. A numerical model to study the interaction of vascular stents with human atherosclerotic lesions. Ann Biomed Eng. 2007;35(11):1857-69.

[33] Gijsen FJ, Migliavacca F, Schievano S, Socci L, Petrini L, Thury A, Wentzel JJ, van der Steen AF, Serruys PW, Dubini G. Simulation of stent deployment in a realistic human coronary artery. Biomed Eng Online. 2008;7:23.

[34] Zahedmanesh H, John Kelly D, Lally C. Simulation of a balloon expandable stent in a realistic coronary artery-Determination of the optimum modelling strategy. J Biomech. 2010;43(11):2126-32.

[35] Latib A, Colombo A. Bifurcation Disease: What do we Know, What Should we do?. J. Am. Coll. Cardiol. Int.,2008; 1, pp. 218–226.

[36] Colombo A, Bramucci E, Sacca S, Violini R, Lettieri C, Zanini R, Sheiban I, Paloscia L, Grube E, Schofer J, Bolognese L, Orlandi M, Niccoli G, Latib A, Airoldi F. Randomized Study of the Crush Technique Versus Provisional Side-Branch Stenting in True Coronary Bifurcations: The CACTUS (Coronary Bifurcations: Application of the Crushing Technique Using Sirolimus-Eluting Stents) Study. Circulation 2009, 119, pp. 71–78.

[37] Molony DS, Kavanagh EG, Madhavan P, Walsh MT, McGloughlin TM. A computational study of the magnitude and direction of migration forces in patient-specific abdominal aortic aneurysm stent-grafts. Eur J Vasc Endovasc Surg. 2010;40(3):332-9.

[38] Capelli C, Taylor AM, Migliavacca F, Bonhoeffer P, Schievano S. Patient-specific reconstructed anatomies and computer simulations are fundamental for selecting medical device treatment: application to a new percutaneous pulmonary valve. Philos Transact A Math Phys Eng Sci. 2010;368(1921):3027-38.

[39] Auricchio F, Conti M, De Beule M, De Santis G, Verhegghe B. Carotid artery stenting simulation: from patient-specific images to finite element analysis. Med Eng Phys. 2011;33(3):281-9.

[40] Mortier P, Holzapfel GA, De Beule M, Van Loo D, Taeymans Y, Segers P, Verdonck P, Verhegghe B. A novel simulation strategy for stent insertion and deployment in curved coronary bifurcations: comparison of three drug-eluting stents. Ann Biomed Eng. 2010;38(1):88-99.

[41] Badalucco P, Vergari E. Stent coronarici in biforcazioni:modelli strutturali computazionali a partire da μ-TAC. 2010. Master degree final dissertation in Biomedical Engineering, Politecnico di Milano.

[42] Gervaso F, Capelli C, Petrini L, Lattanzio S, Di Virgilio L, Migliavacca F. On the effects of different strategies in modelling balloon-expandable stenting by means of finite element method. J Biomech. 2008;41(6):1206-12.

[43] http://www.medtronic.com/

[44] http://www.bostonscientific.com

[45] http://www.abbottvascular.com

[46] http://www.biotronik.com

[47] Narracott AJ, Lawford PV, Gunn JP, Hose DR. Balloon folding affects the symmetry of stent deployment: experimental and computational evidence. Conf Proc IEEE Eng Med Biol Soc. 2007;2007:3069-73.

[48] Lim D, Cho SK, Park WP, Kristensson A, Ko JY, Al-Hassani ST, Kim HS. Suggestion of potential stent design parameters to reduce restenosis risk driven by foreshortening or dogboning due to non-uniform balloon-stent expansion. Ann Biomed Eng. 2008;36(7):1118-29.

[49] Migliavacca F, Petrini L, Montanari V, Quagliana I, Auricchio F, Dubini G. A predictive study of the mechanical behaviour of coronary stents by computer modelling. Med Eng Phys. 2005;27(1):13-8.

[50] Holzapfel GA, Sommer G, Gasser CT, Regitnig P. Determination of layer-specific mechanical properties of human coronary arteries with nonatherosclerotic intimal thickening and related constitutive modeling. Am J Physiol Heart Circ Physiol. 2005;289(5):H2048-58.

[51] www.vmtk.org

[52] Gradus-Pizlo I, Bigelow B, Mahomed Y, Sawada SG, Rieger K, Feigenbaum H. Left anterior descending coronary artery wall thickness measured by high-frequency transthoracic and epicardial echocardiography includes adventitia. Am J Cardiol. 2003;91(1):27-32.

[53] Takeuchi M, Yoshitani H, Miyazaki C, Yoshikawa J. Relationship between the number of coronary risk factors and coronary atherosclerosis assessed by high-frequency transthoracic echocardiography. J Am Soc Echocardiogr. 2006;19(8):1056-62.

[54] Gradus-Pizlo I, Bigelow B, Mahomed Y, Sawada SG, Rieger K, Feigenbaum H. Left anterior descending coronary artery wall thickness measured by high-frequency transthoracic and epicardial echocardiography includes adventitia. Am J Cardiol. 2003;91(1):27-32.

[55] Loree HM, Tobias BJ, Gibson LJ, Kamm RD, Small DM, Lee RT. Mechanical properties of model atherosclerotic lesion lipid pools. Arterioscler Thromb. 1994;14(2):230-4.

[56] Turco MA. The Integrity bare-metal stent made by continuous sinusoid technology. Expert Rev Med Devices. 2011;8(3):303-6.

[57] Poncin P, Proft J. Stent Tubing: Understanding the Desired Attributes. Proceedings of the Materials & Processes for Medical Devices Conference, 2003.

[58] Dunn AC, Zaveri TD, Keselowsky BG. Macroscopic friction coefficient measurements on living endothelial cells. Tribol let. 2007; 27:233-238.

[59] ABAQUS 6.10 Documentation. Abaqus Inc., RI, USA.

[60] Timmins LH, Miller MW, Clubb FJ Jr, Moore JE Jr. Increased artery wall stress post-stenting leads to greater intimal thickening. Lab Invest. 2011;91(6):955-67.

[61] Morlacchi S, Chiastra C, Gastaldi D, Pennati G, Dubini G, Migliavacca F. Sequential structural and fluid dynamic numerical simulations of a stented bifurcated coronary artery. J Biomech Eng. 2011;133(12):121010.

[62] Mariani M, Vitale L. Studio computazionale della fluidodinamica in biforcazioni coronariche: confronto tra stent dedicati e stent tradizionali. 2012. Master degree final dissertation in Biomedical Engineering, Politecnico di Milano.